technische universität dortmund

MAX PLANCK INSTITUTE OF MOLECULAR PHYSIOLOGY

Dissertation

Structural Investigation of the Relaxed Cardiac Sarcomere by Electron Cryo-Tomography

Zur Erlangung des akademischen Grades eines Doktors
der Naturwissenschaften
(Dr. rer. nat.)
der Fakultät für Chemie und Chemische Biologie
der Technischen Universität Dortmund

Angefertigt am
Max-Planck-Institut für molekulare Physiologie in Dortmund
Abteilung für Strukturbiochemie

vorgelegt von

Davide Tamborrini

Dortmund, 31.01.2024

First Referee: **Prof. Dr. Stefan Raunser**
Department of Structural Biochemistry
Max-Planck Institute of Molecular Physiology

Faculty of Chemistry and Chemical Biology
Technical University Dortmund

Second Referee: **Prof. Dr. Leif Dehmelt**
Department of Physical Chemistry I
Faculty of Chemistry and Chemical Biology
Technical University Dortmund

Formal declaration

The work described in this dissertation was carried out from January 2020 to December 2023 under the guidance of Prof. Dr. Stefan Raunser at the Max-Planck-Institute of Molecular Physiology, Dortmund.

I hereby declare that I carried out the work independently and did not use any aid, other than the ones mentioned.

Eidesstattliche Erklärung

Die vorliegende Arbeit wurde in der Zeit von Januar 2020 bis Dezember 2023 am Max-Planck-Institut für molekulare Physiologie in Dortmund unter der Anleitung von Prof. Dr. Stefan Raunser durchgeführt.

Hiermit erkläre ich, dass ich die vorliegende Arbeit selbstständig und nur mit den angegebenen Hilfsmitteln angefertigt habe.

Table of Contents

List of Figures

List of Abbreviations

2D	2-dimensional
3D	3-dimensional
α-actinin	alpha-actinin
A-band	anisotropic band
ADP	adenosine diphosphate
ATP	adenosine triphosphate
B-state	blocked state
BH	blocked head
CAP2	adenylyl cyclase-associated protein 2
C-state	closed state
C-type SR	C-type super-repeat
cryo-EM	electron cryo-microscopy
cryo-ET	electron cryo-tomography
cryo-FIB	cryo-focused ion beam milling
CTF	contrast transfer function
D-loop	DNase-I-binding loop
D-type super-repeat	D-type super-repeat
DTT	Dithiothreitol
DHPR	dihydropyridine receptor
DRX	disordered relaxed state
EGTA	ethylene glycol tetraacetic acid
ELC	essential light chain
EM	electron microscopy/microscope
EMDB	electron microscopy data bank
ET	electron tomography
F-actin	filamentous actin
FEG	field-emission gun
Fn3	Fibronectin type III
FH	free head
FSC	Fourier shell correlation
HC	heavy chain

HCM	hypertrophic cardiomyopathy
HEPES	4-(2-hydroxyethyl)-1-piperazineethanesulfonic acid
HMM	heavy meromyosin
HPF	high-pressure freezing
HRX	hyper relaxed state
I-band	isotropic band
Ig	immunoglobin
IHM	interacting-head motif
LMM	light meromyosin
M-band	*mittel* band
MyBP-C	myosin-binding protein C
MyHC	myosin heavy chain
MYH	myosin heavy chain gene
MLC	myosin light chain
MYL	myosin light chain gene
MURF	muscle-RING-finger-protein
PDB	protein data bank
PEVK	Proline, glutamic acid, valine, and lysine residues
PFIB	plasma focused ion beam
P_i	phosphate group
RyR2	type 2 ryanodine receptor
RLC	regulatory light chain
SEM	scanning electron microscopy/microscope
SERCA	sarco/endoplasmatic reticulum Ca^{2+} - ATPase
SPA	single-particle analysis
SRX	super relaxed stated
SR	sarcoplasmic reticulum
TEM	transmission electron microscopy/microscope
TK	titin kinase
Tm	tropomyosin
TnI	troponin I
Tn	troponin
t-tubule	transverse tubule
Z-disc	*zwischen* band

CHAPTER 1 ABSTRACT AND ZUSAMMENFASSUNG

1.1 Abstract

The sarcomere is the basic unit of striated muscles and consists of interdigitating thick and thin filaments. The two types of filaments slide on each other resulting in the shortening of sarcomere itself thereby generating work. The thin filament comprises filamentous actin (F-actin), troponin (Tn), and tropomyosin (Tm). The thick filament is the force bearing part of the sarcomere and it comprises myosin, titin, and myosin-binding protein C (MyBP-C). The vast majority of the mutations responsible for familial hypertrophic cardiomyopathy and other heart and muscle diseases are borne by components of the thick filaments. However, despite its central importance, it remains unclear how thick filaments are structurally organized and how its components interact with each other and with thin filaments to enable highly regulated muscle contraction in the cardiac tissue.

In this thesis, I aimed to elucidate the molecular organization of the thick and thin filaments from left ventricular myofibrils in their relaxed state. I resorted to cryo-focused ion beam milling (cryo-FIB-milling) and cryo-electron tomography (cryo-ET) to investigate the molecular architecture of the native mammalian cardiac sarcomeres.

The reconstruction of the thick filament provides insight into the three-dimensional arrangement of myosin heads and tails, MyBP-C, and titin. This clarification of structural details sheds light on their interplay during muscle contraction. The positioning of myosin heads exhibits variability based on their location along the filament, indicating diverse capabilities in terms of susceptibility to strain and activation. Meanwhile, the arrangement and interactions of myosin tails follow a distinct pattern, potentially governed by the organization of three alpha and three beta titin chains resembling a spring. This hints at specialized functions of thick filament segments in length-dependent activation (LDA) and contraction.

Interestingly, the three titin alpha chains extend throughout the entire length of the thick filament, in contrast to titin beta. The structural analysis further reveals that the C-terminal region of MyBP-C not only binds to myosin tails but also unexpectedly interacts directly with myosin heads. This suggests a hitherto unreported direct involvement in maintaining the myosin OFF state.

Furthermore, we visualize how MyBP-C forms links between thin and thick filaments. This study provides a molecular blueprint of the cardiac sarcomere and paves the way to forthcoming research aiming to explore muscle disorders that involve sarcomeric structural components.

1.2 Zusammenfassung

Das Sarkomer ist die Grundeinheit der quergestreiften Muskulatur und besteht aus ineinandergreifenden dicken und dünnen Filamenten. Die Filamente verschieben sich ineinander, was zur Verkürzung des Sarkomers führt und dadurch Kraft erzeugt. Das dünne Filament besteht aus filamentösem Aktin (F-Actin), Troponin (Tn) und Tropomyosin (Tm). Das dicke Filament ist der krafttragende Teil des Sarkomers und besteht aus Myosin, Titin und dem Myosin-bindenden Protein C (MyBP-C). Die überwiegende Mehrheit der Mutationen, die für die familiäre hypertrophe Kardiomyopathie und andere Herz- und Muskelerkrankungen verantwortlich sind, finden sich in Komponenten des dicken Filaments. Trotz ihrer zentralen Bedeutung ist jedoch nach wie vor unklar, wie die dicken Filamente strukturell organisiert sind und wie ihre Komponenten miteinander und mit den dünnen Filamenten interagieren, um eine regulierte Muskelkontraktion im Herzgewebe zu ermöglichen.

In dieser Arbeit habe ich das Ziel verfolgt, die molekulare Organisation der dicken und dünnen Filamente von ventrikulären Myofibrillen im entspannten Zustand aufzuklären. Dazu nutzte ich einen fokussierten Ionenstrahl bei Kryo-Bedingungen, um die Proben vorzubereiten (cryo-FIB-milling) und Kryo-Elektronentomographie (cryo-ET), um die molekulare Architektur der nativen Herzsarkomere von Säugetieren zu betimmen.

Die Rekonstruktion des dicken Filaments zeigt die dreidimensionale Organisation der Myosinköpfe und -schwänze, des MyBP-C und Titins und klärt die strukturelle Grundlage für ihre Interaktion während der Muskelkontraktion auf. Die Anordnung der Myosinköpfe ist je nach ihrer Position entlang des Filaments variabel, was darauf hindeutet, dass sie unterschiedliche Fähigkeiten in Bezug auf Belastungsanfälligkeit und Aktivierung haben. Auch die Myosinschwänze weisen eine unterschiedliche Anordnung und ein unterschiedliches Muster von Interaktionen auf. Diese werden wahrscheinlich von drei alpha- und drei beta-Titinketten orchestriert, die wie eine Feder angeordnet sind. Dies deutet darauf hin, dass unterschiedliche Segmente des dicken Filaments bei der längenabhängigen Aktivierung und Kontraktion eine besondere Rolle spielen.

Überraschenderweise verlaufen die drei alpha-Titinketten über die gesamte Länge des dicken Filaments, die beta-Titinkette jedoch nicht. Die Struktur zeigt auch, dass die C-terminale Region von MyBP-C Myosin-Schwänze bindet und unerwarteterweise auch direkt mit den Myosin-Köpfen interagiert, was auf eine bisher unbeschriebene direkte Rolle bei der Aufrechterhaltung des Myosin-

OFF-Zustands hindeutet. Darüber hinaus konnte ich zeigen, wie MyBP-C Verbindungen zwischen dünnen und dicken Filamenten bildet.

Meine Arbeit liefert einen molekularen Bauplan des Herzsarkomers und ebnet den Weg für künftige Forschungsarbeiten zur Erforschung von Muskelerkrankungen, an denen strukturelle Komponenten des Sarkomers beteiligt sind.

CHAPTER 2 INTRODUCTION

In this introduction, I summarise the state-of-the-art in our understanding of sarcomere organization and give an introduction to the technique I employed to analyse it at a molecular level. First, I describe the general structural organization of the sarcomere and how its function is regulated at a physiological and molecular level (section 2.1). In section 2.2, I provide a more in-depth analysis of the different sarcomere components. For each component, I discuss the known structural features, their functional relationship and how their regulation is modulated. Finally, in the last section, I describe the main techniques I exploited during this thesis: cryo-FIB milling, cryo-ET, and subtomogram averaging (section 2.3).

2.1 General organization and physiology of the cardiac sarcomere

2.1.1 Overview of the mammalian heart

The heart is the organ responsible for pumping blood in the circulatory system. In human, mouse, and in most mammals, it is divided into four chambers: two atria and two ventricles. The atria receive the blood streams from the body periphery and from the lungs and channel them into the ventricles (Fig. A1). The ventricles have thicker walls and can generate higher pressure compared to the atria. The right ventricle pumps the oxygen-depleted blood into the pulmonary circulation while the left ventricle, the thicker and stronger of the two, generates the higher pressure required to pump the oxygenated blood into the systemic circulation.

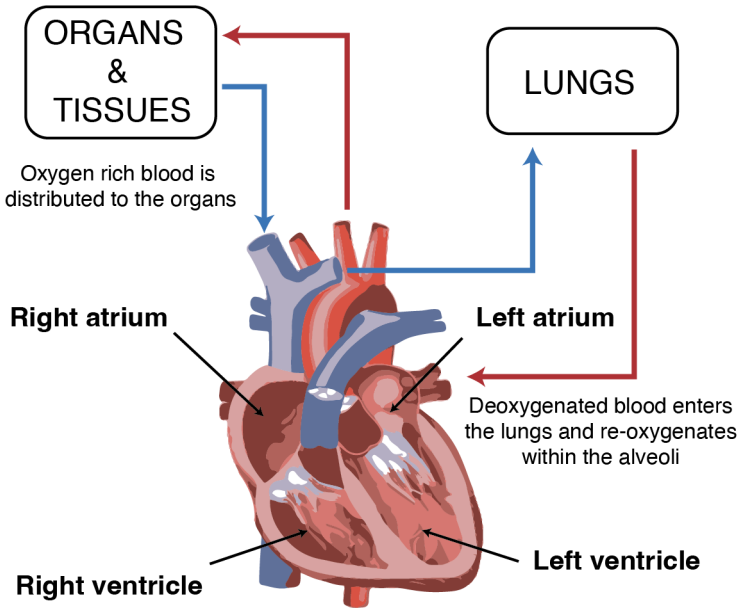

Figure A1 Diagram of the mammalian heart.

Deoxygenated blood returns to the right atrium. As the right atrium contracts, the blood flow moves into the right ventricle. Contraction of the right ventricle propels the blood through the pulmonary valve into the pulmonary artery, directing it to the lungs for oxygenation. Oxygenated blood returns to the left atrium via the pulmonary veins. Upon atrial contraction, the blood fills the left ventricle. The left ventricle contracts, forcing oxygenated blood into the aorta and is then distributed to the rest of the body, supplying oxygen and nutrients to tissues and organs.

2.1.2 The action potential controls the Ca^{2+} transient in the cardiomyocytes

Humans have a resting heart rate of 60 beats per minute (BPM) and during each heartbeat, the heart completes a cardiac cycle that consists of two phases: diastole and systole.

The heart rhythm is controlled by the sinoatrial node. Here, during systole, pacemaker cells generate the electrical impulse known as “cardiac action potential”. This is conducted via the electrical conduction system of the heart to the rest of the organ, reaching the atria, passing thought the atrioventricular node and then arriving at the ventricles. It creates a wave of membrane depolarization that travels to adjacent cardiomyocytes via the intercalated discs and reaches inside the cardiomyocytes via invaginations of the sarcolemma (cardiac cell membrane) known as transverse-tubules (t-tubules) (Fig. A2). When the action potential reaches the t-tubule it causes the activation and opening of the membrane L-type voltage-dependent Ca^{2+} channels, the dihydropyridine receptors (DHPRs). The resulting influx of Ca^{2+} activates type 2 ryanodine receptors (RyR2) located on the sarcoplasmic reticulum (SR) of the cardiomyocytes and promotes a positive feedback loop known as “calcium induced calcium release”. The SR stores high concentration of Ca^{2+} and upon activation of the RyR2 by the initial Ca^{2+} wave it releases even more Ca^{2+} in the sarcoplasm. The peak in Ca^{2+}

concentration results in the activation of the sarcomeres that leads to the conversion of the energy from the adenosine triphosphate (ATP) into mechanical contraction, ultimately leading to the ejection of blood from the heart. During diastole, the sarco/endoplasmatic reticulum Ca^{2+}-ATPase (SERCA) actively pumps Ca^{2+} back into the SR in concert with the action of the Na^{+}/Ca^{2+} exchangers, lowering the Ca^{2+} concentration again (Jeon et al. 2020). This allows the sarcomeres to relax and the heart chambers to be refilled with blood.

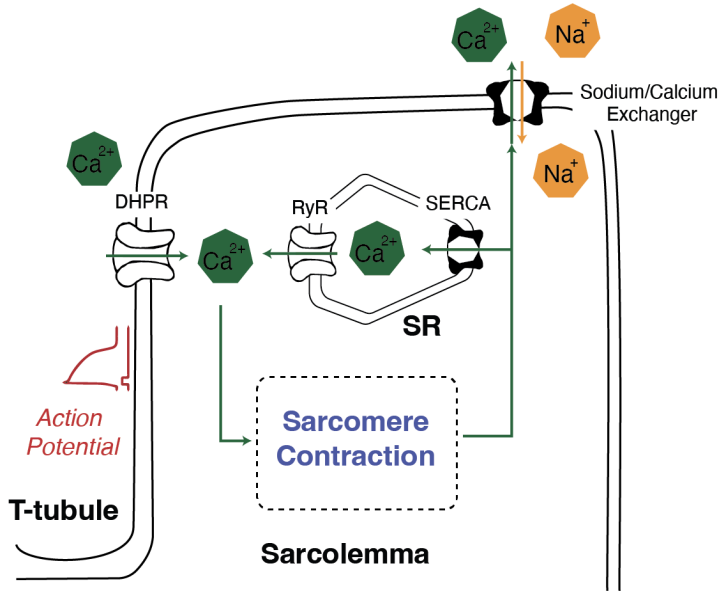

Figure A2 Schematic of the cardiac excitation-contraction coupling.

Scheme of the components involved in the excitation-contraction coupling in the cardiac myocytes and the effect on sarcomere contraction: Ca^{2+} enters the sarcolemma via the L-type voltage-operated Ca^{2+} channels (CaV; DHPR) and triggers the release of more Ca^{2+} from the sarcoplasmic reticulum (SR) via the ryanodine receptor (RyR) in a Ca^{2+}-induced Ca^{2+}-release mechanism. Ca^{2+} flux in the sarcolemma induces sarcomere contraction. Ca^{2+} removal depends on the action of SR Ca^{2+}-ATPase (SERCA) and the Na^{+}/Ca^{2+} exchanger.

2.1.3 Overview of the cardiac sarcomere

The heart predominantly contains striated muscle tissue. The cardiomyocytes in the muscle tissue are specialized polynucleated contractile cells which connect to each other via intercalated discs. Each cardiomyocyte contains multiple myofibrils that can be segmented into multiple copies of the fundamental unit of contraction: the sarcomere (Fig. A3a). The cardiac sarcomere has a resting length of ~ 2.2 µm but its length can range from 1.6 µm (contracted) to 2.6 µm (extended) and it comprises two types of filaments: thick and thin filaments. The striated pattern that can be observed in skeletal and cardiac muscle originates from the regular spacing of darker and lighter regions arising from the overlap between thick and thin filaments in the sarcomere (Fig. A3b). By convention, each sarcomeric unit extend from one Z-disc (in German "Zwischenbande", “in-between band”) to the next one. The

thin filaments are mainly formed by F-actin, troponin, and tropomyosin. They attach to the Z-discs via an alpha(α)-actinin network and extend with opposite directionality, towards the M-bands ("Mittelbande", *middle band* in German). The thick filaments are bipolar filament structures of 1.6 µm in length and are formed by approximately 300 myosin molecules, titin, MyBP-C, myomesin, and various associated proteins. The M-band represents the center of the thick filaments, where myosin molecules of opposite polarity intertwine. Here, a network of myomesin and other M-band associated proteins stabilize the filament lattice by crosslinking adjacent thick filaments. the myosin can form cross-bridges between thick and thin filaments where thick and thin filament overlap. This region is called anisotropic (A)-band. Finally, the isotropic (I)-band is the region that only contains thin filaments (Fig. A3b). The cross-sectional views of the sarcomere, show that thick and thin filaments are organized in a regular lattice with hexagonal pattern (H. E. Huxley 1957) (Fig. A3c).

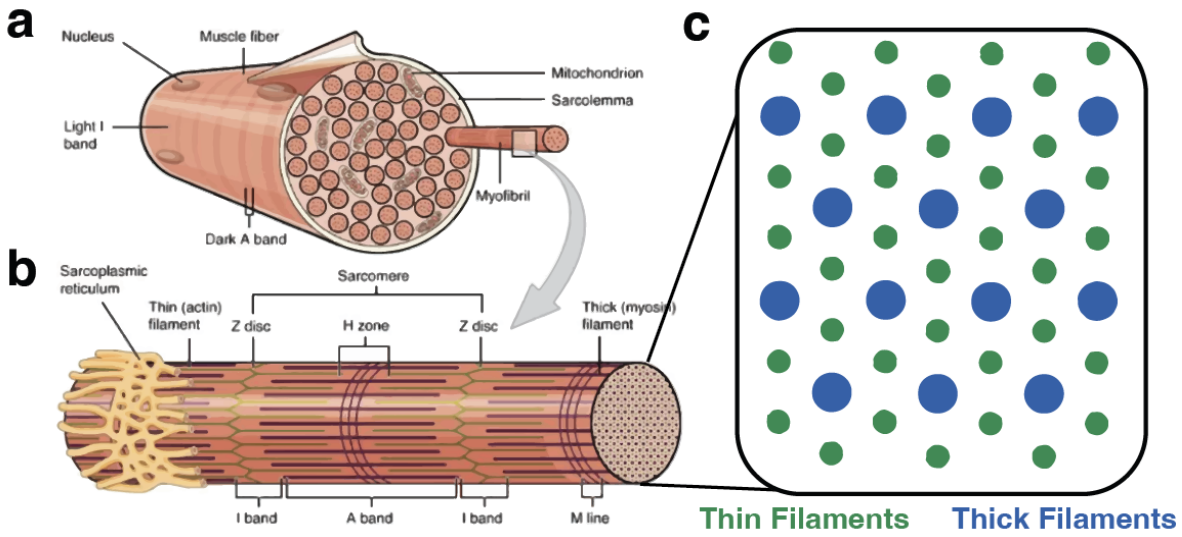

Figure A3 Organisation of a muscle fiber.

a, *Schematic depiction of a muscle cell formed by bundles of myofibrils.* ***b,*** *Zoomed view of a single myofibril showing the bands pattern of the sarcomere: the H zone is at the centre of the sarcomere and contains the M-band, the two contralateral A-bands contain the two symmetric side of the thick filaments. The I-bands contain only thin filaments, which are connected in the Z-disc.* ***c,*** *Cross-section of a sarcomere showing the hexagonal superlattice of the thin and thick filaments. Panels (a and b) are adapted from* (Betts 2013) *under license CC BY 4.0.*

2.1.3 The sliding filament model of contraction

The shortening of the sarcomere is the driving force for muscle contraction. Pioneer microscopy studies on the sarcomeres revealed that while the length of the dark region, corresponding to A-band and M-region, remained constant during contraction, the length of the light region (I-band) shortened

upon contraction (H. Huxley and Hanson 1954; A. F. Huxley and Niedergerke 1954). Knowing that the A-band was primarily formed by myosin and that the I-band primarily contained actin, these studies provided the basis for was later named "the sliding-filament model" (Fig. A4). In this model, thick and thin filaments would move relative to one other: the thin filaments sliding on the thick filaments, in a process driven by ATP, resulting in sarcomere shortening.

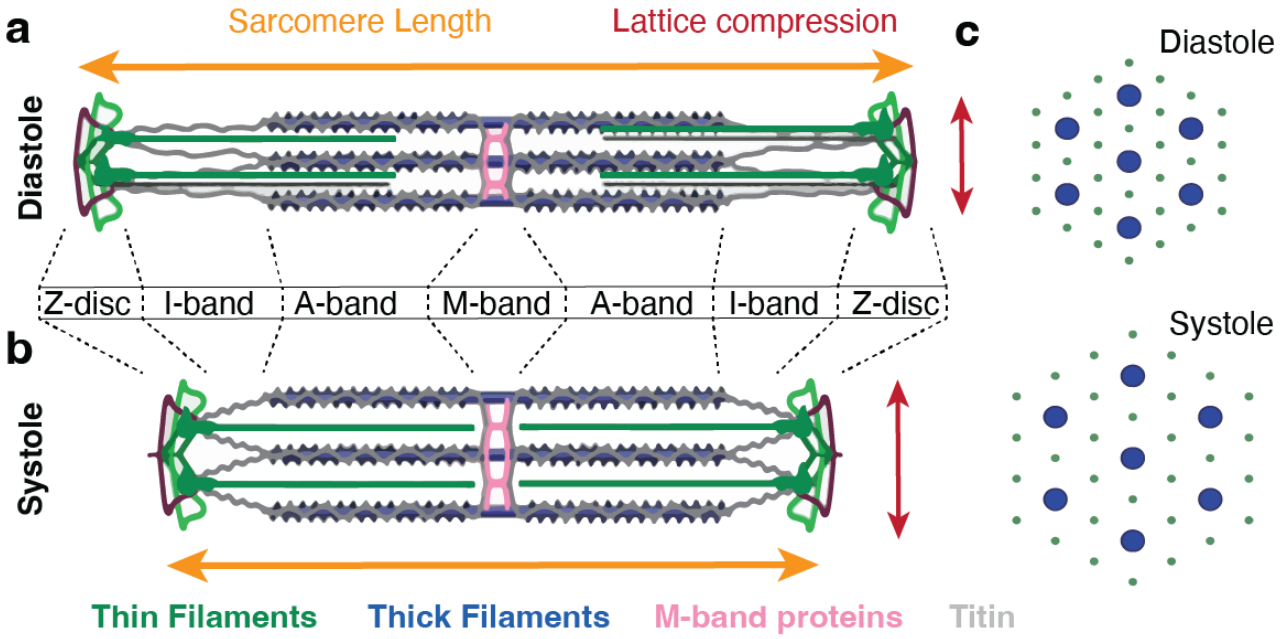

Figure A4 The sliding filament theory.

***a**, During diastole, the sarcomere is relaxed and there is only a partial overlap between thick and thin filaments. The I-bands are clearly visible and there a compression of the lattice. **b**, During systole, thick and thin filaments slide onto each other resulting in the shortening of the sarcomereric length (as well as a reduction of the I-bands length). **c**, The contraction also produces an increase in the average radial distance between filaments in the lattice. Figure adapted from* (Crocini and Gotthardt 2021) *under license CC BY 4.0.*

The regulation of the heart contraction is multifaceted and multi-layered to ensure the efficient blood stream regulation in different physiological states. As such, the mammalian heart function can be tuned by a variety of mechanisms including the electrical control over (and via) the action potentials and the neurological control via the release of neurotransmitter hormones (e.g. norepinephrine and acetylcholine). A noteworthy regulatory mechanism, specific to mammalian hearts, is the Maestrini-Starling mechanism (also known as the Frank-Starling mechanism). Initially observed and theorized by physiologist Dario Maestrini in 1914 and later verified Ernest Henry Starling, this mechanism describes an intrinsic regulatory mechanism that adjusts the force of contraction based on the degree of stretch (preload) of the heart muscle (Jacob, Dierberger, and Kissling 1992). Specifically, as the left ventricular end diastolic pressure increases, the ejected volume of the subsequent stroke also

increases. As a result, when the heart is filled with a larger volume of blood, it stretches more and responds by contracting more forcefully, resulting in a stronger contraction and ensuring an appropriate cardiac output (Fig. A5a). At the level of the single sarcomere, a similar phenomenon, known as "length-tension relationship" can also be observed (Fig. A5b) and it will be further described in section 2.2.3.

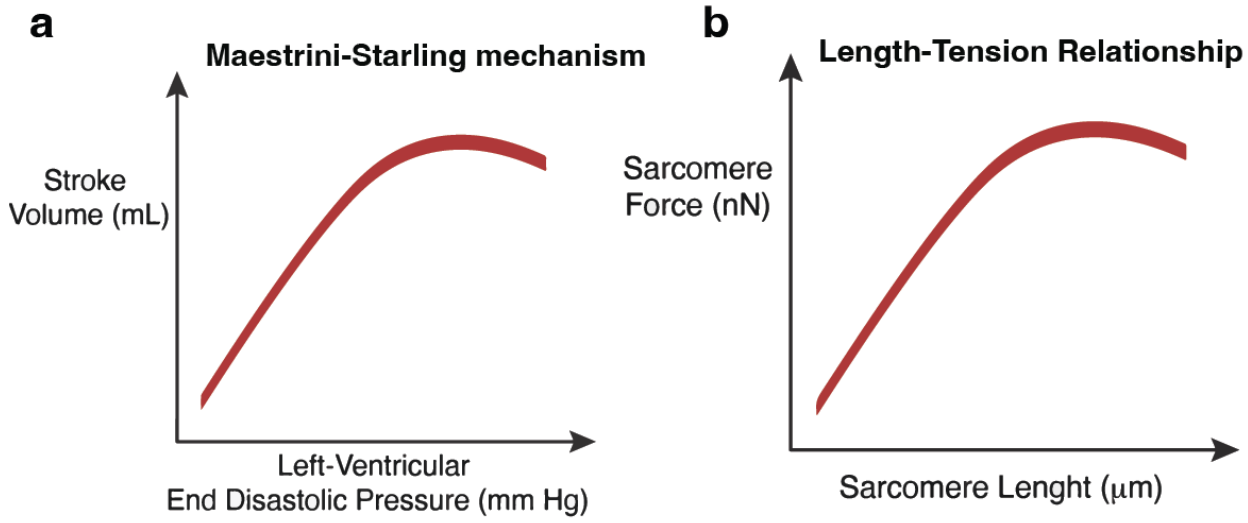

Figure A5 - Maestrini-Starling mechanism and the length-tension relationship.

***a**, The Maestrini-Starling mechanism (also known as Frank-Starling relationship) is an inherent characteristic of myocardium. It indicates that at increased ventricular volume (or myofibril length) there is an increase in the cardiac output, specifically in the end diastolic pressure, generating greater force during the contraction. This relationship is crucial in cardiac function as it allows the ventricles to accommodate greater venous return, resulting in a more forceful contraction and increased stroke volume. **b**, This physiological observation is reflected in the length-tension relationship: within physiological limits, a systole that starts at longer sarcomere lengths will generate a greater force of contraction within the sarcomere.*

2.1.4 The impact of cardiac diseases

The importance of the faithful cardiac function is exposed in the cases where the delicate and finely tuned normal regulatory mechanisms of heart contraction are impaired, causing various disease and pathological cardiac conditions. Such heart diseases include arrhythmias and heart failure. Heart and circulatory diseases cause around one in three deaths globally, with an estimated one in 13 people living with a heart or circulatory disease worldwide. One in 110 births are diagnosed with congenital heart diseases and millions more remain undiagnosed (Liu et al. 2019).

Deepening our understanding of the cardiac tissue and its fundamental components is an imperative priority to broaden our knowledge and to improve toolkits for tackling those medical challenges.

2.1.5 *Mus musculus* as a model for the study of the mammalian heat

The hearts of human and mouse (*Mus musculus*) show highly conserved anatomical features. Despite the remarkable differences in size (~ 300 grams for the human heart and ~ 0.2 grams in the mouse) and heart rate (60 BPM in humans and 600 BPM in mice, at rest) both mammals conserve the same general four-chamber architecture, the same sarcomere length and structure, and a highly conserved protein organization and composition (Krishnan et al. 2014). The two species share an almost identical set of genes and an average protein sequence identity of 85% (Krishnan et al. 2014). The general architecture of the sarcomere from striated muscle is extremely well conserved across species. This can be clearly appreciated in the plot profiles obtained via electron microscopy analysis of the sarcomeres from different organisms, such as rat, frog, and mouse (Fig. A6) (Luther et al. 2008). As such, the mouse model offers a privileged sample for the analysis of precious cardiac tissue, and it has been regularly employed over the past decades to dissect and understand cardiac muscle physiology.

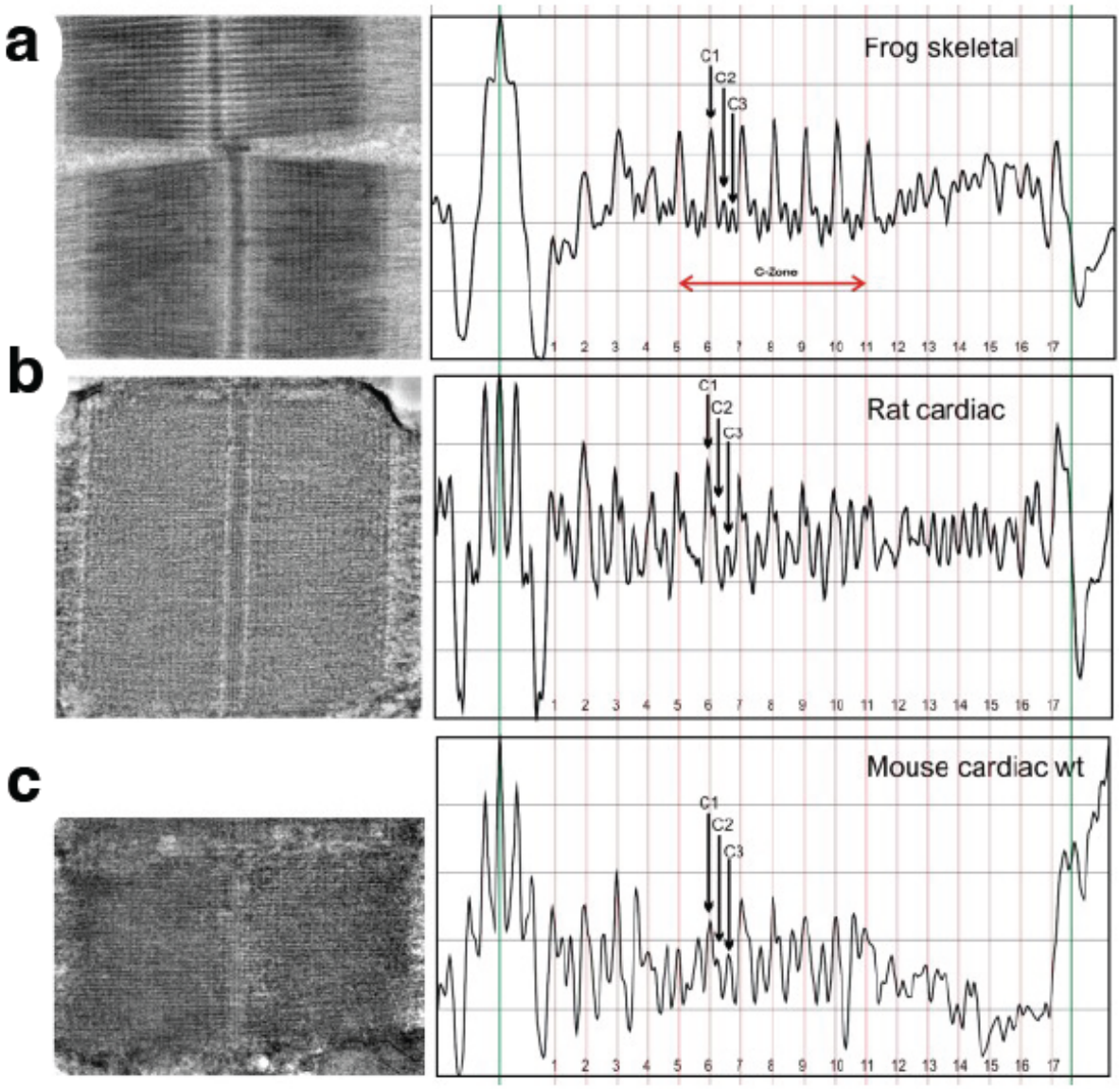

Figure A6 Sarcomere organization is highly conserved across species.

Mean profile plots of muscle structures, comparing different species. The left panels exhibit electron micrograph used to generate the average profile plots shown in the right panel. The plots are precisely aligned at the centre of the M-line and the A-band's edge. The sub-banding is evident and well conserved. The M-bands are flanked by the A-bands which are followed by the I-bands and Z-disc. ***a,*** *Micrograph and plot profile of the frog skeletal sarcomere.* ***b,*** *Micrograph and plot profile of the rat cardiac sarcomere.* ***c,*** *Micrograph and plot profile of the mouse cardiac sarcomere. Cropped figure from* (Luther et al. 2008) *under CC-BY-NC-ND 4.0 license.*

2.2 Molecular details of sarcomere

The scope of this thesis is to dissect the organization of the cardiac sarcomere in the relaxed state at molecular level. In doing so, I started from a pre-existing solid layer of scientific evidence that has been accumulated by the scientific community over the past decades. Physiological, biochemical, and structural studies have greatly helped to elucidate the protein composition and regulation in the sarcomere and represent the starting point for my investigation. In this section, I summarise the current understanding that we have on the different sarcomere components.

2.2.1 Thin filament

In the mammalian sarcomere, the thin filament is present in a 2:1 stoichiometry to the thick filament (John M. Squire et al. 2005). It is formed by a backbone of F-actin, associated with tropomyosin and troponin. It originates in the Z-disc and, in cardiac muscle, its length is regulated by the interplay of various proteins such as CapZ, nebulin, nebulette, tropomodulin, leiomodulin, cofilin and adenylyl cyclase-associated protein 2 (CAP2).

F-Actin

Actin is a fundamental protein that form filaments and is found in virtually all eukaryotes. It plays a pivotal role in various cellular processes, particularly in the context of muscle function and cell motility (Pollard and Cooper 2009). In its monomeric form, actin is 45 kDa flattened globular protein (G-actin) (Fig. A7a) and in vertebrates it exists in six different isoforms, sharing 90% sequence identity, and having unique and overlapping functions and localizations. Three α-actin isoforms are expressed in muscles (cardiac, skeletal and smooth), β-actin is found in non-muscles cells, and two γ-actin isoforms are expressed in smooth muscle and in non-muscle cells (Perrin and Ervasti 2010).

At physiological salt concentration, G-actin can spontaneously polymerize into F-actin in a reversible and dynamic manner, forming long, stable filaments that shape the cytoskeleton inside the cells (Fig. A7b). Each actin monomer has a pocket for binding an adenosine nucleotide, either adenosine triphosphate (ATP) or adenosine diphosphate (ADP). The filament elongation is primarily driven by ATP-bound G-actin monomers. F-actin is a polar filament with an arrangement that can be described either as parallel double-stranded right-handed helix or as a single-stranded left-handed helix with a

helical twist of -166.7° and helical rise of 27.5 Å (Fig. A7b). The two ends of the F-actin have distinct rate constants for the association and dissociation of G-actin. The so-called *barbed end* of F-actin has a faster growth rate compared to the (opposite side) *pointed end*. Once the ATP-actin monomers are incorporated in the filament, they undergo a conformational change that activates the ATPase activity of the protein. This nucleotide hydrolysis takes place in a relatively fast timescale (seconds) while the release of the inorganic phosphate is comparatively slower (minutes) (Fig. A7c) (Merino et al. 2018; Oosterheert et al. 2022). The ADP-actin monomers then dissociate from the filament and once released in the cytoplasm they will spontaneously re-exchange ADP for ATP and are ready to be incorporated again in actin fibrils. In physiological condition, this generates a *treadmill* behaviour of F-actin: the barbed end is elongated by association of ATP-actin monomers while the pointed end faces a similar rate of dissociation of ADP-actin monomer, resulting in a constant filament length (Lappalainen et al. 2022).

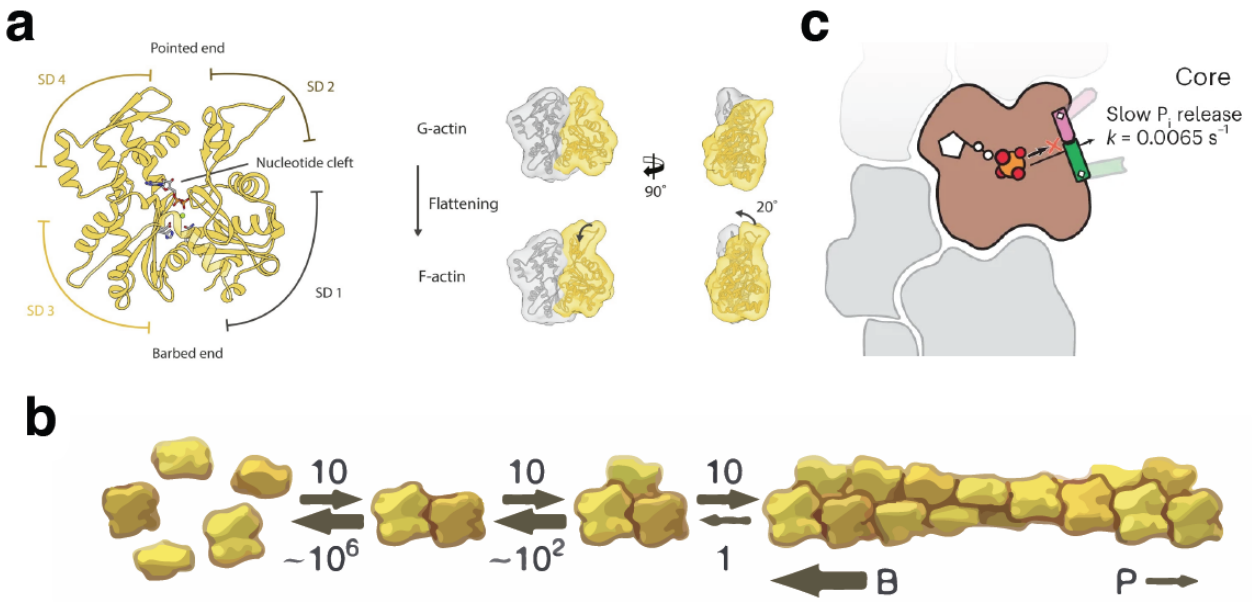

Figure A7 Molecular details of actin and its polymerization.

a, *Diagram depicting the structure of the G-actin, comprising four subdomains (SD) and a central nucleotide binding cleft.* ***b,*** *G-actin spontaneously polymerize into F-actin in a reversible and dynamic manner, resulting in the formation of long, stable filaments that contribute to the structural framework of the cytoskeleton within cells. The process involves spontaneous nucleation and elongation, with unstable dimers and trimers. Longer polymers exhibit rapid growth at the barbed end (B) and slower growth at the pointed end (P).* ***c,*** *Nucleotide hydrolysis takes place in the central nucleotide cleft and the release of the inorganic phosphate is relatively slower (minutes) compared to the hydrolysis.*

Panel ***a*** *is adapted from* (Merino, Pospich, and Raunser 2020) *under license CC-BY-NC-ND. Panel* ***b*** *is adapted from* (Pollard and Cooper 2009) *under license CC-BY-NC. Panel* ***c*** *is adapted from* (Oosterheert et al. 2023) *under license CC-BY 4.0.*

The actin network dynamics are regulated by several proteins and processes that finely tune the various aspects of the formation, branching, maintenance, function, and termination of actin filaments. In the sarcomere the F-actin is the backbone for the thin filaments and its most important function is to provide anchor points to the myosin in the thick filament and allow the contraction. F-actin is anchored with the barbed ends to the Z-disc and the pointed ends extend in the direction of the M-band. Here, both F-actin ends are protected: in the Z-disc by CapZ and towards the M-band by tropomodulin. As such, the addition of new ATP-actin monomers is limited on both side by the two capping proteins. However, tropomodulin is more dynamically associated compared to CapZ and this leads to a faster subunit exchange at the pointed end (Cooper and Sept 2008). Notably, in cardiac sarcomeres, the thin filament length is controlled by two M-band associated-proteins: Cofilin-2, which disassembles both ADP- and ATP/ADP-Pi-actin filaments (Kremneva et al. 2014), and CAP2, which depolymerizes and inhibits actin incorporation (Colpan, Iwanski, and Gregorio 2021).

Tropomyosin and the troponin complex

Tropomyosin and troponin are indispensable regulatory components for the thin filament organization in the sarcomere. They orchestrate the translation of varying Ca^{2+} concentrations in the sarcomere into structural activation/inactivation of the thin filament. In the thin filament, actin, tropomyosin (Tm), and troponin (Tn) are present at a 7:1:1 stoichiometric distribution. Tn is composed of three subunits: troponin C (TnC), the Ca^{2+}-binding regulatory subunit; troponin T (TnT), which binds to Tm; and troponin I (TnI), the inhibitory subunit (Figure A8a).

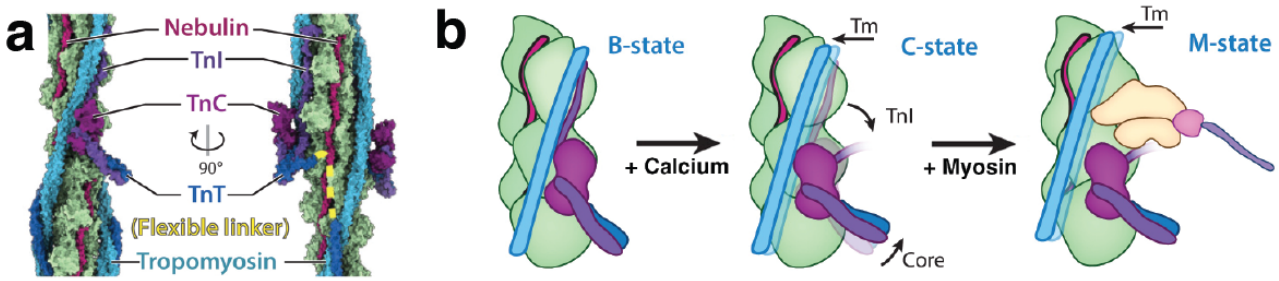

Figure A8 Molecular composition of the thin filament containing. F-actin, Tm, and Tn.

a, *Overview of the thin filament from the skeletal muscle containing F-actin, Tm, Tn, and nebulin.* ***b,*** *Schematic showing the azimuthal shift of Tm orchestrated by Tn in presence of Ca+ and upon binding myosin binding. Figure reproduced from* (Wang and Raunser 2023) *with permission from the authors.*

Tropomyosin is a coiled-coil protein winding along each of the two strands of the actin filament and forming head-to-tail polymers that repeat every 37 nm and stabilize the F-actin (von der Ecken et al. 2015). In the sarcomere, starting at 40-60 nm from the Z-disc, tropomyosin decorates the actin filaments and covers them all the way to their end, in the proximity of the M-band (Luther 2009).

During systole, the intracellular Ca^{2+} concentration rises to ~1 µM while in diastole it drops to ~100 nM (Kiess and Kockskämper 2019). During each heartbeat, the position of tropomyosin on F-actin can shift azimuthally, in a Ca^{2+}-concentration manner. During systole, tropomyosin moves towards the so-called C(closed)-state, which allows partial binding of myosin to actin. Upon binding of myosin, tropomyosin further moves to a fully open state, named the M(myosin)-state (Vibert, Craig, and Lehman 1997). On the other end, during diastole, at low Ca^{2+} concentration, tropomyosin shifts in a position that sterically blocks the myosin binding site on actin, resulting in its B(blocking)-state (Fig. A8b) (Yamada, Namba, and Fujii 2020).

The azimuthal shift of tropomyosin from the C-state to the B-state is driven by a conformational change of the troponin complex. The troponin complex has a 1:1 stoichiometry to tropomyosin and, similar to tropomyosin, binds the thin filament every 37 nm (Ohtsuki 1974). The complex appears as an L-shaped core associated with long arm extensions (Fig. A8a). The long arm is formed by coiled-coil structures of both TnI and TnT, while the short arm is composed of TnC, which forms two lobes that rotate upon Ca^{2+} binding. This conformational change is associated with a shift in the position of the TnI, which moves from a position close to tropomyosin to a position closer to TnC, resulting in an accessible myosin binding site at high Ca^{2+} concentration, upon binding of myosin the Tm is further shifted in the M-state (Yamada, Namba, and Fujii 2020; Wang and Raunser 2023) (Fig. A8b).

In synergy with to these mechanisms, it has been proposed that the N-terminal domains of MyBP-C can also regulate the azimuthal shift of tropomyosin and tune the accessibility of the myosin binding site on actin. This aspect of thin filament regulation will be discussed later in this thesis (see section 2.2.5).

Thin filament length – Nebulin/nebulette, tropomodulin and other regulatory proteins

The length of the thin filament in the sarcomere is a critical aspect of muscle function and regulation. Several mechanisms and components are involved in its regulation, and while the exact details are still a subject of ongoing research, we have insights that can help shed light on this process.

In well aligned skeletal sarcomeres, the thin filaments terminate at the same transverse section showing a uniform length within the fibre. However, this length is variable depending on the muscle type and on the species, ranging from 0.9 to 1.4 μm, seeming to correlate with the fiber type (slow twitch vs fast twitch). For instance, in rabbit psoas skeletal muscle, the length of the thin filament is 1.1 μm, while fast-twitch and slow-twitch fibers in perch muscle show lengths of 0.94 μm and 1.24 μm, respectively (H. L. Granzier, Akster, and Ter Keurs 1991). The thin filament in human deltoid has a length of 1.19 μm while it is 1.37 μm in the pectoralis major, possibly correlating with the levels of type 2X myosin protein levels (Gokhin et al. 2012).

Cardiac muscle does not follow the pattern of consistent thin filament lengths, displaying a broader range of thin filament lengths. In the cardiac sample, the uniform front of thin filament length is absent and their length ranges from 0.6 μm to more than 1.1 μm within the same sarcomere. However, the absolute dimensions of the longest thin filament is yet to be ascertained and cardiac thin filament can often cross over into the contra-lateral A-band (Page 1974; Thomas F. Robinson and Winegrad 1977; T F Robinson and Winegrad 1979).

Nebulin is a key protein found in vertebrate skeletal muscle and presents almost 200 individual repeats of 35 α-helical amino acid, grouped into 22 seven-module super-repeats. While nebulin's function as a molecular ruler has been postulated, its role in specifying thin filament length remains a topic of research (Yuen and Ottenheijm 2020; Wang et al. 2022). Nebulin can bind tropomodulin, possibly influencing the localization of tropomodulin to the pointed ends of thin filaments of the appropriate length (R. Littlefield and Fowler 1998).

In vertebrate cardiac muscle, a smaller nebulin isoform, nebulette, extends only about 0.2 μm into the I-band, being significantly shorter than nebulin and only covering a fraction of the total thin filament's length (Moncman and Wang 1995). Concomitantly, nebulin has not been found in arthropods, yet thin filament lengths increase uniformly during Drosophila flight muscle development (Reedy and Beall 1993). The asymmetric sarcomeres of the crab *Portunus depurator* present an extremely interesting case study, too. In this organism, the M-line is displaced off-center in the A-band and the resulting two half-sarcomeres have asymmetric thick filament portions. Remarkably, the thin filament lengths in the contralateral A-bands are similarly asymmetric and both sides of the pointed ends are located at the same distance, at the edge of the bare zone, from the M-line (Franzini-Armstrong 1970).

Tropomodulin, a protein crucial for actin filament capping, plays a unique role in inhibiting actin elongation primarily from the pointed ends of tropomyosin-actin copolymers. Its binding directly to both tropomyosin and actin ensures tight capping activity (Gokhin et al. 2015; Kolb et al. 2016). This interaction suggests a mechanism for restricting possible thin filament lengths in an incremental fashion, allowing filament lengths to vary only in steps equal to the length of one tropomyosin rod.

In conclusion, the regulation of thin filament length is a complex process involving various components, including nebulin, tropomodulin, tropomyosin, and possibly, thick filament components such as titin and M-band associated components.

In cardiac sarcomere, as a result of the thin filament length variability, the striations of cardiac M-bands appear less distinct. This longer and less regular lengths have been proposed to act as a mechanical feature that prevents the cardiac sarcomere from over contracting. While skeletal muscles are anchored to rigid tendons and bones that can prevent over contraction, cardiac muscles lack stiff attachment points. Instead, cardiac over contraction might be prevented by the longer thin filaments sliding thought the M-band and into the opposite A-band, generating an osmotic pressure that would deter excessive contraction (R. S. Littlefield and Fowler 2008).

2.2.2 General introduction to the thick filament structure and regulation

As previously mentioned, the thick filament is 1.6 μm long and it comprises approximately 300 myosin molecules, titin, MyBP-C, myomesin, and additional associated proteins. It is a bipolar structure with one symmetry centre positioned in the M-band, at the M-line. Additionally, the thick filament also shows a 3-fold rotational symmetry (C3 symmetry) resulting in a dihedral 32-point group symmetry. At the M-line, the myosin from the opposite direction intertwines creating a 160 nm zone that only contains myosin tails (bare zone). The fist layer of projecting myosin heads (so called "crown of heads") appears symmetrically at 80 nm distance from the M-line (Al-Khayat et al. 2010; Luther, Munro, and Squire 1981). Starting from the first crown, the heads are organized on the filament surface in a quasi-helical array that comprises three layers of crowns and shows a rise of 430 Å. The myosin bundle extends into the A-band where it shows a systematic helical perturbation and is separated by approximately 143.3 Å (430/3) and a twist of 40° on average (Sjöström and Squire 1977; H. E. Huxley and Brown 1967). After tapering into the I-band, the thick filaments anchor to the Z-disk via the N-terminus of the titin (Fig. A4) (Luther 2009).

2.2.3 Myosin

Myosin structure

Myosins are a superfamily of actin-dependent molecular motors (ATPases) ubiquitous across eukaryotic cells. They comprising over 40 known classes, 13 of which are expressed in mammals driving various motile processes (Foth, Goedecke, and Soldati 2006). They are crucial for muscle contraction, vision, hearing, cell motility, and host cell invasion of apicomplexan parasites (Foth, Goedecke, and Soldati 2006).

The myosin repertoire in mammals is variable and represented with up to 40 different genes. Myosin heavy chains are involved in diverse cellular functions such as organellar transport, mitosis, and cell locomotion. Myosin II, isolated from skeletal muscle thick filaments by Wilhelm Kühne in 1864 (reviewed in (Kritikou 2010) was the first myosin discovered. Each myosin molecule is a hexamer that comprises two heavy chains (MyHCs), two essential light chains (MLCs), and two regulatory MLCs (Fig. A9a). In mammals, 11 MyHCs are coded by myosin heavy chain (MYH) genes, 6 of which are abundantly found in muscle and 5 additional genes with limited expression in specialized muscles. The five essential MLCs are coded by four myosin light chain (MYL) genes, and two regulatory MLCs by two other MYL genes (Schiaffino et al. 2015). With the exception of Class VI myosin, which moves towards the (−)-end of actin filaments, almost all studied myosin classes move towards the (+)-end (Wells et al. 1999). Some myosin classes show the ability to move cargoes as single (two-headed) molecules. Myosin V, for instance, serves as a processive vesicle trafficking motor, and moves on actin similarly to how kinesins move vesicles on a microtubule (Mehta et al. 1999). Class II, or *conventional myosin*, are found in mammalian striated muscle, and will be referred to as “myosin” throughout this thesis.

While various myosin motor proteins are present in different cell types, the thick filaments of mammalian heart muscle primarily consist of only two isoforms: (α)-myosin heavy chain (encoded by MYH6) and (β)-myosin heavy chain (encoded by MYH7) (C. A. Henderson et al. 2017). The distribution of isoforms among myosin heavy chains in the mammalian ventricular myocardium is associated with the contractile speed of cardiac muscle. In the ventricular myocardium of small mammals, the composition of MyHC consists of 90% α-MyHC, whereas in humans the predominant isoform is β-MyHC (95%). In humans, MYH7 is predominantly expressed in ventricular chambers, while MYH6 is the primary isoform found in atrial chambers (Nakao et al. 1997).

Myosin light chains (MLCs) belong to the calcium binding protein superfamily and are regulated by phosphorylation via two opposing pathways: phosphorylation by myosin light-chain kinases and dephosphorylation driven by myosin light-chain phosphatases (C. A. Henderson et al. 2017). MLCs are divided in two categories: essential light chains (ELCs) and regulatory light chains (RLCs). In skeletal and cardiac muscles, phosphorylation of the RLCs has been demonstrated to enhance force generation while in smooth muscle switches on myosin and is the primary control for contraction (Trybus 1994).

Myosin heavy chains have three distinct domains: N-terminal head, neck, and C-terminal tail. The motor domain in the head binds filamentous actin and drives actin-based movement through ATP hydrolysis. The neck region transduces force while the tail region mediates myosin interactions and assembling in the thick filament. The light chains regulate MHC motor function by binding to the neck region.

The head of myosin can be structurally divided in four subdomains: the upper 50 KDa, the lower 50 KDa, the N-terminus, and the converter. The myosin motor domain consists of the upper and lower 50 KDa domains together with the N-terminus, while the converter contains an elongated helix that associates with the ELC and RLC to constitutes the myosin "lever arm", which enhances movements within the myosin motor domain (Llinas et al. 2015; Sweeney, Houdusse, and Robert-Paganin 2020) (Fig. A9b,c). The motor domain contains the actin-binding site and the ATPase domain.
Historically, myosin has also been described according to its proteolytic digestion products. In the presence of magnesium, myosin can be cleaved by α-chymotrypsin into heavy meromyosin (HMM, containing a segment of the tail and the head domains) and light meromyosin (LMM, containing the remaining fragment of the tail). Further digestion of HMM by papain produces the myosin S1 and myosin S2 sub-fragments. S1 includes the head domains (the first ~850 residues of the MHCs together with the two MLCs) while the S2 represents ~50 nm of the MHC tails, starting from the myosin neck (Kominz et al. 1965) (Fig. A9a).

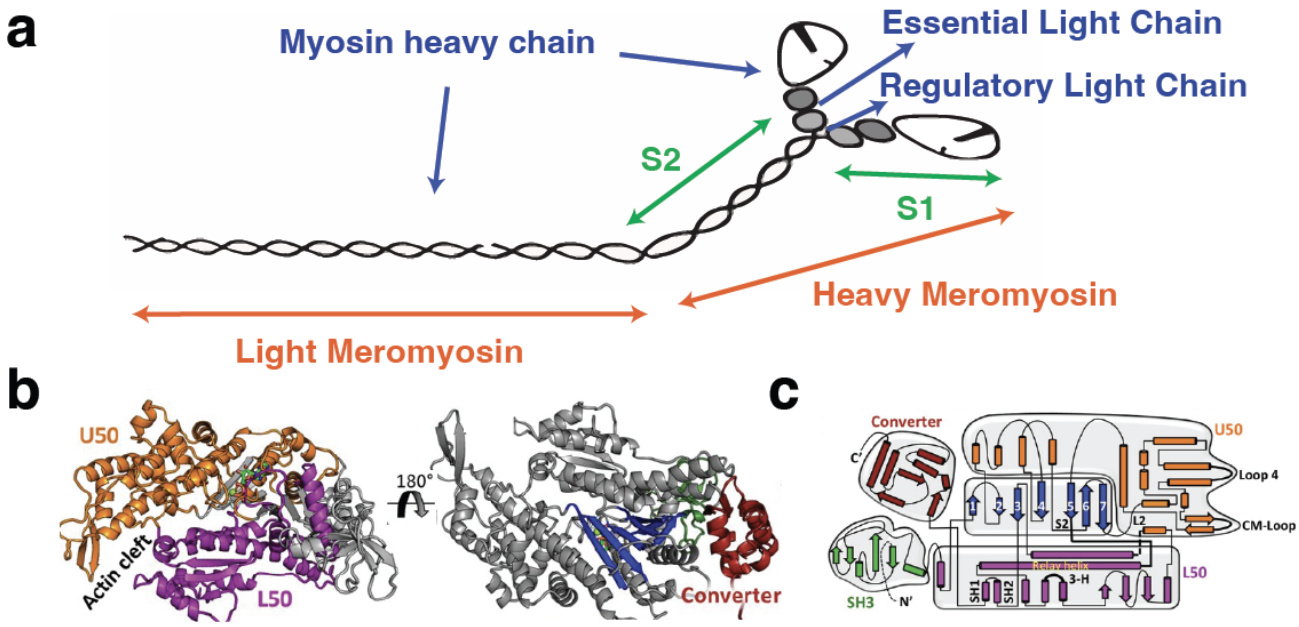

Figure A9 – Structure and domain organization of the myosin molecule.

a, *Myosin II comprises two myosin heavy chains, two essential light chains, and two regulatory light chains. Its domain can be described based on the digestion products from trypsin (orange labels) and papain (green labels) (see main text).* ***b,*** *The various domain of a myosin motor (class XIV) are highlighted and* ***(c)*** *depicted in a topology map. Panel* ***b*** *and* ***c*** *are adapted from* (Powell et al. 2018) *under CC-BY license.*

Tails organization within the thick filament

Early X-ray crystallography and cryo-EM data found that myosin exists in two conformations: It was shown that the long lever-arm undergoes a 60-70° rotation between the beginning and the end of the powerstroke (reviewed in (Geeves and Holmes 1999)). This rotation changes the molecular environment in the active site (OPEN to CLOSED) and controls phosphate release. At the same time, binding to actin mediates the transition from CLOSED to OPEN.

More recently, cryo-EM analysis of isolated myosin molecules has unveiled the near-atomic resolution reconstructions of myosin II in the autoinhibited state (S. Yang et al. 2020; Heissler et al. 2021; Grinzato et al. 2023). At the same time, the analysis of the thick filaments isolated from various organisms provided structural data of the myosin where the tail bundle together in the thick filament. In particular, cryo-EM analysis of insect flight muscles resolved the thick filament to 5-7 Å in bombus (Li et al. 2022), *Drosophila melanogaster* (Daneshparvar et al. 2020), and lethocerus (Hu et al. 2016). The organization of the myosin tails was also resolved by cryo-EM in the thick filaments from tarantula (Alamo, Koubassova, et al. 2017; Woodhead et al. 2005). The arrangement of the tails varies depending on the organism but in all these muscles, the tails run almost parallel to the filament axis and are packed as curved molecular crystalline layers (J. M. Squire 1973).

The myosin tail sequence exhibits a characteristic seven-residue heptad repeat, a hallmark of coiled-coil structures. Additionally, it displays a distinctive dipolar charge profile spanning 28 amino acid residues, which is thought to facilitate the staggered assembly of adjacent rods within the thick filament (McLachlan and Karn 1982). In sarcomeric myosins, the cyclic pattern is interrupted by four extra amino acids known as "skip residues" and are widely spaced along the tails. They are insertion of a single residue and introduce discontinuity in the phasing of the heptad repeats, causing a deformation in the α-helical coiled-coil. As a result, the tails show a local unwinding of the two α-helices and local flexibility (Taylor et al. 2015; Rahmani et al. 2021).

As previously described, the vertebrate thick filament has a 3-fold rotational symmetry and its length, which is ruled by titin, is 1.6 μm. On the other hand, invertebrates show significant variation, both in rotational symmetries and in lengths: the axial repeat is 145 Å and the rotational symmetries range from fourfold to sevenfold (Vibert and Craig 1983), with no threefold symmetry ever been observed .

In mammalian, the organization of myosin within the thick filament remains elusive. Reconstruction of the thick filaments from vertebrates has remained limited to a resolution of 28-30 Å (Zoghbi et al. 2008; Al-Khayat et al. 2013; Luther et al. 2011). While these reconstructions provided insights into the helical arrangement of the myosin heads onto the thick filament, the arrangement of the coiled coils could not be resolved, limiting our understanding of the mechanistic details of myosin regulation in human.

Regulation of myosin's activity within the thick filament

As previously mentioned, all myosin motors are product-inhibited enzymes that hydrolyse ATP (ATPases) when not interacting with actin. The release of hydrolysis by-products, Mg^{2+}-ADP, and inorganic phosphate (Pi), occurs slowly unless the myosin binds to an F-actin filament. Upon F-actin binding, myosin triggers the release of Pi which is then followed by the release of Mg^{2+} and ADP. Next, ATP binding induces myosin dissociation from F-actin, allowing hydrolysis to reoccur, re-initiating the cycle. The structural adjustments upon hydrolysis result in a significant movement of the myosin lever arm and this motion is reversed when the products are released while the myosin head is bound to F-actin. This constitutes the myosin power stroke, which generates force and movement, pulling the thin filaments toward the centre of the sarcomere, resulting in contraction. The movement of the lever arm associated with hydrolysis is termed the recovery stroke (Ruppel and Spudich 1996; Sweeney, Houdusse, and Robert-Paganin 2020).

In order to limit energy consumption and allow muscle relaxation, all subtypes of myosin II evolved regulatory mechanisms that can reduce myosin activity. Early studies on myosin activity observed a reduced (slower) ATP turnover rate in myosin that is incorporated in the sarcomere and higher (faster) ATP turnover when the myosin is present in solution. This suggests that some of the interactions taking place in the sarcomere inhibit the ATPase activity (Stewart et al. 2010). After this initial breakthrough study, more studies continued to evolve our understanding of myosin's enzymatic regulation.

In current models, depending on the speed of ATP hydrolysis and in particular on the ATP turnover rate, we can distinguish four main myosin states: an actin-activated state, represented by a very fast turnover rate (~10/second), a disordered-relaxed state (DRX) with a fast turnover rate (<0.1/second), a super-relaxed state (SRX) with a slow turnover rate (<0.01/second), and a hyper-relaxed state (HRX) with a very slow turnover rate (<0.001/second) (reviewed in (Roger Craig and Padrón 2022)) (Fig. A10). A question that has driven several lines of research during the past decade is how myosin can control the switch between the different kinetics. The switch from an active to a relaxed state appears relatively intuitive and can be found in the structural state of the thin filament: in absence of Ca^{2+}, the myosin binding sites on actin are shielded and therefore myosin can only be present in its active state during Ca^{2+} influx. However, the transition from SRX to DRX (and viceversa) is far from be completely understood.

In mammalian striated muscle, myosin has been found to exist in two kinetic states associated to SRX and DRX states. It has been estimated that in relaxed skeletal muscle about 50% of myosin is present in the DRX state, while the remaining 50% is in the DRX state (Stewart et al. 2010). Interestingly, fluorescent-ATP studies from Neil Kad's laboratory, showed that the distribution of SRX myosin is relatively even along the thick filament, but that pharmacological relaxation with Mavacamten switches the myosin from the DRX to the SRX state, particularly in the D-zone (Pilagov et al. 2022).

Whether the kinetically-defined SRX is associated to a specific structural conformation of myosin has been highly debated over the past 10 years and no studies have been able to directly link this myosin state to a specific structure. Nevertheless, it has been proposed that the SRX state could be associated to the structurally-defined "interacting-heads motif" (IHM) (Roger Craig and Padrón 2022).

In 1983, it was suggested that myosin activity could be regulated by forming a folded-back conformation in non-muscle myosin (Vibert and Craig 1983). Additionally, structural data from Kenneth Taylor's laboratory on dephosphorylated myosin from smooth muscle suggested that the heads fold back onto the proximal part of the tail. In this conformation, the two motor domains interact with each other and form a triangular shape (Wendt et al. 2001). This structure was also observed by Raul Padron, Roger Craig and colleagues in the tarantula's thick filament (Woodhead et al. 2005) termed the "interacting-heads motif" (IHM). The two asymmetrically oriented heads were label "blocked" and "free" head (BH and FH, respectively), evoking a supposed different capacity to bind the thin filaments and were suggested to represent the inhibited state of myosin (Wendt et al. 2001; Woodhead et al. 2005; Alamo et al. 2008). In the thick filament, the IHM is closely associated with the filament core while the myosin in the open/activated state are not helically ordered and project out towards the thin filaments, ready to interact with F-actin (Brunello and Fusi 2024). The IHM has been found in very primitive animals lacking muscles, such as in the Porifera phylum, indicating that it likely emerged 700-900 million years ago. It is highly conserved across the phylogeny of myosin II and has been also identified in smooth, skeletal and cardiac muscles (Schmid and Toepfer 2021).

The activation state of myosin is controlled both by mechanical, biochemical, and physical regulatory mechanisms in the thick filament. The length dependent activation (LDA) of the thick filament is a mechanical activation that is induced upon stretch and is thought to be the molecular basis for the Frank-Starlin law observed in heart and muscle physiology. The process is not yet completely understood but evidence accumulates, which suggests that LDA is primarily dependent on the I-band and A-band portions of titin, as well as on MyBP-C in the C-zone (Marcucci 2023). These structural components of the sarcomere can "sense" strain and relay it to the myosin tails and heads, promoting their switch from the helically ordered OFF state to the disordered ON state. While the structural basis for this phenomenon remains, it has been reported that upon tension, the A-band portion of the thick filament can experience an elongation of ~1%, resulting in the recruitment of more heads in the ON state, in closer proximity to the thin filament (Linari et al. 2015; Brunello et al. 2020).

Another important regulatory factor for myosin-based activation of the sarcomere is temperature. Different studies demonstrated that higher temperature can increase the amount of myosin heads in the helically ordered OFF state (observed by small angle X-ray diffraction and LCs fluorescent probes). This state additionally shows the biochemical signature of the SRX state, which has a slower ATP turnover rate (Stewart et al. 2010; Xu et al. 2003; Fusi et al. 2016; Caremani et al. 2019).

The thick filament can be directly activated by Ca^{2+}, too. In invertebrates such as scallops, Ca^{2+} can bind to the ELCs and favor the cycling of the cross-bridges (Szent-Györgyi 2007). In tarantula skeletal muscle and vertebrate smooth muscle, Ca^{2+} binding to calmodulin activates myosin light chain kinase, which upon phosphorylation and activation of the RLCs, leads to the activation of myosin (Padrón et al. 2020). Additionally, X-ray and biochemical data from Thomas Irving's laboratory recently proved that mammalian cardiac thick filaments are also directly regulated by Ca^{2+} and activated in its presence (Ma et al. 2022).

Pharmaceutical targeting of cardiac myosin has been an extensive field of research for decades. Small molecules capable of modulating myosin activity are important tools for medical intervention in patients affected by muscle and cardiac diseases, such as dilated and hypertrophic cardiomyopathy. Additionally, those small molecules can be used for biochemical investigation of muscles.
Here, I will briefly describe the effect of two different molecules, which can act on myosin II: blebbistatin (Straight et al. 2003) and mavacamten (Green et al. 2016). These compounds and their derivates have been reported as myosin inhibitors and inhibit muscle contractility by binding to β-cardiac myosin.

Blebbistatin is an ATPase inhibitor that acts by binding to the 50 kDa domain of myosin, preventing its closure (Allingham, Smith, and Rayment 2005). This has an impact on nucleotide turnover in skeletal sarcomeres and can promote the helical arrangement of myosin heads in the cardiac thick filament, although it does not directly affect the SRX population. Instead, blebbistatin appears to slow the ATPase rate of the pre-existing SRX myosins (Gollapudi et al. 2021).

Mavacamten is a particularly potent allosteric inhibitor of cardiac myosins (Santini et al. 2020). It inhibits the phosphate release and generated significant interest in the community for its specificity toward the enzymatic pocket of the cardiac isoform of myosin (Green et al. 2016). This property makes mavacamten an effective drug to specifically target the cardiac tissue and to therefore target cardiomyopathies. This capacity was investigated and demonstrated by Anderson and colleagues (Anderson et al. 2018) in a cardiac fibers containing disease mimicking mutations: in these model systems, mavacamten counteracts the depopulation of the SRX state and restores a nominal SRX ratio. A similar effect was reported in muscle fibers containing mutations in cMyBPC. Here, mavacamten mediates the re-population of myosins in the SRX state (Toepfer et al. 2019). EM experiments of negatively stained single particles of the human β-cardiac 25-heptameric heavy meromyosin show an increase in heads folding into the IHM conformation upon treatment with

mavacamten (Anderson et al. 2018). This has been additionally confirmed by small-angle x-ray scattering (Gollapudi et al. 2021).

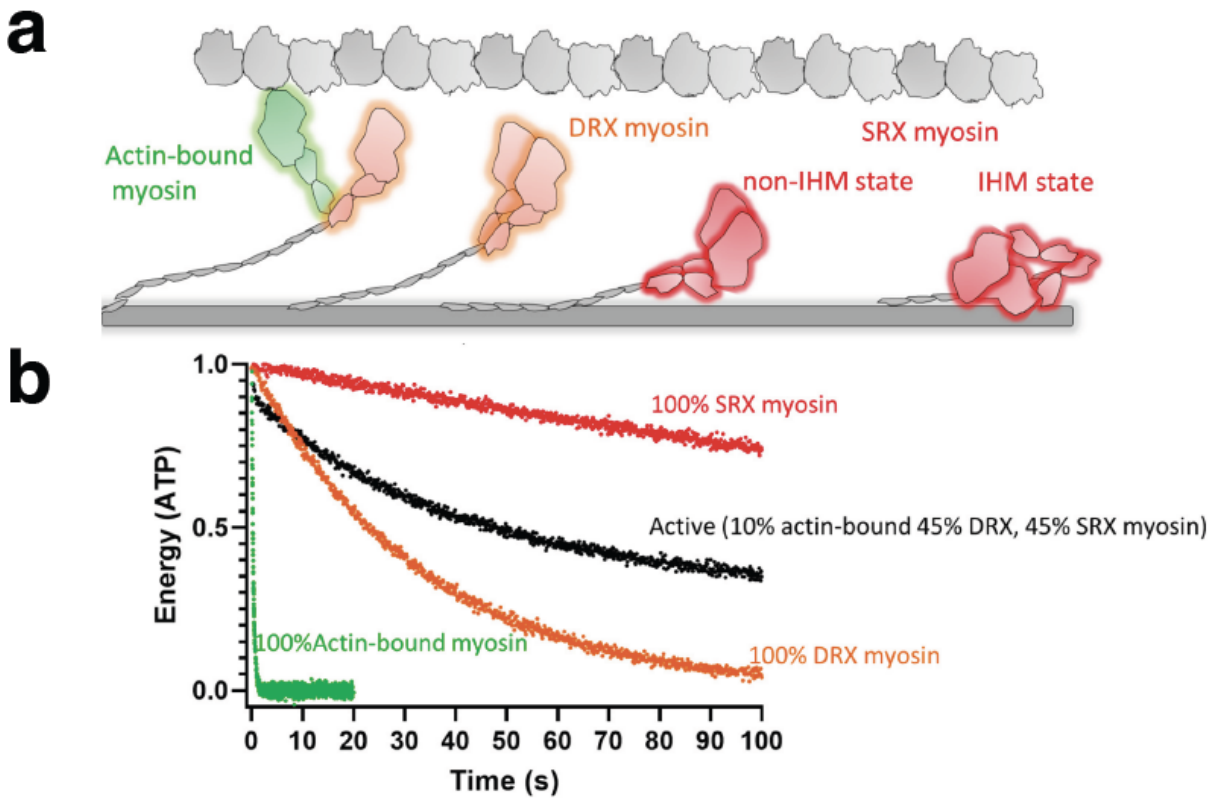

Figure A10 Functional states of myosin and associated ATP-turnover.

a, *Schematic representation of the myosin states and their energy consumptions. Figure adapted from* (Nag and Trivedi 2021) *under license CC-BY.*

2.2.4 Titin

Titin, also known as connectin, is a giant protein with a length greater than 1 µm and it spans half of the sarcomere: the N-terminus is attached to the Z-disc and the C-terminus interacts with M-band components. It acts as a molecular spring regulating the passive mechanical characteristic for muscle (C. A. Henderson et al. 2017). In human, titin is a ~ 3.8 MDa protein encoded by the TTN gene which contains 363 exons and translates into a polypeptide chain longer than 34,000 amino acids (Loescher, Hobbach, and Linke 2022). Titin is predominantly formed by a linear array of fibronectin type III-like domains (Fn3-like domains) and immunoglobulin-like domains (Ig-like domains). Titin can be divided in sub-regions, according to their localization in the sarcomere: Z-disc, I-band, A-band and M-regions (Fig. A11).

In the Z-disc region, we find the so-called "Z-repeats" (45 residue repeating modules) vary in number, depending on the tissue and its development stage, which may be implicated in binding to nebulin/nebulette, α-actinin, and T-cap (C. A. Henderson et al. 2017). The I-band-titin is where most of the passive tension of the sarcomere is accounted for and where a large part of the sarcomere's compliance, contraction and structural stability may be regulated. Here, the N2A and N2B regions are located, which are formed by Ig-like domains. The N2B region is specific for the cardiac isoforms of titin, whereas N2A is present in other isoforms (Adewale and Ahn 2021). The other sub-region in the I-band is the PEVK region, termed after its high prevalence (about 70%) of proline (P), glutamic acid (E), valine (V), and lysine (K) residues. Altogether, the I-band segment of titin provides a platform that can fine-tune the passive tension of the sarcomere in response to mechanical demand and exercise. This happens in a dynamic process controlled by various factors, such as protein kinases and the Ca^{2+} level.
Furthermore, each tissue can specifically tune the ratio of N2A and N2AB isoforms expressed in the muscle to provide increased or reduced passive stiffness: The N2B isoform with fewer extensible spring regions or N2BA isoform containing more extensible regions (N2A, N2B and PEVK regions) (C. A. Henderson et al. 2017).

In the A-band, titin contains two types of domains in the distal and central region respectively: the D-type super-repeat (D-type SR) and the C-type super-repeat (C-type SR). There are six D-type SR and eleven C-type SR. The D-type SRs contain a repetitive pattern of 7 domains arranged as follows: Ig-like, Fn3-like, Fn3-like, Ig-like, Fn3-like, Fn3-like, Fn3-like. On the other hand, the eleven C-type SRs, contain a repetitive pattern of 11 domains arranged as follows: Ig-like, Fn3-like, Fn3-like, Ig-like, Fn3-like, Fn3-like, Fn3-like, Ig-like, Fn3-like, Fn3-like, Fn3-like (Fig. A11). The C-type SRs localise in the C-zone and immuno-fluorescence microscopy data shows that these regions co-localize with the MyBP-C stripes observed in the C-zone (Tonino et al. 2019).

In the M-band, titin harbours the region known as the 250 kDa carboxyterminal region (W. M. Obermann et al. 1996). This region contains the peculiar titin kinase domain (TK domain) (Mayans et al. 1998) followed by 10 Ig-like domains, which acts has an interaction hub for several M-band associated proteins such as myomesin 1 and 2, obscurin, obsurin-like protein, muscle-RING-finger-proteins (MURFs) and others (W. M. J. Obermann et al. 1997; Lange et al. 2020).

Mutations in the TTN genes are commonly associated with inherited myopathies and they are generally referred to as “titinopathies”. Around 130 pathogenic mutations have been linked to striated muscle myopathies, mostly represented by truncations, resulting in a loss-of-function (Rees et al. 2021). Yet, the exact mechanism and underlying structural details of these mutation are not fully understood. The structural data available on titin is limited to NMR or X-ray studies of individual domains and do not offer high resolution detail on the organization of this protein in its native environment (reviewed in (Krüger and Linke 2011)). Interestingly, the exact stoichiometry of titin on the thick filament is still debated with estimates ranging from 2 to 10 chains of titin per half-thick filament (Eldemire et al. 2021).

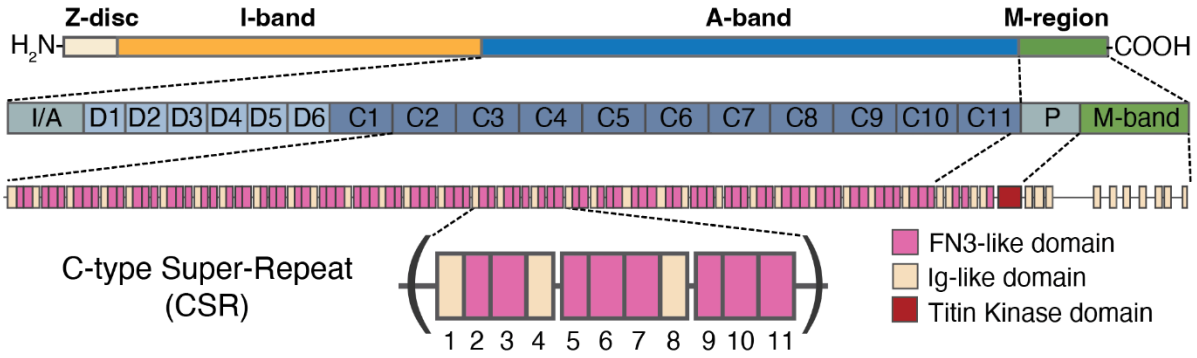

Figure A11 Titin domain map.

General organization of titin and its domain. In the C-zone we find the typical 11x super-repeat. Figure from (Tamborrini et al. 2023) *under licence CC-BY 4.0.*

2.2.5 Myosin Binding protein C

Myosin-binding protein C was initially discovered in the 1970s as a contaminant of myosin purification from skeletal muscle (Offer, Moos, and Starr 1973). The contaminants were classified based on their size and MyBP-C (also known as C-protein) was the third one, hence the letter “C”. In the same family of myosin-binding proteins, we also find MyBP-H was names following the same principle. Both proteins localize in the A-band (specifically in the C-zone) and form transverse stripes 43 nm apart from each other. The exact number of stripes varies from species to species and in both, mouse and human, we observe nine of them (Bennett et al. 1986; R. Craig, Offer, and Boycott 1976; Gilbert et al. 1999). MyBP-H is only expressed in fast twitch skeletal muscle and in the Purkinje fibers of cardiac tissue (Bennett et al. 1986; Alyonycheva et al. 1997).

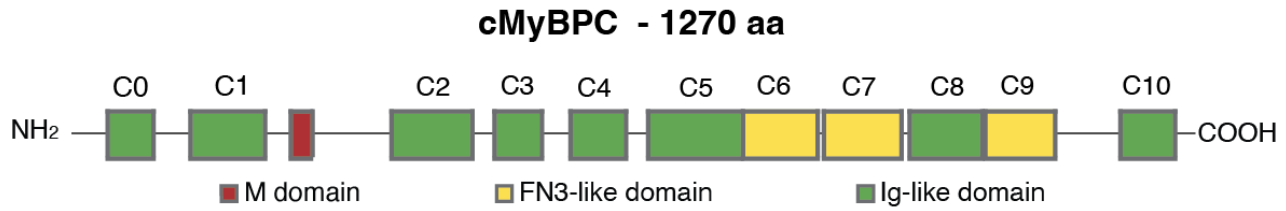

Figure A12 Domain organization of the cardiac isoform of MyBP-C.

cMyBP-C comprises 11 domains, from C0 to C10 and an additional M-domain located within the disordered link between C1 and C2.

Structurally, MyBPs consists of a sequence of four to eleven Ig-like and Fn3-like domains. MyBP-H is a small isoform that only contains four domains followed by a unique N-terminal region, which is rich in proline and alanine. MyBP-C isoforms, on the other hand, contain ten or eleven domains, named from the N-terminus to the C-terminus, from C0 to C10 (Fig. A12). They are divided in 3 sub-regions: the C-terminal domain from C7 to C10, reported to bind to the thick filament (Kampourakis et al. 2014; Tonino et al. 2019), the bridging domains form C3 to C0, and the N-terminal domain from C0 to C2, which can bind to the thin filament. On the thin filament, it displaces tropomyosin and competes with myosin for actin binding and interacts with thick filament, in particular with the S2 region of myosin and its light chains (Risi et al. 2022; Harris et al. 2016; Ratti et al. 2011). The N-terminus has the greatest variability across all MyBP-C isoforms and contains a proline and alanine rich region near the N-terminus. Between C1 and C2 a phosphorylation motif is located, which is called M-motif and which is targeted by Ca^{2+}-dependent calmodulin kinase II, PKA and PKC (Barefield and Sadayappan 2010; M. J. Previs et al. 2012; Risi et al. 2022). MyBP-C is expressed in three different isoforms: slow, fast, and cardiac - encoded by MYBPC1, MYBPC2, and MYBPC3 respectively. Cardiac MyBP-C (cMyBP-C) is exclusively express in cardiac muscle and shows a few features that are specific for this isoform: the C0 domain at its N-terminus has a 28 amino acid insertion in C5 domain, and a unique amino acid sequence within its M-motif (Gautel et al. 1998). The role of MyBP-C has been extensively studied for decades, yet its precise function has not been fully elucidated. It has been proposed to have both activating and inhibitory capacities on sarcomere contraction, which are mediated by its binding and interactions with thick and thin filaments. The phosphorylation levels of the M-motif can modulate cross-bridge kinetics and high phosphorylation levels have been reported to induce a cooperative acceleration of the myosin recruitment and cross-bridge formation, resulting in an increased amplitude during muscle twitch (Moss Richard L., Fitzsimons Daniel P., and Ralphe J. Carter 2015).

The regulation of the expression and phosphorylation levels of MyBP-C are critical for faithful muscle functionality. This pivotal role manifests in the heart of hypertrophic cardiomyopathic (HCM)

patients, where cMyBP-C represents a key disease gene. Over 350 mutations have been found in cMyBP-C and are associated with various human familial HCM, making MYBPC3 the largest depository of genetic mutations associated with cardiomyopathy (reviewed in (Bonne et al. 1995)). The majority of mutations in cMyBP-C are either missense or frame-shift mutations that lead to the expression of a truncated protein, ultimately inducing a haploinsufficiency of cMyBP-C (Marston et al. 2009). Given the therapeutical relevance, MyBP-C has also been the target of various structural studies. Although there is currently no structural information available on the CTD and its binding to the thick filament, some recent cryo-EM analysis of the NTD propose a model for the binding of the C0-C2 domains to the thin filament (Harris et al. 2016; Risi et al. 2022). These models show a precise and unique binding of NTDs to epitopes on the surface of the thin filament, suggesting that C0, C1, M-motif, and C2 might have a specific arrangement on the thin filament depending on its activation state: At high Ca^{2+} levels, when the NTDs are binding to the thin filament, cMyBP-C can inhibit the actin-myosin interaction while at low Ca^{2+} levels, the NTDs do not compete with the myosin motors but instead promote cross-bridge formation to the adjacent F-actin subunits (Risi et al. 2022). These models have been proposed based on experiments that were performed on reconstituted thin filaments. As such they are limited by the absence of a native surrounding and context (the thick filament with myosin and the CTD of MyBP-C are not present in vitro). Additionally, the observations may be biased due to the use of saturating stoichiometries of NTDs that are not representative of the native environment.

2.3 Cryogenic Focused Ion Beam and Electron Tomography (cryo-FIB-ET)

Electron microscopy offers a mean to observe cellular structures and molecular assemblies with resolution in the nanometre and sub-nanometre range. In this thesis, I used a pipeline based on cryogenic focused ion beam and electron tomography (cryo-FIB-ET): I used cryo-FIB milling to prepare thin lamellae of cardiac myofibrils to then exploit the resolving power of transmission electron microscopy (TEM) and analyse their content. Ultimately, the cryo-FIB-ET pipeline allows to analyse a biological sample in its preserved hydrated and native conditions and obtain a reconstruction of the molecule of interest in it. It requires various steps that I will explain and dissect in the following paragraphs.

2.3.1 Sample vitrification via plunge-freezing

One of the most critical steps in the cryo-FIB-ET pipeline is the vitrification of the sample material. Opposite to other fixation methods, such as chemical fixation, this process that preserves the native state of the cellular content by rapidly cooling the hydrated sample, allowing the formation of vitrified amorphous ice. This step is essential as it makes the sample content conducive to TEM and subsequent high-resolution imaging and reconstruction, preventing the formation of ice crystals that would otherwise disrupt its integrity and interpretability (Jacques Dubochet et al. 1987).

To achieve this, the sample must first be loaded onto a cryo-EM grid. These grids have standardized dimensions in order to be compatible with all instruments of a cryo-ET pipeline while also offering a relatively easy way and flexible way to handle the sample. They have a standard diameter of 3,05 mm but can support different mesh types and materials to accommodate for sample variability but generally share a thin holey carbon layer on top of which the sample is deposited. To analyse biological material, it is generally recommended to use titanium or gold grids to reduce cellular toxicity which could be encountered in the case of nickel or copper grids. Additionally, to simplify the FIB-milling procedures, large mesh sizes are generally preferred as they offer more surface with reduced thickness and increase the area that can be easily milled (Fig. A13a). After applying the sample on the grid, the excess liquid is blotted away and the grid is rapidly plunged into liquid ethane or liquid ethane/propane mixture using commercial or homemade plungers (Hands-Portman and Bakker 2022). Both these liquids are precooled with liquid nitrogen at –180 °C and have high thermal capacity which allows for fast freezing process that pushes the sample and its water content in a vitrified state. The biological material is therefore cryo-fixed in a native conformation with the water preserving the same amorphous hydrogen bond network it had in solution (J. Dubochet et al. 1982). One limitation of this approach is sample thickness: at thickness greater than 5-10 microns the cooling speed within the sample is no longer sufficiently fast to ensure vitrification. This problem can be alleviated by the use of cryo-protectants or, alternatively, high-pressure freezing which can help vitrification of samples with a thickness up to 200 micron (Kaech and Ziegler 2014).

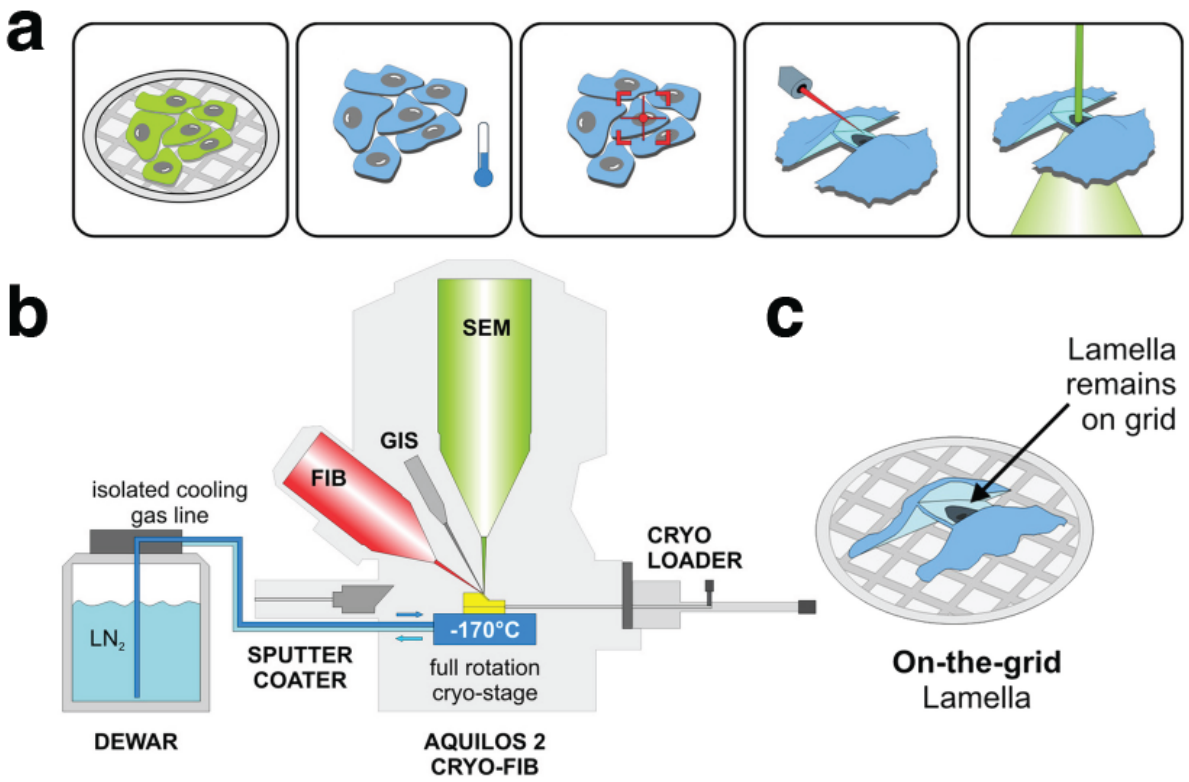

Figure A13 Pipeline for the preparation of a lamella from biological sample.

a, *Cells are grown on cryo-EM grids, plunged frozen and thinned with a FIB before being imaged with cryo-ET.* ***b,*** *Diagram of a dual-beam microscope: the sample it kept at cryogenic temperatures on a cryo-stage, image with a SEM and milled using the FIB.* ***c,*** *The resulting lamella is sufficiently thin to be imaged via cryo-TEM. Images adapted from* (Kuba et al. 2021) *under license CC BY-NC 4.0.*

2.3.2 FIB-milling

High-energy electrons to strongly interact with matter, which increases the probability of an electron to scatter multiple times within the sample and losing energy. Therefore, to take successfully images via TEM, the sample thickness should not exceed the total mean free path of the electron accelerated at voltages of 300 kV(Danev, Yanagisawa, and Kikkawa 2019). A sample thickness of 200-300 nm represent the best compromise to favour elastic interactions and limit inelastic interactions (Martynowycz et al. 2021). The analysis of viruses, small organelles, and bacteria can be performed right after vitrification as the thickness of the sample does not limit data acquisition (Baker, Grange, and Grünewald 2017). However, the analysis of muscle fibres and other thicker biological material, requires sectioning and thinning steps prior to TEM analysis. Mechanical sectioning (e.g. by ultramicrotomy) induces artifacts that impair the quality of the sample. In this study, we circumvent this limitation using the recently developed FIB-milling approach. FIB-milling was initially

introduced as a specimen preparation and analysis for material science applications, however it has been recently adapted to biological samples too, with the first demonstration reported by Michael Marko and colleagues (Marko et al. 2006). The underlying principle is based on the usage of a high current focused ion beam (generally gallium) that can be targeted to ablate the material in a controlled manner, removing matter in a tuneable rate thought a spattering process (Schaffer et al. 2017). Similar to SEM, FIB scans the surface of the specimen and generates secondary electrons and ions that can be detected, generating an image. FIB microscopes are generally associated to a SEM in a dual-beam microscope, where the two beams are placed almost orthogonally one to the other and allow for simultaneous milling (FIB) and imaging (SEM) of the specimen, which is kept in vacuum and cryogenic temperature (Fig. A13b). Using this approach, biological material above and below the region of interest can be precisely removed to generate an artifact-free lamellae of the desired thickness while also preserving the hydrated sample in its vitreous state (Fig. A13c). These advancements in cryo-FIB-milling synergised with cryo-ET to help visualize molecular details within the cell with unprecedent detail (Mahamid et al. 2016; Berger et al. 2023). This pipeline also offers great potential for the analysis muscle fibers in their native state and it has been successfully employed in Stefan Raunser lab to obtain the first high-resolution reconstruction of the thin filament and its native surrounding (Wang et al. 2021; 2022).

2.3.4 Cryogenic transmission Electron Tomography (cryo-ET)

Transmission electron microscope: hardware and image formation

Structural analysis at the nanoscale has been revolutionized by Transmission Electron Microscopy (TEM) and recent advancements in Cryo-Electron Microscopy (Cryo-EM) and Cryo-Electron Tomography (Cryo-ET) further expanded the reach of these approaches to biological sample. These techniques have led to exceptional discoveries in the understanding of complex biological macromolecules, cellular structures, and intricate biochemical processes. In this chapter, I will delve into the principles, methodologies, and recent developments in these structural techniques, with a particular focus on the Cryo-ET pipeline.

TEM is a pivotal tool in the arsenal of structural biology, providing informative reconstructions at nanoscale resolutions. At its heart lies the fundamental interaction of electron beam with biological specimens.

If we observe the diagram of a TEM microscopes, we can follow the electrons from their source, through the sample, and onto the detector (Fig. A14). The TEM column is kept in a vacuum environment and in its top section we find the electron source that allows for the extraction of electrons and their acceleration to 120-300 keV. The electron source can be a tungsten filament, a lanthanum hexaboride crystal or a field emission gun (FEG) and the extraction of the electron can rely upon thermionic emission, field electron emission or a combination of both (Cleaver 1975). Spatial and temporal coherence of the electrons are the most important factor determining the resolutive power of the microscope, as such, a highly coherent cold-FEG provides the best commercially available solution for TEM, generating highly spatially coherent electrons from a tungsten tip of about 100 nm with high temporal coherence thanks to the cold extraction based on field electron emission (Williams and Carter 2009). The electrons are then focused and magnified into a parallel beam through a series of apertures and lenses creating a parallel beam that illuminates the sample with a probe of a few micrometers in diameter. A common TEM set-up consists of three main lens systems: condenser lens system, objective lens system, and projector lens system. All lenses are electromagnetic lenses which makes them susceptible to hysteresis and magnetic field asymmetries that are compensated and corrected for by accessory stigmators placed both in the column and in the energy filter system. The sample holder is located between the objective lenses and it actively cooled in order to keep the sample at cryogenic temperatures. After the objective lens system, the beam enters in an energy filter system connected to the camera. The atoms in the specimen scatter the electron beam, changing the amplitude and the phase of the electron wave and thereby generating amplitude contrast. Highly scattered electrons can be removed to improve contrast via the objective lens system or using an energy filter to select electrons with a relative high energy coherence (+/- 10 eV) to reach the detector and create the final image.

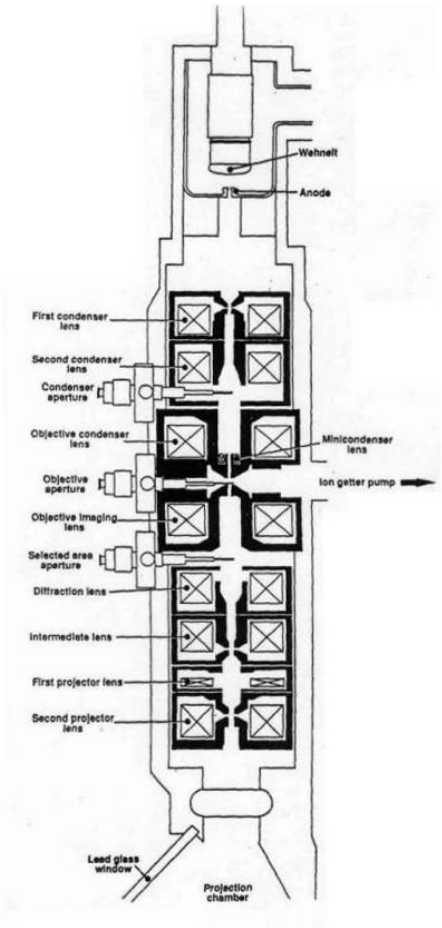

Figure A14 Diagram of a TEM column.

Schematic view of a transmission electron microscope column depicting the position of the various elements: the electron source at the top, the lens systems and specimen holder, and the projection chamber. Figure from (Venturi 2018) *used under licence CC-BY licence.*

Image formation requires phase and/or amplitude contrast. On the detector, amplitude contrast is generated by the removal of inelastically scattered electron and high-angle elastically scattered electrons while the phase contrast is formed by the interference of the elastic scattered electron wave with the unscattered electron wave. Biological samples are weak-phase objects generating a low contrast. This is exacerbated by the low-dose required to not induce drastic radiation damage affect sample integrity. A traditional approach to increase contrast is to apply a few micrometres defocus in the objective lens, this convolutes in the point-spread function (PSF) of the resulting image. With this approach we can more easily calculate (fit) the contrast transfer function (CTF) in Fourier space and reconstruct the original image. The CTF describes how the microscope, and the lens systems modulate and transfer the contrast in the final image. The CTF can be describes as a complex band pass filter and can be mathematically described as a sinusoidal curve which amplitudes oscillates as a function of the special frequencies. Its exact shape depends on lens aberrations (specific for each microscope and each lens setting) and on the applied defocus. Accurate defocus estimation is

paramount to calculate an accurate fitting of the CTF and recreate the original image. In this context, it is worth mentioning that while high defocus favours contrast and object detection, it comes with the downside of delocalizing the high frequencies information far from the centre of the image and also induces a dampening of the amplitude at high frequencies that increases the error of CTF fitting of high-resolution imaging (Glaeser et al. 2021).

Energy filters are particularly important when acquiring data on relatively thick samples (e.g. FIB-milled lamellae) as they allow to efficiently reduce the noise generated by inelastic scattering from entering the detector. While older system rely on in-column Ω-filters, nowadays most energy filters are post-column systems based on the GIF200 design introduced by Krivanek and colleagues (Krivanek, Gubbens, and Dellby 1991). They consist of an electrostatic shutter that precedes a bent magnetic section which redirects the beam thought an energy selecting slit, followed by a series of quadrupole and sextuples lenses that can correct image aberrations and distortions. Most recent systems contains additional octupoles and decapoles and can correct up to the fourth order of aberration, providing improved isochromaticity at larger apertures (i.e. improving signal amplitude and acquisition speeds) (Gubbens et al. 2010).

The electrons are finally collected by the detector, the final element of the TEM. Since 2008 the increased commercial availability of direct detections camera allowed for a significant improvement in acquisition speed and resolution of TEM images (Kühlbrandt 2014). As the bypass the need for a scintillator and photomultipliers, direct detection camera provide reduced lateral spread of the electron and smaller physical pixel sizes, resulting in increased detective quantum efficiency, improved acquisition speed and resolutive power (Faruqi and Henderson 2007).

As the beam interacts with the specimen it induces damage that disrupt the high-resolution information in it, at the same time this interaction results in motion within the sample (Grant and Grigorieff 2015). To correct for motion and to account for radiation damage, each exposure consists of multiple frames. These movies can later be post-processed to perform motion correction, defocus estimation, CTF estimation, and dose-weighting, improving image quality post-acquisition (Tegunov and Cramer 2019; Tegunov et al. 2021).

Tomographic data acquisition

In cryo-ET, during the acquisition of a region of interest (ROI), the sample is places at eucentric Z-height and it is imaged at different tilt angles. In an ideal scenario, in order to obtain the most accurate

and complete representation of the ROI, one would need to acquire a continuous movie to record a 180 degree rotation along two axis. However, in reality the acquisition strategy is dictated by mechanical and physical limitations in specimen tilting as well as limitations in the exposure the sample can be subjected too before being irremediably damaged.

As we tilt the 200 nm thick specimen, its thickness along the electron beam axis increases too, according to Euclidian geometry. This increases the length of the path the electrons have to travel though the sample to the point where the ratio of elastically scattered electrons vs inelastically scattered electron is too low and can no longer produce a usable image. Moreover, the sample holder in a TEM, can only rotate along one of the axes of the specimen from -70° to + 70°, limiting the total range to about 140°. In principle, the specimen could be rotated in plane by 90° and another tilt series along the remaining axis could be acquired. However, the radiation damage is also limiting the total dose and therefore the total number of images per ROI.

Generally speaking, after an exposure of about 10 $e^-/ Å^2$, high resolution information present in the biological samples is lost due to radiation damage (Xue et al. 2022). Furthermore, after 140-160 $e^-/ Å^2$ (depending on sample thickness and specific composition) the radiolysis reactions under the electron beam becomes so severe that the hydrogen is released in gaseous form and induces the formation of molecular hydrogen bubbles that determine that ultimate destruction of the ROI (Leapman and Sun 1995). During acquisition at high-magnifications (53'000-105'000x), in order to have sufficient contrast to correct for motion and fit the CTF as previously described, during each image acquisition the sample must be exposed to 2.5-6 $e^-/ Å^2$, limiting the tilt series acquisition to the about 30-60 images per ROI. To balance and optimize these factors, a typical acquisition covers tilts from -60° to + 60°, with steps increments of 2.5-3°. Different tilt-scheme can be employed to collect the various tilt-images. For instance, a dose-symmetric tilt-scheme allows for the best "dose-economy" as it acquire the first images at low-angle tilts us, ensuring reduced drift and increased defocus accuracy (Hagen, Wan, and Briggs 2017).

Tilt-series alignment and tomogram reconstruction

After the acquisition of the 2D images during tilt-series, we need to reconstruct a 3D tomographic by back-projecting the images and fill the 3D Fourie space. This process requires a precise understanding of how each point of the volume was projected onto the acquired 2D images. During tomographic data acquisition, each image of the tilt series has a relative orientation determined by the acquisition parameter. These parameters are rough reads out from the sample holder within the TEM and must

be most precisely calculated and refined to guarantee the highest possible tomogram reconstruction. This is a pivotal step that corrects for shifts, rotations, and distortions between projections (Amat et al. 2010). The first course alignment step is generally based on cross-correlation between adjacent images (Guckenberger 1982) but it requires further tuning to extract high-resolution information from the tilt-series. For this purpose, it is possible to track the movement specific features within the images across the tilt-series. To ensure the presence of high-contrast features, the sample can be pre-submerged in a solution containing gold particles that will deposit on the surface, alternatively, in the cases of FIB-milled material, the random platinum particles deposited on the lamellae during can also be exploited and provide sufficient signal to cross-correlate across the tilt-series (Wan and Briggs 2016). These approaches are called "fiducial tracking" and are particularly useful in low signal-to-noise ratio (SNR) samples such as typical biological cryo-ET specimen. Nevertheless, these tilt-series can also be aligned using image patches and calculating their cross-correlation throughout the tilt-series in a "patch tracking" approach that has proven its adequacy in a number of biological samples (Amat et al. 2010). Both fiducial and patch tracking result in a geometric model that describes the refined posed of each image and accounts for magnification distortion, shift of the ROI, stage geometry, beam-induced motion, and sample deformation. This model is then used to reconstruct the final tomogram via number of different available methods (weighted back-projection methods, iterative reconstruction methods, etc.) (Wan and Briggs 2016).

Subtomogram averaging (STA), 3D refinement, and Fourier shell correlation (FSC)

The final tomogram reconstruction contains a representation of the initial ROI in 3D but this representation is incomplete: because of the limited range of the tilt angles during acquisition, the corresponding 3D Fourier space information for the angles that were not imaged are absent and generate a *missing wedge* that results in anisotropic resolution in real space. One major goal of a FIB-milling-cryo-ET pipeline is to attain structural information on the biological sample (e.g. molecular complexes) *in situ* and most of these targets are present in multiple copies within one or more tomograms. This redundancy can be exploited to overcome two limitations of cryo-ET, namely the low SNR and the missing wedge, using an approach known as subtomogram averaging (STA). For STA, we first need determine the localization and rough orientation of the molecules of interest (particles) by picking them (more details later in this paragraph) to then extract sub-volumes (or subtomograms) of the original tomogram(s) centred on the particles. Several particles (with different poses) can then be merged together to increase the SNR in an iterative process of alignment and averaging (Fig. A15).

The first step in this process is to identify, label and extract the particles of interest. This can be performed manually for small datasets but it becomes exponentially more labour intensive as one attempt to increase the final resolution of the particle reconstruction. In the last few years, several software packages and tools have been developed to obviate this tedious process, streamline the workflow, and help identify poorly represented particles in the vast and heterogenous population of molecules generally found in a cell. These softwares are generally called “particles pickers” and are based on various object detection systems and convoluted neural networks (CNN) that greatly simplified the process of labelling/identify the particles of interest withing the tomograms. Same particle pickers, such as crYOLO, required the user to first pick (label the particles of interest) form a small subset of the dataset in order to train the CNN that can then be deployed on novel, unlabelled, data to recognize the target particles (Wagner et al. 2019).

After picking and subtomogram extraction, the set of subtomograms containing the same particle of interests are pooled together and aligned to a reference to obtain a 3D reconstruction (density map) with increased SNR and resolution in the nanometre and sub-nanometre range. In this thesis, the subtomograms were aligned and averaged using RELION, a software package based on a Bayesian approach that optimizes for a single target function with the use of a gold-standard Fourier shell correlation (FSC) procedure that reflecting the quality of the alignment while also preventing data overfitting (Scheres 2012a; 2012b). RELION operates by performing angular sampling and translational search to align the subtomograms to a reference and then average them to produce a new map that is low-pass filtered according to the FSC (more details later) and becomes the reference for the next round of alignment in an iterative process that tries to optimize the resolution of the output maps by using increasingly higher frequencies and finer sampling of the subtomograms. To better understand this process, we need to introduce the concept of FSC and “resolution” in cryo-EM/ET.

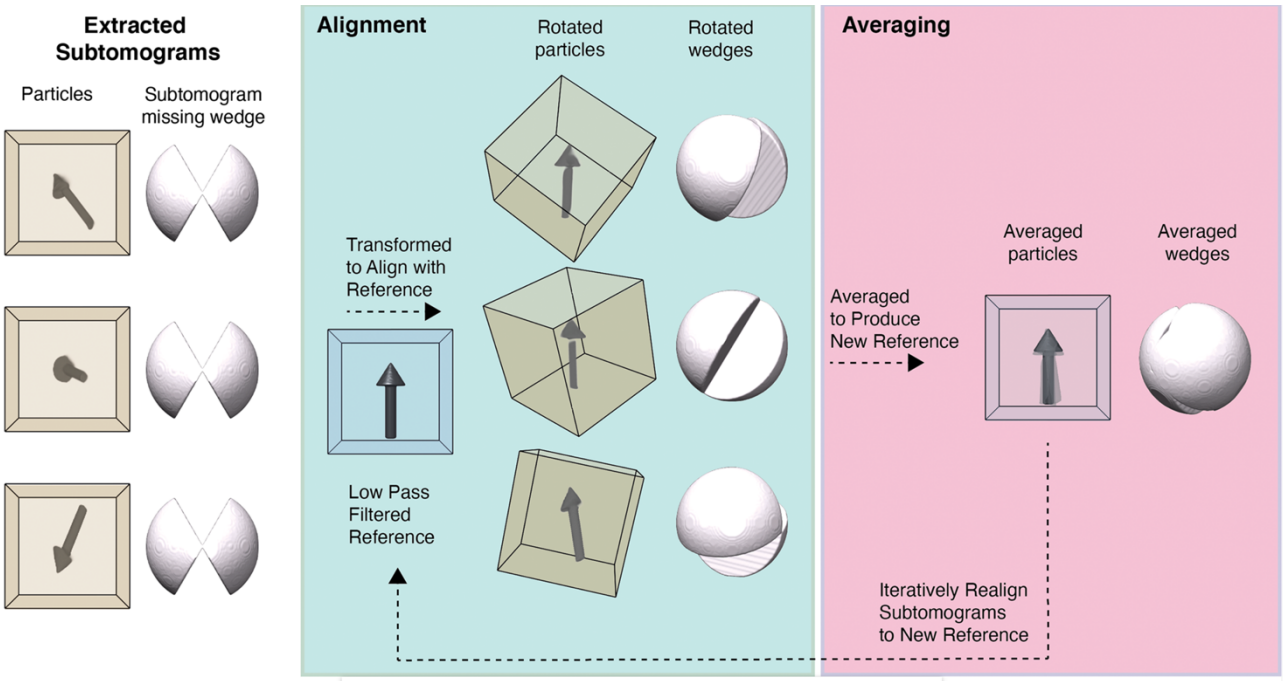

Figure A15 Subtomograms extraction, alignment, and averaging.

After picking the tomographic volume, all subtomograms of interest are extracted, aligned, and averaged. The initial alignment is guided by the priors obtained during picking. Each particle is rotated and translated to match a low-pass filtered reference; all particles are then averaged together to generate a new map that serves as a reference for the next step of alignment. The process is repeated iteratively, improving the quality of the alignment the final resolution of the map. Figure adapted from (Pyle and Zanetti 2021) *under license CC BY 4.0.*

In imaging and optics, the term "resolution" often describes the capability of an object or instrument to resolve two distinct points, more precisely it describes the minimum distance at which two objects can be individually identified and this is a function of the refraction index of the media interposing the observe and the observed points, the numerical aperture of the optic system, and importantly, the wavelength of the light. In electron microscopy, to assess the quality of a reconstruction (map), structural biochemists resort to the FSC, which is the function of the correlation between special frequencies, and define the resolution as the maximum spatial frequency in the map that still contains reliable information (Penczek 2010). During 3D refinement in software packages as RELION, the dataset is divided in two halves and each half is refined starting from the same reference but independently from each other. After various iterations of alignment, averaging, and optimization, the two half-maps converge to similar solution in alignment. The resolution is determined by comparing the Fourier spaces of both maps and calculating the cross-correlation between the two maps at Fourier shells: after a typical refinement, low frequencies shells generally have high correlation between the two half-maps and the correlation decreases as higher special frequencies are analysed and compared. The "gold-standard FSC resolution" has been agreed to be determined as the

spatial frequency at which the FSC correlation between the two independent half-maps falls below 14.3% ($FSC_{0.143}$) (Penczek 2010; R. Henderson et al. 2012). This is called the 0.143-criterion and other criteria with different cut-off thresholds have been proposed to better described the quality of the map such as the 3 sigma-criterion and the 0.5-criterion (Penczek 2010). Regardless of the specific cut-off frequency, these approaches allow scientist to quantify, discuss and compare different maps but they all have a built-in limitation: they do not take into account the shape and slope of the FSC function at spatial frequencies above the threshold, therefore cannot fully and comprehensively describe the quality of the map. For this reason, while the FSC provides a handy number to discuss and mathematically describe the quality of the map, the *real* quality of the final reconstruction should be assessed by visual inspection from a trained eye. Generally speaking, tertiary structure can be recognized at 20-30 Å resolution, finer details such as protein domains and coiled coils appear clearly distinguishable at 16-18 Å, secondary structural elements of the macromolecules start to be resolved around of 8-9 Å resolution, amino acids side chains can be modelled at resolutions of 3-5 Å and water molecules only became clearly distinguishable at 2 Å.

2.4 Aim of the thesis

Over the past five decades, the scientific community has diligently explored the intricacies of muscle organization, employing various approaches from different disciplines and across diverse organisms. This collective effort has significantly advanced our comprehension of muscle physiology and pathologies. However, the more we explored into the complexities of this molecular machine the more we expose the limitations of our understanding of its regulation.

While structural insights from EM analyses of purified components have been pivotal in deciphering some aspects of muscle mechanics, a critical gap existed concerning the structural information on the arrangement of the thick filament in mammalian striated muscle at the commencement of my study. The organization of essential components of the cardiac sarcomere such as myosin, titin, and MyBP-C remained largely uncharted territory.

Throughout my Ph.D. journey, I leveraged the high-resolution capabilities of cryo-electron tomography (cryo-ET) to study the organization of the sarcomere and its constituents in their native environment – *in situ*. My primary objective was to map the molecular organization of thick and thin filaments in cardiac muscle. The ultimate aim was to provide a detailed mechanistic explanation of sarcomere contraction by describing the interactions and arrangements of its various components. This pursuit aimed to address unresolved questions in the field, including the interaction between titin and myosin, the arrangement of myosin tails within the thick filament, the stabilization mechanisms for the interacting head motif (IHM), and the role of MyBP-C.

Answering these questions not only seeks to resolve long-standing controversies but also brings us closer to unraveling fundamental questions: What are the molecular principles governing muscle contraction? And, crucially, why and how do they fail in cardiomyopathies? This research endeavors to contribute to our understanding of these intricate processes, paving the way for advancements in muscle physiology and pathology.

CHAPTER 3 In situ structures from relaxed cardiac myofibrils reveal the organization of the muscle thick filament

In the subsequent section, I present the methods, findings and the discussion from my paper published in Nature (Tamborrini et al. 2023). This publication serves as a crucial foundation for the ongoing research discussed in this thesis.

Contribution from other authors

Stefan Raunser designed and supervised the study. Zhexin Wang helped with the initial reconstruction of the thin filament. Sebastian Tacke, Thorsten Wagner, and Markus Stabrin wrote scripts for particle re-extraction and re-projection. Zhexin Wang, Sebastian Tacke, and Micheal Grange optimized initial FIB-milling and cryo-ET acquisition. Ay Lin Kho and Mathias Gautel developed methods and prepared myofibril samples.

3.1 Abstract

The thick filament is a key component of sarcomeres, the basic force-generating and load-bearing unit of striated muscle (Gautel and Djinović-Carugo 2016). Mutations in thick filament proteins are associated with familial hypertrophic cardiomyopathy and other heart and muscle diseases (Barrick and Greenberg 2021; Ramaraj 2008). Despite this central importance for sarcomere force generation, it remains unclear how thick filaments are structurally organized and how its components interact with each other and with thin filaments to enable highly regulated muscle contraction. Here, we present the molecular architecture of native cardiac sarcomeres in the relaxed state, determined by electron cryo-tomography. Our reconstruction of the thick filament reveals the three-dimensional organization of myosin heads and tails, myosin-binding protein C (MyBP-C) and titin, elucidating the structural basis for their interaction during muscle contraction. The arrangement of myosin heads is variable depending on their position along the filament, suggesting that they have different capacities in terms of strain susceptibility and activation. Myosin tails exhibit a distinct arrangement and pattern of interactions. These are likely orchestrated by three alpha and three beta titin chains that are arranged like a spring, suggesting the existence of specialized roles of thick filament segments in length-dependent activation and contraction. Surprisingly, while the three titin alpha chains run along the entire length of the thick filament, titin beta does not. The structure also demonstrates that the C-terminal region of MyBP-C binds myosin tails and unexpectedly also directly interacts with the myosin heads, suggesting a previously undescribed direct role in the preservation of the myosin OFF state. Furthermore, we visualize how MyBP-C forms links between thin and thick filaments. These findings establish a robust groundwork for forthcoming research endeavors aiming to explore muscle disorders that involve sarcomeric structural components.

3.2 Introduction

Muscle contraction requires a shortening of the sarcomere, the basic contractile unit of muscle, caused by the sliding of interdigitating thick and thin filaments. Thick filaments are bipolar structures containing myosin-II, myosin-binding protein C (MyBP-C) and titin, as well as several other proteins near the bare zone, which marks the thick filament's symmetry axis and the centre of the sarcomere (Lange et al. 2020). By convention, this region comprises the P-zone (P stands for proximal), where the so-called crowns of myosin P1, P2 and P3 are located, and the M-band, a bare zone devoid of myosin heads where tails belonging to apposing half-sarcomeres intertwine (Al-Khayat et al. 2010). Myosin is a 446 kDa complex of a myosin-II dimer whose head or motor domains connect via a neck region to their coiled-coil tails that pack into the thick filament backbone, with each neck bound by an essential and regulatory light chain. Myosin heads are arranged in a quasi-helical array with a 3-fold rotational symmetry in the relaxed state of muscle (Al-Khayat et al. 2008; Caremani et al. 2019; Zoghbi et al. 2008). The pairs of heads of three myosin molecules protrude from the backbone at regular intervals to form a "crown" of heads, with successive crowns axially separated by about 143 Å. The interaction of the myosin motor domains with the thin filament is responsible for force generation and muscle contraction.

MyBP-C localizes in the C-zone which also contains all the myosin motors that are responsible for providing the peak force during contraction (Brunello et al. 2020). The cardiac isoform of MyBP-C (cMyBP-C) is a 140 kDa protein with 3 fibronectin type 3 (Fn3)-like domains and 8 immunoglobulin (Ig)-like domains that can form links between the thick and thin filaments (Main, Fuller, and Baillie 2020). Biochemical investigations support a model in which the N-terminal region can bind both actin and myosin heads in a phosphorylation-dependent manner (Kampourakis et al. 2014; Ponnam et al. 2019), while the C-terminal region docks to the thick filament via interactions with titin and myosin tails (Freiburg and Gautel 1996; Ponnam and Kampourakis 2021). MyBP-C links can act as mechanical sensor for muscle tension and have both activating and inhibitory effects on the myosin motors, fine tuning the strength and the kinetics of the muscle contraction (Finley and Cuperman 2014; Hanft et al. 2021; Rahmanseresht et al. 2021; Michael J. Previs et al. 2016).

Titin is an up to 4.25 MDa protein consisting of up to 169 Ig-like and 132 Fn3-like domains that form a chain from the M-band to the Z-disc, where the actin filaments of opposite polarity are cross-linked by α-actinin, marking the lateral borders of the sarcomeres (Bennett, Rees, and Gautel 2020; Wang et al. 2021). Titin acts as a molecular spring that prevents the overstretching of the sarcomere, recoils

the sarcomere after stretch release (Gautel 2011; Lemke and Schnorrer 2017) and is proposed to act as a molecular ruler for assembly of myosin in the A-band (the region of the sarcomere where thin and thick filaments overlap) (Maruyama et al. 1985; Tonino et al. 2019; Tskhovrebova and Trinick 2012). The exact stoichiometry of titin within the A-band has remained a mystery, with estimates ranging from 2 to 10 molecules per thick filament (Eldemire et al. 2021). With numerous post-translational modification sites scattered along its length and the predicted interactions with myosin and MyBP-C, titin is also proposed to mediate regulatory signals from the cell to the myosin motors (Linke and Hamdani 2014).

Models exist for the general arrangement of myosin heads within the cardiac thick filament(Al-Khayat et al. 2013) and using components reconstituted in vitro, remarkable insights have been gleaned into the regulation of their kinetics (Heissler and Sellers 2016). However, how these observations map onto the structure of a fully complemented, natively organised sarcomere, and the molecular interactions that occur within the thick filament in its native environment is still unknown. In particular, knowledge of key molecular players implicated in disease – myosin, titin, MyBP-C – is completely lacking, demonstrating a key gap in understanding of how they carry out their highly regulated functions within the confined space of the thick filament. Here, we present the *in situ* structure of the thick filament in the M-band, P-zone and C-zone in relaxed mouse cardiac myofibrils determined using our established workflow for focused ion beam (FIB) milling and cryo-electron tomography (cryo-ET) (Tacke et al. 2021; Wang et al. 2022; 2021). The structure reveals in unprecedented detail and completeness the architecture of the thick filament, visualizing critical interactions between myosin, titin, and MyBP-C, as well as MyBP-C links between thin and thick filaments.

3.3 Results

3.3.1 Sarcomere structure of relaxed cardiac myofibrils

To obtain a near-native sample suitable for FIB milling and cryo-ET analysis, we relaxed de-membranated mouse cardiac myofibrils in the presence of EGTA, dextran, and mavacamten (see Methods). Mavacamten, an FDA-approved drug to treat hypertrophic cardiomyopathy, stabilizes the OFF (relaxed) state of myosin (Anderson et al. 2018; Green et al. 2016).

The tomograms showed that the thick filaments were indeed in the OFF state, as defined by the absence of myosin binding to thin filaments (Fig. 1a). Importantly, the tomograms contain structures that could not be visualized *in situ* before. In particular, using subtomogram averaging, we could determine the structure of the cardiac thin filament with tropomyosin in the blocked state (myosin binding site occluded) at 8.2 Å resolution (Fig. 1b,d, Extended Data Figs. 1a,b, 2a,b, 3,a,b, Methods) and the structure of the relaxed thick filament (Fig. 1b,c,e, Extended Data Fig. 1,b 2,b Methods). To tease out greater detail in the analysis of the thick filament, we subdivided the filament into overlapping segments and determined their structures independently, obtaining subtle structural differences between the different segments. The resulting reconstructions ranged in resolution from 19.3 Å to 23.6 Å (Extended Data Fig. 2c-h).

Mapping of the determined structures into their determined XYZ positions within the reconstructed tomograms further enabled us to characterize the 3D arrangement of thin and thick filaments (Fig. 1b, Supplementary Video 1). In agreement with previous structural studies of vertebrate heart muscles, the myosin heads in our combined reconstruction are arranged in a quasi-helical array with a 3-fold rotational symmetry (Al-Khayat et al. 2008; Caremani et al. 2019; Zoghbi et al. 2008) (Fig. 1c, Extended Data Fig. 4). The combined reconstructions comprise the M-band, P-zone, and C-zone and reveal the position of M-band proteins together with the first 31 myosin layers, encompassing 6 titin molecules and 9 cMyBP-C stripes (27 molecules of cMyBP-C) (Fig. 1b,c, 2). This structure of the thick filament has a diameter of 64 nm, a length of 510 nm, and a molecular weight of ~ 67 MDa and enables a description of the thick filament across the entire sarcomere in a region-by-region specific manner.

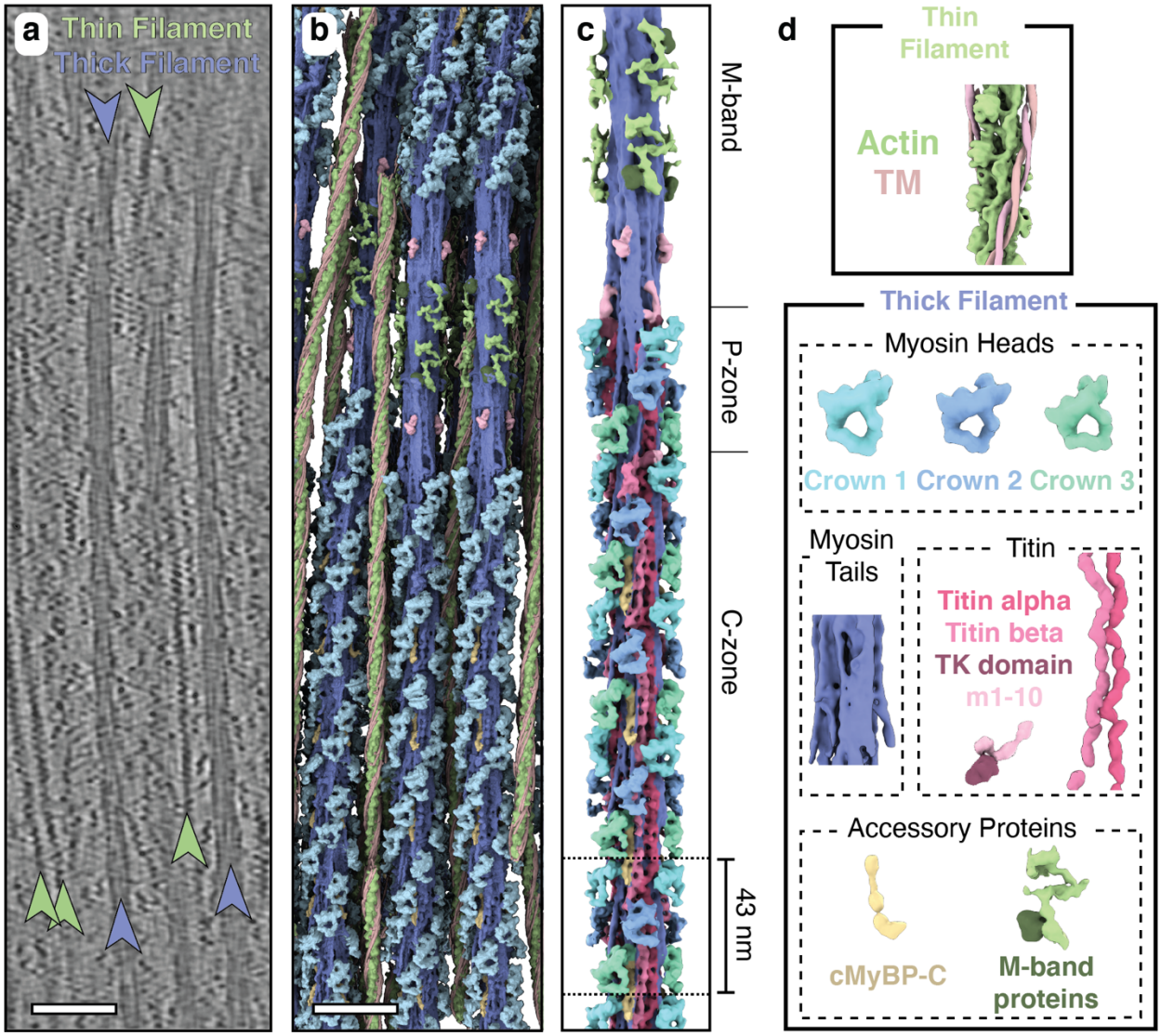

Figure 1 Thick filament structure in the relaxed cardiac sarcomere.

***a**, Tomographic slice of a cardiac sarcomere M-band depicting thick and thin filaments. Scale bar, 50 nm. **b**, Reconstructed thick and thin filaments mapped into a tomogram. Thin filaments obstructing the view on the thick filament were removed for clarity. Scale bar, 50 nm **c**, Structure of the thick filament from the M-band to the C-zone. For clarity, only the first four cMyBP-C stripes are shown here. **d**, Illustration of the various sarcomere components and their color code which is maintained throughout the manuscript, unless otherwise indicated. TM, tropomyosin. TK domain, titin kinase domain.*

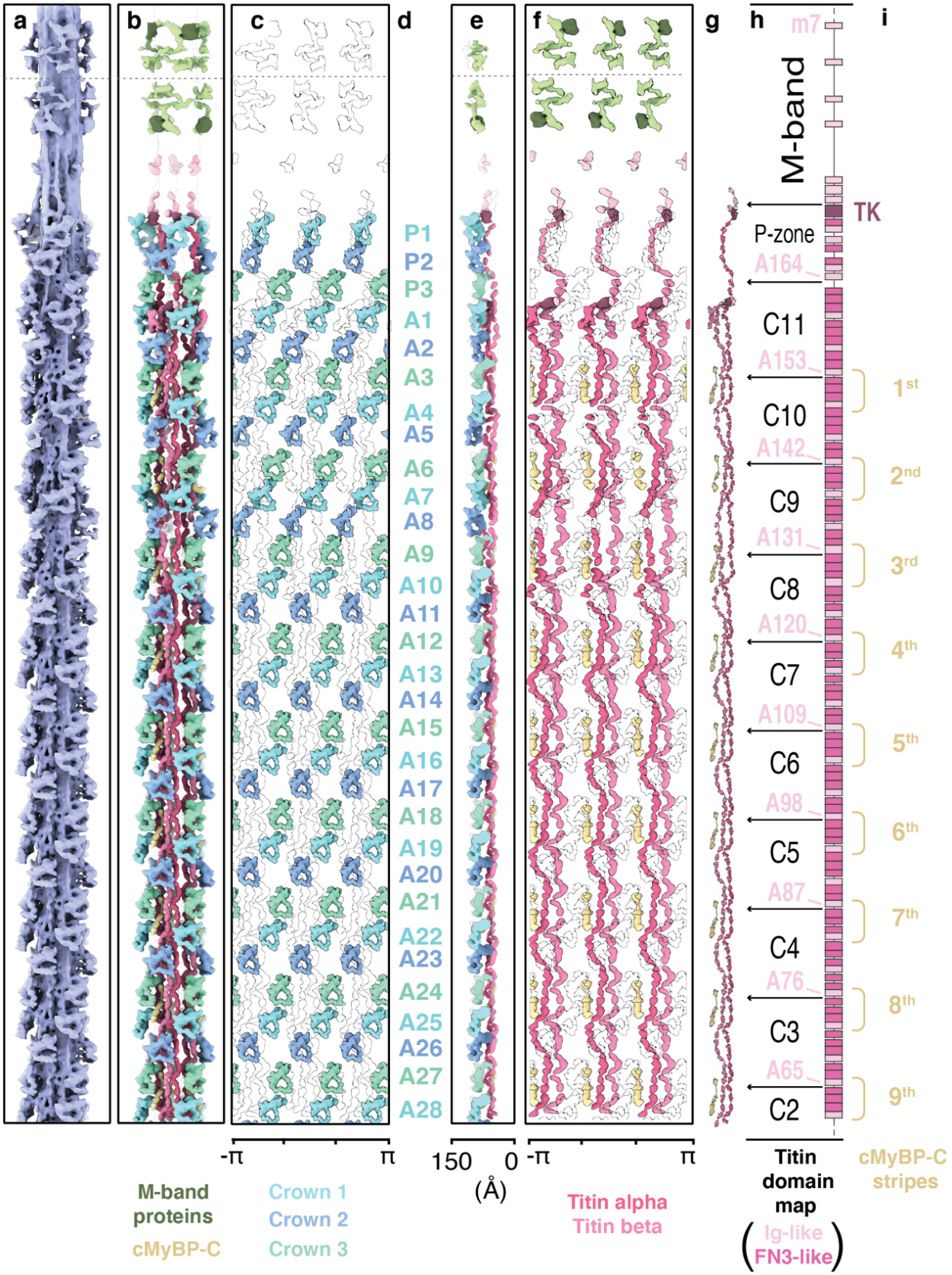
a
b
c
d
e
f
g
h
i
m7
M-band
TK
P-zone
A164
C11
A153
C10
A142
C9
A131
C8
A120
C7
A109
C6
A98
C5
A87
C4
A76
C3
A65
C2
1st
2nd
3rd
4th
5th
6th
7th
8th
9th
P1
P2
P3
A1
A2
A3
A4
A5
A6
A7
A8
A9
A10
A11
A12
A13
A14
A15
A16
A17
A18
A19
A20
A21
A22
A23
A24
A25
A26
A27
A28
-π
π
150
0
(Å)
M-band proteins
cMyBP-C
Crown 1
Crown 2
Crown 3
Titin alpha
Titin beta
Titin domain map
Ig-like
FN3-like
cMyBP-C stripes

Figure 2 Arrangement of myosin heads, cMyBP-C and titin from the M-band to the C-zone.

a, *Cryo-ET map of the thick filament, spanning from the M4' line to the C-zone.* ***b,*** *Cryo-ET map of the thick filament. with myosin tails removed for visual clarity.* ***c,*** *"Unrolled" depiction of the filament, revealing the spatial organization of the myosin heads. Position and arrangement of myosin heads from the P-zone (crowns P1, P2, and P3) to the 9th stripe of cMyBP-C (from crown A1 to A28).* ***d,*** *The complete crowns' nomenclature is indicated in.* ***e,*** *Side view of the "unrolled" filament having the center of the thick filament to the right side.* ***f,*** *"Unrolled" depiction of the filament, revealing the spatial organization of the six titin and 27 cMyBP-C molecules.* ***g,*** *Atomic models of the two titin chains and the 9 cMyBP-C within a single asymmetric unit.* ***h,*** *Domain map of titin. The pseudo-helical symmetry in the C-zone is dictated by titin's SRs, indexing the crowns in a repeated sequence of three types (crown 1, 2, and 3).* ***i,*** *The structural arrangement reveals the 9 stripes of cMyBP-C CTD, anchored on the thick filament in proximity to the interphase of different C-type SRs.*

3.3.2 Structural organization of myosin, cMyBP-C and titin

The segments containing the cMyBP-C stripes from 4 to 9 and the titin C-type super-repeats 3-8 have similar structures and were therefore averaged yielding an improved resolution of 18 Å (Fig. 3a, Extended Data Fig. 2h, Methods). We then fitted atomic models of thick filament proteins (obtained either from experimental structures or AlphaFold2 predictions (Alamo, Ware, et al. 2017; Jumper et al. 2021)) in the resulting reconstruction, allowing us to assign all densities to the corresponding thick filament components (Fig 3b, Supplementary Video 2).

The reconstruction revealed three distinct crown arrangements of myosin (defined as crowns 1, 2 and 3 from M-band to Z-disc direction) that form the outermost layer of the thick filament (Fig. 3d-i). Their double heads interact with each other within myosin dimers in the so-called interacting heads motif (IHM) (Woodhead et al. 2005). In this OFF state, one of the heads is folded back ("blocked head") so that its actin-binding site is blocked by the other head ("free head"). This configuration has been suggested to correlate with the super-relaxed state (Hooijman, Stewart, and Cooke 2011; S. Yang et al. 2020), where both motors have a highly inhibited ATPase activity (Woodhead et al. 2005).

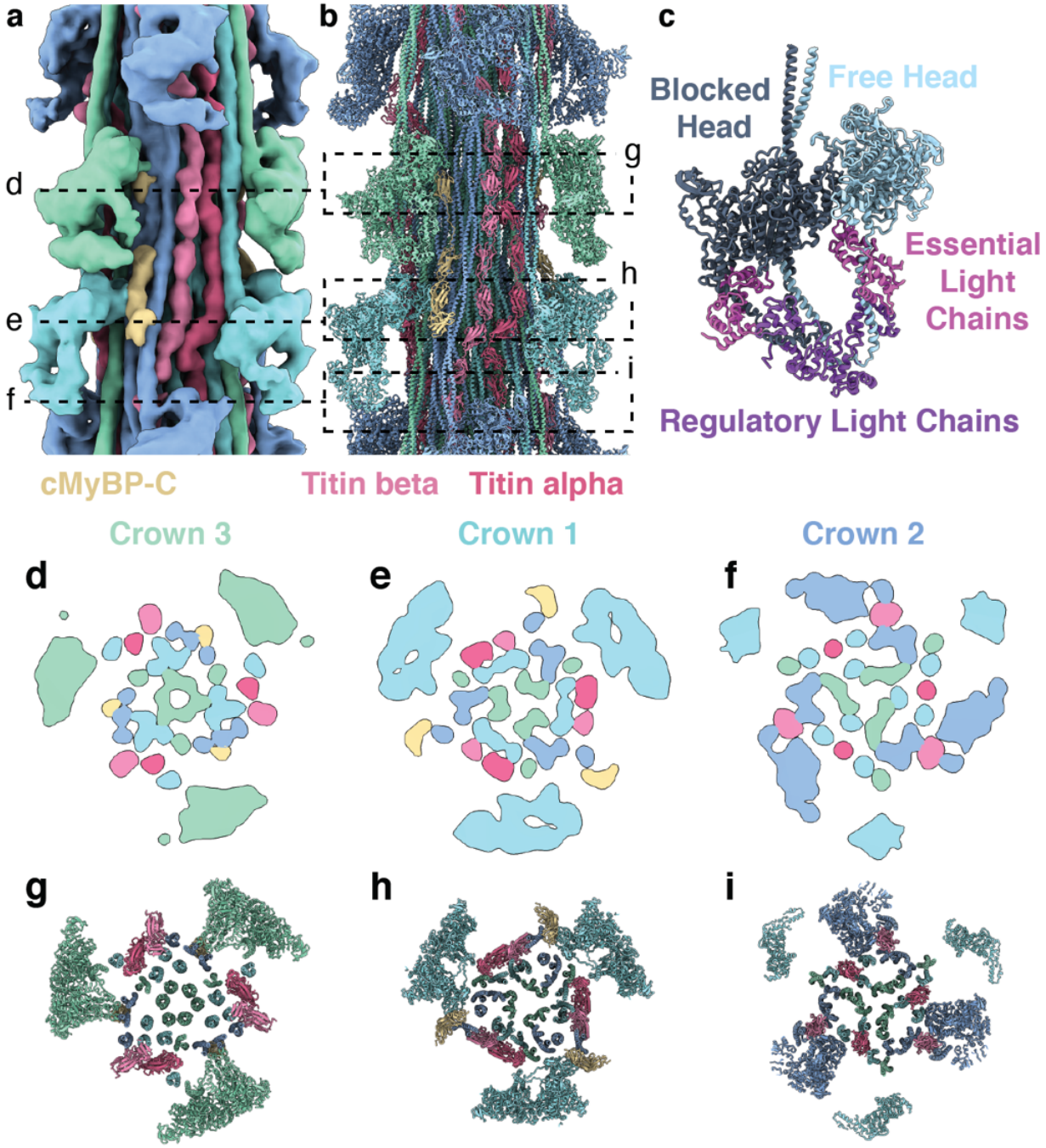

Figure 3 Structural model of the C-zone.

a,b, *The 3D reconstruction (**a**) and atomic model (**b**) of the C-zone, from cMyBP-C stripe #4 to stripe #9. The volume was colored according to its atomic model (**b**). **c**, Model of the myosin double heads in the IHM, with BH and FH binding to each other. **d-i,** Cross-sections of the map (**d-f**) and model (**g-i**) are shown at the level of the 3 different crowns, providing a more detailed view of the arrangement within the core of the thick filament.*

The myosin tails associated with the crowns form a large bundle of coiled-coils at the center of the filament (Fig. 3d-i). Interestingly, in the C-zone, besides interacting with each other, the myosin heads only bind to their own tail and are not in direct contact with the tails of other heads. Thus, there seems to be no direct communication possible between them.

On the bundle of tails, there are three pairs of titin molecules that run parallel to each other but where each molecule (or chain) has a unique conformation. To uniquely identify the two chains, we named them titin alpha and titin beta (Fig. 3a,b). While the heads of crown 1 and 3 do not interact with titin, the free head of crown 2 binds to the 6th domain of the titin C-type super-repeat (Fig. 3,f,i), as it can also be observed at cMyBP-C stripe 1 (Extended Data Fig. 5g-i).

Importantly, the structure also demonstrates that cMyBP-C binds with its domains C7 to C10 to an array of myosin tails (Fig. 4,f-h, Extended Data Fig 6a), thus providing visual confirmation to biochemical evidence that started accumulating half a century ago (Bennett et al. 1986; Offer, Moos, and Starr 1973; Starr and Offer 1978).

Unexpectedly, the C-terminal region of cMyBP-C also directly interacts with the IHMs. Specifically, domain C10 binds to the free head of crown 3 while domain C8 forms broad electrostatic interactions with the free head of crown 1 (Fig. 4g,h - Extended Data Fig. 5c,e). The atomic model (see Methods) indicates that this interaction likely involves loop 4 and the cardiomyopathy loop of myosin (Fig. 3b,4g, Extended Data Fig. 5c). These unforeseen interactions of the cMyBP-C with myosin motors suggest a previously undescribed direct role in the stabilization of the myosin OFF state in the C-zone and explains why cMyBP-C can stabilize the super-relaxed state(McNamara et al. 2016). This highlights a paradigm-shift for the role of cMyBP-C in sarcomere regulation and presents an interface at which unexplored pharmaceutical intervention into hypertrophic cardiomyopathy patients can be explored.

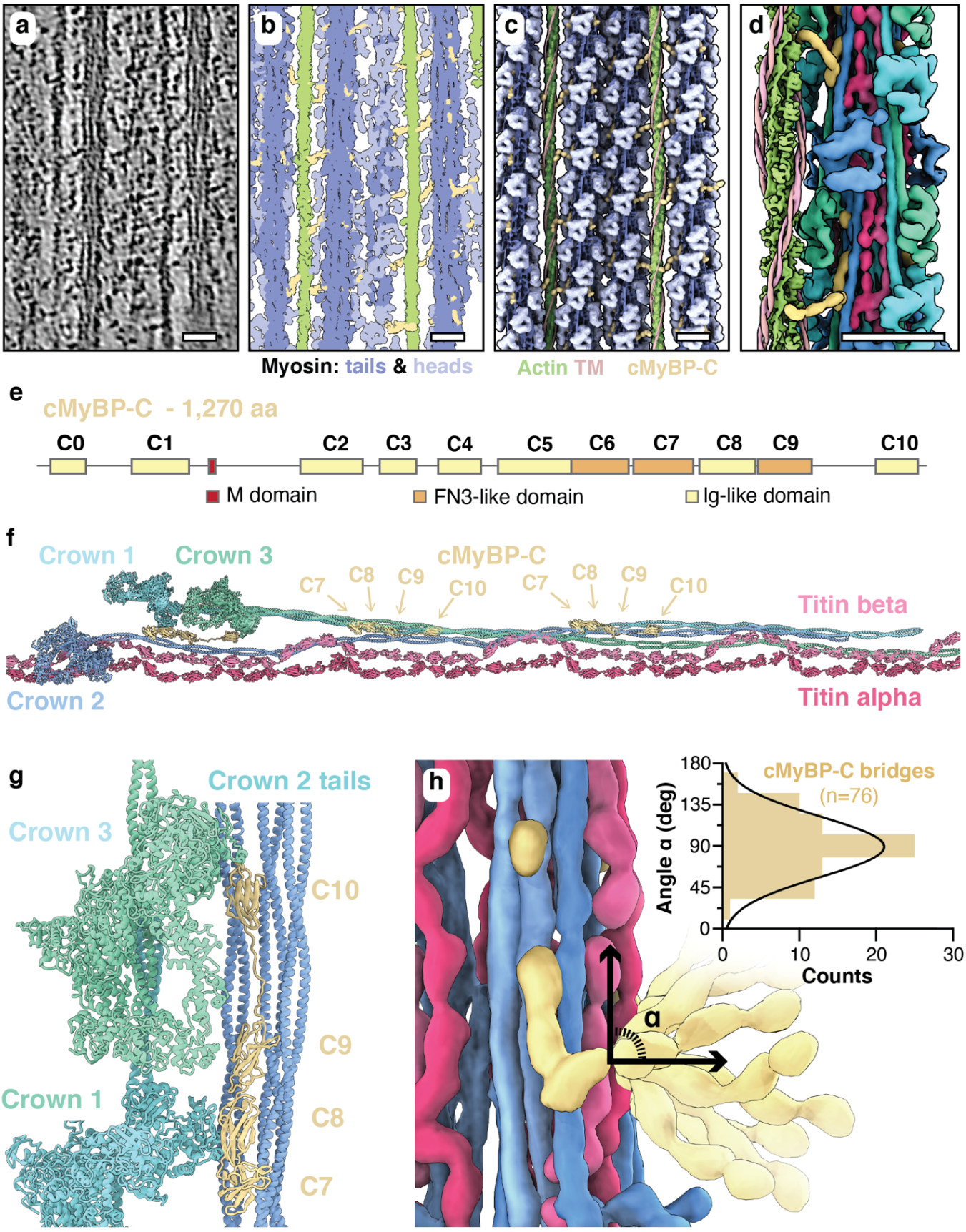
a
b
c
d
Myosin: tails & heads
Actin TM
cMyBP-C
e
cMyBP-C - 1,270 aa
C0
C1
C2
C3
C4
C5
C6
C7
C8
C9
C10
M domain
FN3-like domain
Ig-like domain
f
Crown 1
Crown 3
cMyBP-C
C7
C8
C9
C10
C7
C8
C9
C10
Titin beta
Crown 2
Titin alpha
g
Crown 2 tails
Crown 3
C10
C9
Crown 1
C8
C7
h
180
135
90
45
0
Angle α (deg)
cMyBP-C bridges
(n=76)
0
10
20
30
Counts
α

Figure 4 cMyBP-C forms links between the thick and thin filaments.

***a**, Tomographic slice (0.94 nm thickness) of the C-zone in the relaxed state. **b**, Tomogram segmentation of a 9.4 nm slab from the same region as in (**a**), depicting the thin filament (light green), the thick filament core (blue), the myosin heads (light blue), and cMyBP-C (yellow). **c**, A 3D model of the sarcomere organization in the same slab as in (**b**), showing the flexible cMyBP-C links, spanning 3 to 4 globular domains, linking thick and thin filaments. **d**, Close-up view of the connection of two consecutive cMyBP-C to the same thin filament. **e**, Domain map of cMyBP-C. The C-terminal domains from C7 to C10 bind to the thick filament, the central domains C3 to C6 form the link, and the N-terminal domains bind to the thin filament. **f**, Structural model of the CTD of cMyBP-C, depicting how it binds to the thick filament core by multiple interactions with crown 2 tails. **g**, Schematic representation of the cMyBP-C bridging region. Flexibility is shown together with a plot of the angular distribution of the bridge measured in the tomographic volumes. Scale bars, 20 nm.*

3.3.3 Myosin tails exhibit distinct arrangements and pattern of interactions

Although the organization of myosin tails has been determined in insects and spiders (Alamo et al. 2008; Daneshparvar et al. 2020; Hu et al. 2016), to date we have no structural information to elucidate their organization in mammalian striated muscle, representing an unbridgeable gap in our understanding of the molecular mechanics of cardiac contraction. In the 43 nm repeat reconstruction of the C-zone, only parts of the tails are visible, so to visualize them in their full extent we calculated a 200 nm long helical extension starting from this reconstruction (see Methods). The resulting 3D map allowed us to elucidate the tail arrangement associated with each of the three crowns (Figure 5a). The tails of the three crowns interweave, interacting with each other and form a compact rod. The tails of crown 3 form the core of the rod and interact with each other in their C-terminal section, where the conserved 29-residue assembly competence domain is localized (Sohn et al. 1997). This domain plays a crucial role in thick filament assembly, suggesting that the myosin tails that are associated with crown 3 represent the nucleus for this process (Thompson et al. 2012).

To quantify and compare the curved nature of the tails we calculated a sinusoidal compression percentage (see Methods) that positively correlates to increases in tail curvature and resulted in 3.05%, 4.44%, and 2.53%, for tails from crowns 1, 2 and 3, respectively. Notably, while the tails bear a unique inflection point at different locations, crown 1 and 2 share a strongly pronounced kink at the phenylalanine residue in position 1449 (Fig. 5a) that does not correspond to any skip residues predicted in the coiled-coils sequence and is not present in non-mammalian myosin II (Rahmani et al. 2021), possibly revealing a peculiar characteristic of the mammalian myosin-II tail.

Within the C-zone, the myosin tails have different degrees of interaction with titin. The tails associated with crown 3 have only minimal interaction while those of crown 1 bind to either titin

alpha, titin beta, or both for its entire length (Extended Data Fig. 7b,d). Tails associated with crown 2 only bind to titin beta and mostly through their S2 domain (Extended Data Fig. 7c). Taken together, these data show that each crown within the cardiac thick filament exhibits a distinct arrangement of its tails and pattern of their interactions that are likely orchestrated and tuned by the titin chains, although the reverse process would also be conceivable. This suggests the existence of specialized roles for the myosins of each crown in length-dependent activation and contraction. The curved nature of the tails of crown 1 and 2 and their direct interaction with titin supports the observation that both titin chains not only act as counters of myosin molecules (as a molecular ruler), but can sense and relay muscle load, transducing a signal that might promote transition from super-relaxed to the disordered-relaxed state of the upstream crowns towards the M-band.

3.3.4 Variability of myosin crowns in the P- and C-zones

To better understand whether there are differences between myosin heads along the filament, we analyzed our combined reconstruction, where we resolved 93 myosin double heads, spanning from the P-zone layers (P1, P2, and P3) to the C-zone (from A1 to A28) (Fig. 2,a,e). We observed that all myosin heads are in the IHM state, confirming that all 31 layers are in the OFF state. The pseudo-helical arrangement of "crown 1, 2, 3" pattern, which we observed from cMyBP-C stripe 4 to 9 is preserved throughout the C-zone. However, in the regions closer to the M-band there are noticeable structural differences (Fig. 2,a,e, Extended Data Fig. 8,b-d).

To quantify these variations, we calculated the orientations (Euler angles), the azimuthal angle, axial positioning, and the radial distance for each crown (Extended Data Fig. 8,b-d). The heterogeneity in rise, twist, and angular orientation of myosin is particularly pronounced from crowns P1 to A9 while a more regular pattern emerges from A10 (Extended Data Fig. 8,b). This is exemplified by crowns A5 and A8: although they localize in canonical "crown 2" layers, these crowns have a much wider radial distance that makes them the closest to the thin filaments after P1 (Extended Data Fig. 3d). Moreover, their free heads are projected further outwards (Fig. 5a-e), as documented by their strongly negative beta angle (Extended Data Fig. 3d). This variability suggests that these crowns might have unique capacities in terms of strain susceptibility and activation rate. In particular, as they are solely stabilized by a weak interaction with titin, crown 2 appears likely to be the first responder in length-dependent activation, with exceptional layers such A5 and A8 being the most representative cases.

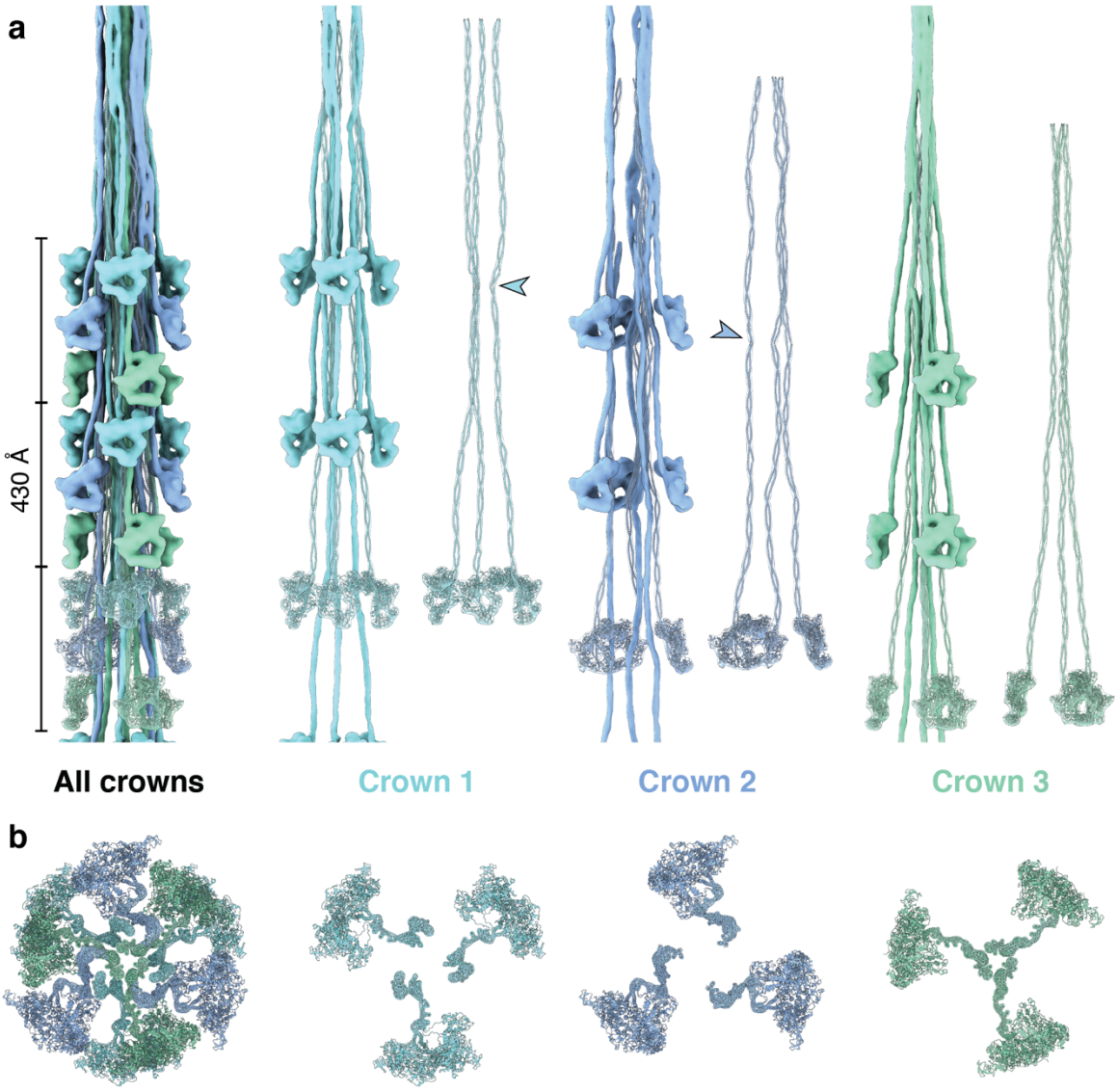

Figure 5 The spatial arrangement of myosin within the C-zone of the thick filament.

***a-b**, Side (**a**) and top (**b**) views of a combined map and atomic models of a section of the thick filament only depicting myosins. The myosins follow a 3-fold rotational symmetry and a pseudo-helical symmetry with a 43 nm rise and 0˚ twist. The asymmetric unit comprises three myosin crowns, each composed of three myosin double heads. The tails form the backbone of the thick filament. The tails of crown 2 represent the outermost layer, followed by those of crown 1 and crown 3. While the tails of crown 3 run relatively straight, the crown 1 and crown 2 tails exhibit a certain degree of undulation. The arrows indicate an inflection point, common to crown 1 and crown 2 tails at phenylalanine 1449.*

Taken together, although all myosins in our reconstruction are in the IHM state, their stabilization varies and relies on a variety of interactions, depending on their specific molecular context, that involves binding sites on myosin S2, titin, and cMyBP-C (see also below). The vast majority of these interactions seem reliant on the flexible loops in the free head: loop 4 and cardiomyopathy loop. Conceivably, this organization along the filament is indicative of an ability for the myosin heads within the thick filament to be fine-tuned by regulatory mechanisms of muscle contraction within the thick filament in adaptation to specific physiological conditions (Irving 2017).

3.3.5 Titin organization in the P- and C-zone

Despite its essential role in sarcomere assembly and function, the detailed structural arrangement of titin has remained hitherto unknown (Gautel 2011; Gautel and Djinović-Carugo 2016). We used our combined reconstruction, spanning from the P-zone layers (P1, P2, and P3) to the C-zone (from A1 to A28) to build an atomic model of titin in which we could assign all the density to the corresponding titin domains. This allowed us for the first time to describe the molecular organization of titin from the C-zone (specifically from C-type super-repeat 2) to the M-band (Fig. 5b,e-h, Extended Data Fig. 7a) and reveal its interplay with the other thick filament components. Importantly, no structural model for titin organisation in the thick filament has been previously determined, representing a distinct lack of molecular information of fundamental importance to understanding both sarcomere function and effects causative of disease.

Surprisingly, while the three titin alpha chains run along the entire length of the thick filament and reach to the P-zone of the opposite half-sarcomere, titin beta is interrupted abruptly at myosin crown A1 (Fig. 2b,e-h). Thus, there are six chains in the C-zone, but only three in the P-zone. Consequently, only three chains enter the M-band from each side of the thick filament, resulting in only six chains of titin in the M-band instead of twelve.

In the C-type super-repeats, titin alpha and beta run alongside each other with only sparse and presumably weak interactions, resulting from the molecular contacts of titin with myosin tails. In both the P- and C-zone, titin chains show a spring-like arrangement, with recurring curved indentations following a 3-4-4 pattern that matches the alternating Fn3 and Ig-like sequences found in titin's super-repeats (Henk L. Granzier and Labeit 2004; Labeit et al. 1992) (Extended Data Fig. 6a-d). Beside this common motif, we observed a certain degree of variability between different C-type super-repeats (Fig. 2b,e-h). These variations are mostly accounted for by the disorganized linkers scattered between

domains all along the structure and are more pronounced on titin beta. The super-repeat domains from 4 to 8 are those showing the highest conformational variability in titin beta. These domains interact with the S2 domain of crown 2 (Extended Data Fig. 5b,g-j) and their variability is reflected in the heterogeneous configuration of crown 2 IHMs (Extended Data Fig. 8b-d) as already discussed.

Missense mutations in the A-band portion of titin which includes the C-zone have been linked to multiple, often severe myopathies and cardiomyopathies (Palmio et al. 2019; Rees et al. 2021). A hotspot for variants linked to hereditary myopathy with early respiratory failure (HMERF) is A150/Fn3-119 (Palmio et al. 2019). The proximal S2 domain of crown A5 sits on this domain, suggesting that a functional impairment of this unique crown might result in this specific muscle disease (Figure 2, Extended Data Fig. 5g-j).

In the P-zone, which is the transition zone between the A- and M-band, the pattern of the titin C-type super-repeat is replaced by 7 domains (from A164 to A170) that lead to the titin kinase (TK) domain (Fig. 2b,e-h). Following the titin alpha chain in our reconstruction, we identified a bulkier region behind the P1 crown that fits the size, the shape, but not the expected position of the TK (Extended Data Fig. 9b). TK interacts with myosin's S2 domain, and is closely connected via its C-terminal regulatory tail to the adjacent m1 domain, as has been previously proposed (Bogomolovas et al. 2021; Puchner et al. 2008). Interestingly, the titin m1 domains interact with the S2 domains of the myosins in crown P2, while the subsequent titin m2 and m3 domains are wrapped around the myosin tails associated with the P1 crown (Extended Data Fig. 9b).

In the C-zone, the titin beta chain follows the same register of titin alpha, however, after domain A154, in proximity of crown A2, its organization changes to a bowtie-shaped structure and its chain is absent after crown A1 (Extended Data Fig. 9d). On top of the A1 crown, we identified another bulky density reminiscent of the TK-m1 configuration. However, the limited resolution does not allow a clear identification of domains. We propose that the bowtie-shaped structure might correspond to 13 titin domains (from A158 to A170), connecting the rest of titin beta to the beta TK-m1 domain (Extended Data Fig. 9d) and that titin beta terminates its run along the thick filament on the A1 motor domains, perhaps after proteolytic cleavage by calpain 3 (CAPN3) downstream of titin m1 (Charton et al. 2015). Thus, the TK domains of titin alpha and possibly of titin beta would localize at 77 and 105 nm from the centre of the M-band (in contact with crowns P1 and A1, respectively) interacting with their S1 and S2 domains in privileged positions that could couple myosin head activation to mechano-sensing by TK.

3.3.6 The molecular organization of the cardiac M-band

The M-band, comprising 6 transverse "lines" (M1-M6), is a complex network of structural proteins, metabolic enzymes and proteostatic machinery components (Gautel and Djinović-Carugo 2016; Lange et al. 2020). Proteins in this network are reported to anchor the M-region to the sarcolemma, stabilize the myosin filament hexagonal lattice, and to serve as a signaling scaffold that integrates mechanical forces, energy balance and protein turnover (Gautel and Djinović-Carugo 2016; Lange et al. 2020). Our reconstruction of the thick-filament M-region shows a twofold mirror axis centered around the M1 line, perpendicular to a threefold rotational axis. We could clearly identify the myosin crowns in the P-zone and also follow the tails from the innermost 4 crown, that run antiparallel to each other, thus confirming previous indications(Al-Khayat et al. 2010) that the P1 tails terminate in proximity of the P1 crown from the opposite polarity (P1') (Fig. 6a,c).

In addition to myosin, we observed several densities protruding from the core of the tails, reflecting M-band-specific proteins such as myomesin 1 and 2 (Lange et al. 2020), obscurin-like-1 (OBSL1(Fukuzawa et al. 2008)) titin C-terminal domains (W. M. J. Obermann et al. 1997) and accessory proteins like muscle type creatine kinase (M-CK). We identified a density spanning from M-lines M1 to M4 that binds to the thick filament core at 85 Å and 230 Å from M1 and projects outward with a threefold symmetry into the hexagonal lattice. Taking into consideration its localization, arrangement and composition from ~4 nm-long domains, we suggest this density to represent a complex of myomesin-1, OBSL1 and possibly myomesin-2 (Fig. 6a-c). Surprisingly, in our super-relaxed cardiac M-band reconstruction, we observe densities at 118 Å from the M1, protruding towards neighbour thick filaments in the lattice (Fig. 6c). However, the expected cross-connecting M-bridges, as they would be inferred from the dimeric myomesin-1 structure (Lange et al. 2005), are averaged out during the refinement due to their flexibility.

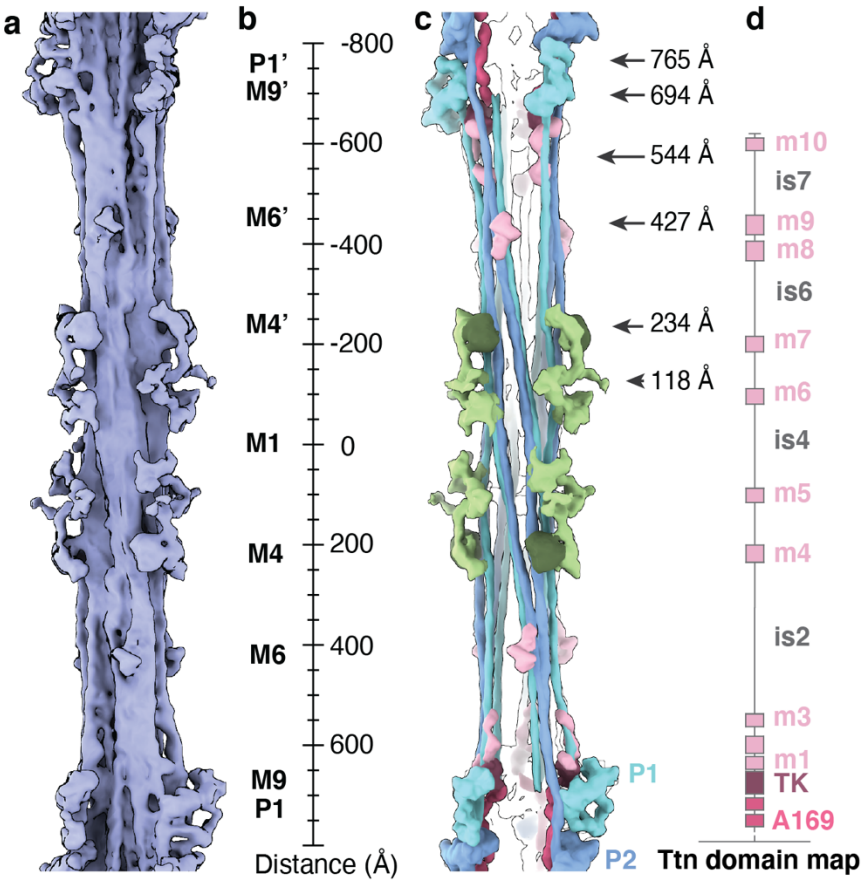

Figure 6 The layout of the M-band.

***a**, Density of the thick filament in the M-band region. The overall structure shows a twofold rotational axis perpendicular to a threefold rotational axis (D3 symmetry). **b,** Ruler, providing markers for the expected high-density M-lines in the cardiac sarcomere (M1, M4, M6, M9). M1 is absent in our reconstruction, likely due to the lattice organization being averaged out during the refinement process. **c,** Most clearly identifiable densities protruding from the core of the myosin tails. **d**, Domain map of the titin C-terminal region, which consists of the titin kinase domain (TK), the ten m-domains (m1-10), and seven interspacing regions (is1-7).*

We could not determine the location of obscurin. This is likely due to a combination of structural flexibility and the localization of obscurin at the myofibril periphery, as opposed to the central sarcomeric localization of OBSL1 (Fukuzawa et al. 2008). As described above, only titin alpha reaches the M-band region with its C-terminus. It consists of the TK domain, ten m-domains (m1-10), and seven interspacing regions (is1-7) (W. M. Obermann et al. 1996). Within each asymmetrical unit of the bare zone, at 427 Å from the high-density M-line M1, we observed a density that fits the size and shape of two Ig-like domains, possibly the adjacent m8 and m9 titin domains. In addition, there are other small densities that might correspond to m1, m2, m3 and m10. The interspacing regions are very thin and likely contain few secondary structure elements, and therefore cannot be seen in our reconstruction. In line with previous suggestions (W. M. Obermann et al. 1996), these

observations support that the titin alpha M-region spans across the M-band. The identification of M-line densities in their near-native state provides a blueprint for titin m-domain localization and structural rationalization of reported biochemical interactions (Fukuzawa et al. 2008; Hornemann et al. 2003; Lange et al. 2020; W. M. J. Obermann et al. 1997; Pernigo et al. 2017; 2010). Detailed assignment of the densities will require a combination of site-directed labeling of the domains and cryo-ET in the future.

Nonetheless, the structure of the native cardiac M-band presented here *in situ* represents an initial model of the M-band at the molecular scale. The crosslinks formed by M-band proteins are dictated by the threefold rotational symmetry of the thick filament. However, the interactions of titin with OBSL1, and OBSL1 with myomesin-1 are all in a 1:1 complex (Pernigo et al. 2017; 2010), posing a symmetry mismatch between these constituents and the previously expected six titins from each half-sarcomere entering the M-band. Our analysis resolved this paradox, showing that the full M-band region of titin is only present in three copies in each half-sarcomere, directing the assembly of the six observable M-links (three in each half-sarcomere).

3.3.7 cMyBP-C forms links between thick and thin filament

In our reconstruction of the thick filament, we identified that the C7-C10 domains of cMyBP-C bind to an array of three consecutive tails associated with crown 2 in 9 regions of the C-zone (Fig. 2a-b,f-g,i) (Luther et al. 2011; Tonino et al. 2019). C7-C10 run longitudinally along the filament: for each cMyBP-C, C10 is in the M-band direction and C7 is oriented toward the Z-disc, spanning a 16 nm region at the interphase between titin C-type super-repeats (Fig. 2f-i). Initial biochemical data suggested that the confinement of cMyBP-C to the C-zone might depend on a direct interaction between the C7-C10 of cMyBP-C and the titin C-type super-repeats (Freiburg and Gautel 1996). We do not observe any direct interactions between the two proteins in the relaxed state. Instead, we clarified that the C-terminal domains bind to a specific configuration of myosin tails that emerges in the C-zone as a complex interplay between myosin tails and titin C-type super-repeats (Fig. 4f,g, Extended Data Fig. 5b-d). Specifically, C7-C10 bind to regions that emerge from an array of tails associated with crown 2 belonging to three consecutive C-zones (Fig. 4f,g) via strong electrostatic interactions (Extended Data Fig. 5d,f). This configuration also resolves the mysterious absence of cMyBP-C in the titin region of titin super-repeat 1, as the site where cMyBP-C would bind is in this case composed of tails of the D-type super-repeat 6, which we have not resolved in our structure, but which have likely a different conformation.

In the cMyBP-C C-terminal region, C7 is the last clearly resolved domain and appears to act as a pivot point for the remaining domains that reach away from the thick filament (Fig. 3a). The bridging region of the protein indeed showed great flexibility and only had weak densities (Fig. 4h - Extended Data Fig. 10a,b). Although stripes 1, 2 showed biases towards a specific lattice organization the cross-sections analysis at the different stripes revealed that the MyBP-C N-terminal region can bind to either of the two neighbouring thin filaments (Extended Data Fig. 10a,b,c). Remarkably, cMyBP-C stripe 2 shows some unique features (Extended Data Fig. 11): the FH of crown A7 is not stabilized by an interaction with cMyBP-C C8, as it is observed in all the other stripes, instead its IHM is stabilized by interaction with myosin light chains of the neighbour crowns.

To validate this pliability of cMyBP-C links, we back-plotted the structures into the reconstructions of the tomographic volume and manually traced the flexible globular domains connecting thick and thin filaments (see Methods) (Fig. 4a-d, Supplementary Video 3). We observed the presence of several cMyBP-C links in the C-zone, suggesting that the N-terminal region can indeed interact with the thin filament. Despite our efforts, subtomogram averaging did not resolve any clear arrangement of the N-terminal region on the thin filament, indicating a high heterogeneity in these interactions, in agreement with previous reconstructions from isolated components (Risi et al. 2022). Our segmentation exposed the presence of a tether formed by 3 to 4 domains that blend in the signal of the thin filament with high degrees of flexibility (Fig. 3h). Of note, the thin filament with bound N-terminal cMyBP-C domains appears in the OFF-state, suggesting that cMyBP-C, at physiological phosphorylation levels, and in the absence of myosin cross-bridges, is not a thin filament activator.

cMyBP-C represents a crucial site of cardiomyopathies and has thus far remained an enigmatic component of the sarcomere, with its function in modulating myosin activation being both proposed but not well understood. Collectively, our analysis of cMyBP-C suggests multiple roles in sarcomeric mechano-signaling. On the one hand, it is reasonable to speculate that under thick filament strain, the sinusoidal path of crown 2 tails can experience a minimal but significant stretch, resulting in the alteration of the binding sites for the cMyBP-C C-terminal region and perturbing its interactions with the FHs. As such, the interactions of the C-terminal domains with the IHMs of crown 3 and 1 would represent a transducer for tension and stretch, independently of thin filament positioning. On the other hand, the crosslinks to the thin filament can sense the stretch on and sliding of the thin filament and relay the tension to both the C-terminal and N-terminal domains of cMyBP-C, while domain C1 and

C0 might extend further to bind the myosin light chains on the thick filament surface, either in cis or trans.

3.4 Conclusions

Our study provides important insights concerning the fundamental organization and regulation of cardiac thick filaments in vertebrates. Our cryo-ET structure of the sarcomere in the relaxed state together with our previously determined structures of the sarcomere in the rigor state (Wang et al. 2022; 2021), provide fundamental insights into muscle architecture, its molecular complexity, intricacy of regulation and sophistication. The structure of the native thick filament provides a three-dimensional representation of how the myosin heads and tails, myosin-binding protein C, and titin are organized in different areas of the filament, explaining how these components can interact during muscle contraction. It also reveals distinct differences in how certain domains of the sarcomere are organized when compared to tradition reconstituted approaches and classical EM methods.

Our analysis revealed a plethora of conformations and stabilization mechanisms for the IHM, which are region-dependent and rely on various interactions with titin m1 domain, cMyBP-C C-terminal region, titin SRs, other myosin tails, and myosin light chains. These findings support a model of a thick filament that is capable of sensing, integrating, and modulating responses to numerous signals such as beta-adrenergic-dependent phosphorylation, Ca^{2+} concentration, length, and mechanical load. In addition, we revealed the organization of titin along the thick filament and the genuine position of its TK domain not in the M-band but juxtaposed at the interface between the M-band and A-band. Such a localization indicates that the role of TK in regulating the sarcomere may be more tightly coupled to the state of the myosin heads than previously thought.

The six titin chains probably influence the arrangement and pattern of interactions of each myosin tails. Thus, it is understandable how titin acts as a scaffold and a molecular ruler for myosin assembly during sarcomerogenesis, as has been previously suggested (Tskhovrebova and Trinick 2003). This is an interesting reflection of the protein nebulin found in the thin filament (Wang et al. 2022). Furthermore, the close interaction and spring-like appearance of both titin and the myosin tails and their connection to myosin heads make a compelling case for a load-dependent activation mechanism of the thick filament promoting the transition from the super-relaxed to the disordered relaxed state.

We were able to observe biologically significant structural variability along the thick filament, which is a crucial aspect needed for understanding sarcomere function and regulation. Static structures in isolation tell us little about the interplay and dynamics of multiple, highly regulated myosin heads interlinked to one another. These important details would have been lost with most structural biology methods and demonstrate the merits of cryo-ET in visualizing this variability in the native state. The MyBP-C links connecting thin and thick filaments are another example of the unique power of cryo-ET. Finally, the insights gleaned through our thick filament structures lay a framework for understanding muscle development, function, and muscle disorders.

3.4 Materials and Methods

3.4.1 Myofibrils preparation and vitrification

Demembranised left-ventricular mouse myofibrils were prepared as previously described(Wang et al. 2022). The myofibrils were collected by centrifugation at 3000 g for 2 minutes at 4°C, followed by two washes with pre-relaxing buffer (100 mM TES pH 7.1, 70 mM KCl, 10 mM reduced gluthatione, 7 mM $MgCl_2$, 25 mM EGTA, 20 µM mavacamten, 5% dextran T500). To prepare for plunging, the pre-relaxing buffer was replaced with final relaxing buffer (pre-relaxing buffer plus 5.5 mM ATP). The relaxed myofibrils were then frozen onto Quantifoil Au R2/2 SiO_2 200 mesh grids using a Vitrobot (Thermo Fisher). The myofibril suspension was incubated on grid at 25°C and 100% humidity for 30 seconds, blotted for 30 seconds from the opposite side of the carbon layer, and plunged into a liquid ethane-propane mixture.

3.4.2 Cryo-FIB milling and electron cryo-tomography (cryo-ET)

The preparation of lamellae for cryo-ET data acquisition was performed by cryo-FIB milling using an Aquilos 2 cryo-FIB/SEM with a cryo-shield, according to previously described protocols (Tacke et al. 2021; Wang et al. 2022; 2021) aiming for lamellae with a final thickness of 180 nm (range from 90 to 250 nm). The data acquisition was carried out with a Titan Krios transmission electron microscope (Thermo Fisher), fitted with a K3 camera and an energy filter (Gatan). The acquisition of overview images of myofibrils in the lamellae was done at a nominal magnification of 6,700× to identify the C-zones regions. The average sarcomere length was 2.33 µm (S.D. = 0.16 µm, N = 29).

The tilt series were acquired targeting the C-zones at 81,000× nominal magnification. The pixel size was calibrated to 1.146 Å using the 143.3 Å peak in the fast Fourier transform of the final thick filament reconstruction (from M-band to C-zone) (Extended Data Fig. 4a,c). A dose-symmetric tilting scheme (Hagen, Wan, and Briggs 2017) was applied during acquisition with a tilt range of −50° to 50° relative to the lamella plane at 2.5° increments. The sample was subjected to a total dose of 120 to 160 $e^{-}/Å^2$. Tilt series were acquired between −3 and −6 µm defocus. All images and a total of 89 tomograms were acquired using SerialEM (Mastronarde 2003).

3.4.3 Tomogram reconstruction and particles picking

Motion correction and contrast transfer contrast (CTF) estimation was performed in Warp (Tegunov and Cramer 2019), tilt series alignment was performed in IMOD (Kremer, Mastronarde, and McIntosh 1996). Final tomogram reconstruction and subtomograms extraction was performed in Warp. After binning the tomogram to a pixel size of 0.92 nm and low-pass filtering them at 60 Å, we used crYOLO (Wagner et al. 2019) to pick and trace both the thick and the thin filaments (Extended Data Fig.1).

3.4.4 Thin filament processing pipeline, model building, and visualization

The traced thin filaments were re-sampled with an inter-segments distance of 18 Å, leading to the extraction of 365,971 subtomograms with a box size of 293.5 Å (128 pixels, binning 2). Each subtomograms was rotated to orientate the thin filaments parallel to the XY plane using the prior angles from the tracing. Then its central slab of 100 slices was projected and used as an input for two-dimensional classification(Moriya et al. 2017; Schöenfeld et al. 2022; Z. Yang et al. 2012). The classes that did not show a clear presence of thin filaments were discarded and the remaining segments were processed in RELION 3.1 (Bharat and Scheres 2016; He and Scheres 2017). The initial helical reconstruction of led to 14.3 Å resolution map (0.143 FSC criterion) with 27.4 Å rise and -167.2° twist (Extended Data Fig.1). After removing the duplicated particles using a customized script, 100,447 subtomograms were further refined with two different masks that either covered the entire density of the thin filament, or only included the F-actin density. The full thin filament (F-actin and tropomyosin) was refined with helical reconstruction and reached a resolution of 8.2 Å while the refinement of F-actin alone resulted in an 8.3 Å resolution map. The two maps were aligned in ChimeraX (Pettersen et al. 2021) and the individual chains from the PDB model 6KN7 (Yamada, Namba, and Fujii 2020) were placed in the density with rigid body fitting. The model of tropomyosin's coiled-coils was improved with Namdinator, using automatic molecular dynamic flexible fitting (MDFF) (Kidmose et al. 2019). The final composite map (Extended Data Fig.3a) was created by combining F-actin from the F-actin alone reconstruction and tropomyosin from the full thin filament reconstruction using "color zone" and "splitbyzone" functions in ChimeraX.

3.4.5 Thick filament processing pipeline

The traced thick filaments were re-sampled with an inter-segments distance of 130 Å, leading to the extraction of 67,492 subtomograms with a box size of 1280 Å (160 pixels, pixel size 8 Å). 2D classification was performed similarly to the thin filament processing, using a central slab of 400 Å, resulting in 37,118 high-quality subtomograms. 3D classification with refinement and helical reconstruction (430 Å, 0° twist) resolved 4 classes that showed different orientation of crown 2. Class A showed a "projected" IHM, class B had a mixture of conformations resulting in fuzzy density for crown 2 IHM, and class C showed a "retracted" IHM (Extended Data Fig.1b). The refined coordinates were used to individually re-extract the 3 classes from Warp, using a box-size of 144 pixels and a pixel size of 4 Å. The individual classes were refined with RELION and their coordinates were mapped back into the tomograms using ArtiaX (Ermel, Arghittu, and Frangakis 2022). Class A, which was later resolved as the segment from crown A8 to A12 (cMyBP-C stripe #2) (Extended Data Fig.1g), showed a unique distribution within the sarcomere. This was used as the initial anchor point to obtain the 3D coordinates of the particles located at an axial distance of -43 nm and +43 nm (Extended Data Fig.1f,h). Through an iterative process of 3D refinement, multi-reference 3D classification, particles back-projection, and axial shift calculations, we resolved 8 structures of the thick filament, spanning from M-band to C-zone (Extended Data Fig.1). The resulting 3D maps showed high variability in resolution within different regions of the same map leading to over-sharpening of the more flexible regions, we therefore resorted to LocSpiral (Kaur et al. 2021) to improve map interpretability. All reconstructions showed a three-fold rotational axis and were therefore refined with a C3 symmetry. The M–band reconstruction further revealed two orthogonal two-fold rotational symmetry axes that intersect at the three-fold axis at an angle of 60 degrees and was later refined with a D3 symmetry.

To build the final composite map, the power spectra of the reconstructions were normalized with *relion_image_handler* (He and Scheres 2017) and a soft cylindrical mask of 15 px (~ 60 Å) was applied to all maps. The filtered reconstructions were aligned in ChimeraX (*fit in map*) and the final map was created by merging the densities of the different segment, using the maximum value at each voxel (*volume add*, *volume maximum* in ChimeraX). To obtain a continuous and homogeneous density that we could use to trace the myosin tails, we took our 18 Å reconstruction of the last 5 stripes of cMyBP-C and extrapolated a 200 nm long helix with *relion_image_handler* (430 Å, 0° twist) (He and Scheres 2017).

3.4.6 Thick filament's model building and visualization

The model of the thick filament was built using a combination of previously available models and AlphaFold2 predictions (Jumper et al. 2021). For the model of myosin-II's, we used the IHM of human beta cardiac heavy meromyosin (PDB entry 5TBY (Alamo, Ware, et al. 2017)) while the tails were predicted in AlphaFold2 using the amino acid sequence of *Mus musculus*'s MYH7 (5 segments of ~250 amino acids with ~20 amino acids overlap) . Similarly, the CTD of cMyBP-C was predicted in AlphaFold2 using the last 590 amino acids of *Mus musculus*'s MYBPC3. The region of titin from domain A101 to m3 (amino acids 24,760 – 32,350) was submitted for prediction as multiple entries (each ~950 amino acid) with overlapping terminal domains. The models were initially built in the map using rigid body fitting and their final organization was later adjusted with multiple rounds of MDFF in Namdinator (Kidmose et al. 2019), starting with 40 Å low-pass filtered densities and gradually using the higher-resolution maps. The models spanning from crown A18 to A28 were obtained by cloning the model spanning from crown A15 to A17. For the visualization in (Figure 2a), we resort to ChimeraX functions "*colorbyzone*", "*splitbyzone*", and "*Gaussian filter*" with standard deviation = 3. The depictions in (Figure 2c,e,f) were obtained using Chimera "*unroll*" function on the structure of all components individually.

3.4.7 Position and orientation of myosin's crowns

To describe the differences in the IHMs across our entire reconstruction, for each crown we calculated the cylindrical coordinate (azimuthal angle, radius, and z-axis height) and extracted radial distance, rise, and twist (Extended Data Figure 8d). Additionally, we calculated the Euler angle (alpha, beta, and gamma angles) to better describes their 3D arrangement (Extended Data Figure 8c). To do this, we treated each IHM as a triangle lying on the surface of a cylinder (the thick filament). The coordinates of the three vertices was obtained from the atomic coordinates for the alpha-carbons of three residues: chain A residue 180, chain B residue 180, and chain A residue 830 (Extended Data Figure 8a). Cylindrical coordinates are obtained from the triangle's centroid, while the Euler angels are relative to a reference triangle that lies on the lateral surface of the cylinder and has its top side parallel to the cylinder's plane and tangential to its radius.

3.4.8 Sinusoidal compression percentage

To quantify the curviness of the myosin tails, for each tail, we first obtained the atomic coordinates of the alpha-carbons for the two amino acids chains in the coiled-coils. We then traced a new three-dimensional curve running through the central points between each alpha-carbon couple. For each curve segment, we calculated the sinuosity S by the ratio of length of curve C to the Euclidean distance between the ends L:

$$S = \frac{C}{L}$$

The sinusoidal compression percentage (SCP) is then given by:

$$SCP = (S - 1) \cdot 100$$

3.4.9 Tomogram segmentation and cMyBP-C links

To described the 3D organization of the sarcomere components we selected two representative tomograms (Figure 1a, 4a, Supplementary Videos 1 and 2) and denoised them using cryo-CARE (Buchholz et al. 2019). With a customized script, we mapped back each subtomogram using a binary mask of their corresponding structure, matching the coordinates and orientations obtained from the 3D refinement. The resulting binary MRC files were imported in Dragonfly (Makovetsky, Piche, and Marsh 2018) and used a template for pseudo-segmentation of the tomograms. The resulting label-layer were manually validated by inspecting each tomographic slice and further tracing the flexible components that were averaged out during the refinement (i.e. the cMyBP-C links from thick to thin filament).

After clearly identifying and segmenting 76 cMyBP-C links in our tomograms, we measured the angle that the link formed relative to the thick filament z-axis, using the position of the C7 domain as pivot point. The angular distribution was plotted in GraphPad Prism.

3.4.10 Data availability

Cryo-ET structures have been deposited to the Electron Microscopy Data Bank (EMDB) under accession numbers: EMD-16986 (thin filament with masked out tropomyosin) [https://www.ebi.ac.uk/emdb/EMD-16986], EMD-16987 (thin filament including tropomyosin)

[https://www.ebi.ac.uk/emdb/EMD-16987], EMD-16990 (Crowns P2-A1 from the relaxed thick filament) [https://www.ebi.ac.uk/emdb/EMD-16990], EMD-16991 (M-band from the relaxed thick filament) [https://www.ebi.ac.uk/emdb/EMD-16991], EMD-16992 (Crowns A15-A29 from the relaxed thick filament) [https://www.ebi.ac.uk/emdb/EMD-16992], EMD-16993 (Crown P1 from the relaxed thick filament) [https://www.ebi.ac.uk/emdb/EMD-16993], EMD-16994 (Crowns A11-A15 from the relaxed thick filament) [https://www.ebi.ac.uk/emdb/EMD-16994], EMD-16995 (Crowns A8-A12 from the relaxed thick filament) [https://www.ebi.ac.uk/emdb/EMD-16995], EMD-16996 (Crowns A5-A7 from the relaxed thick filament) [https://www.ebi.ac.uk/emdb/EMD-16996], EMD-16997 (Crowns A1-A5 from the relaxed thick filament) [https://www.ebi.ac.uk/emdb/EMD-16997].

Representative tomograms have been deposited under accession numbers EMD-16989 (Tomogram of sarcomere M-band to C-zone from mouse cardiac muscle) [https://www.ebi.ac.uk/emdb/EMD-16989] and EMD-16988 (Tomogram of sarcomere C-zone from mouse cardiac muscle) [https://www.ebi.ac.uk/emdb/EMD-16988].

4 Extended Data

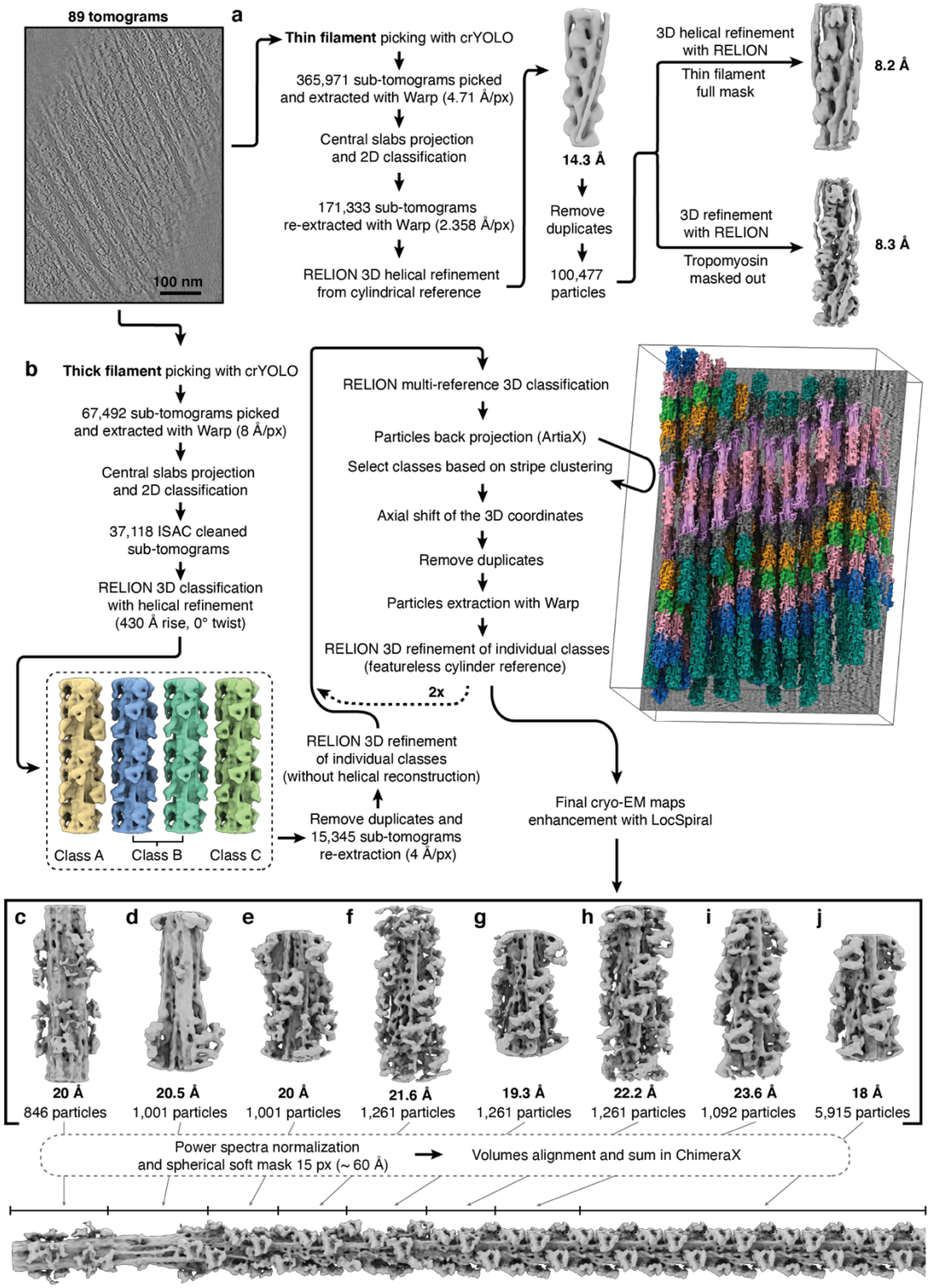

Extended Data Figure 1 Data acquisition and processing pipeline.

*The thin (**a**) and thick filament (**b**). Cryo-EM enhanced maps for: M-band (**c**), A-M transition to crown P1 (**d**), from crown P2 to A1 (**e**), from crown A1 to A5 (**f**), from crown A5 to A7 (**g**), from crown A8 to A12 (**h**), from crown A11 to A15 (**i**), and the combined segments from crown A15 to A29 (**j**)*

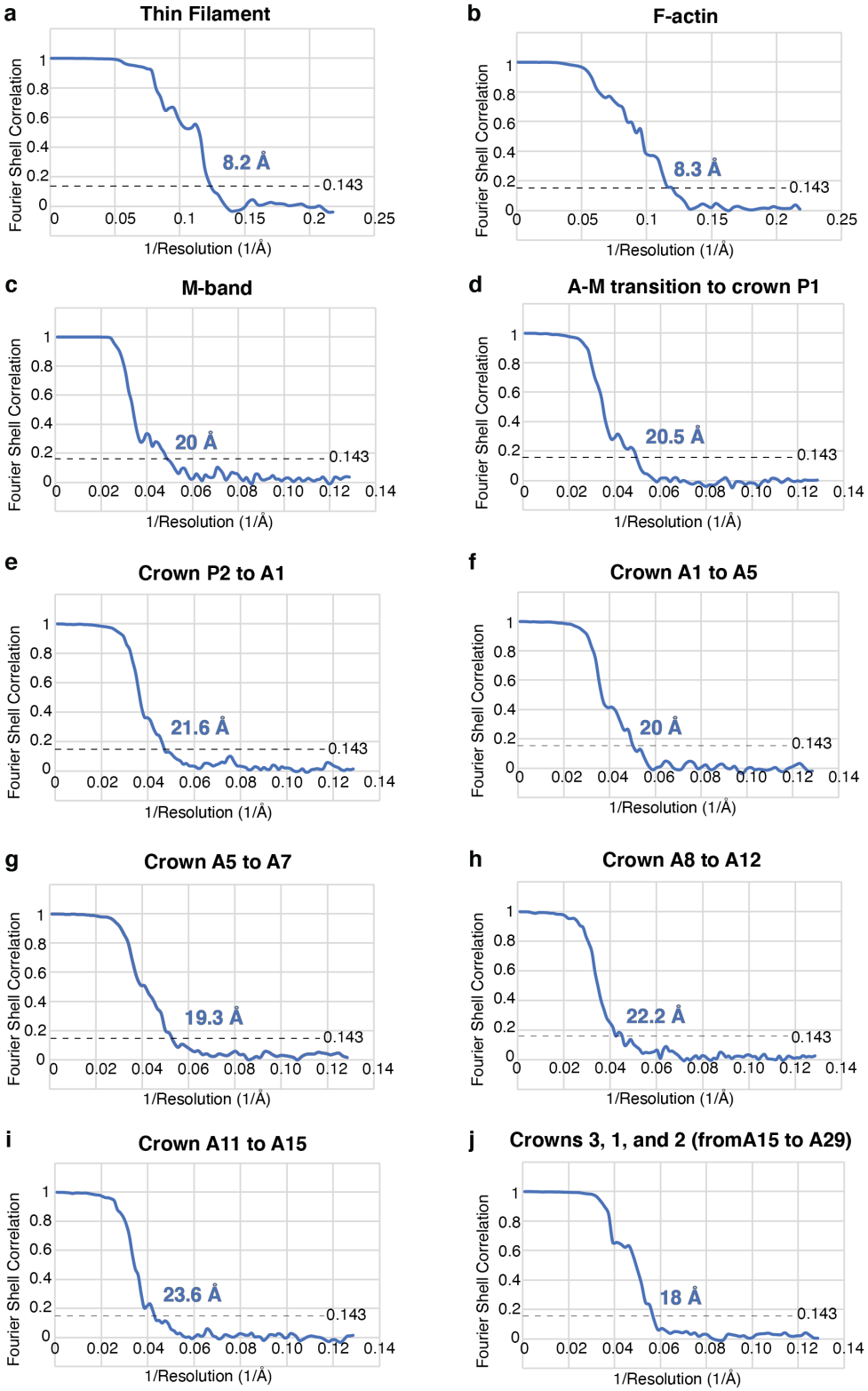

Extended Data Figure 2 Gold-standard FSC curves.

of the cardiac native thin filament ***(a)*** *and F-actin, after masking out tropomyosin* ***(b).*** *Gold-standard FSC curves of the different segments of the relaxed thick filament: M-band* ***(c),*** *A-M transition to crown P1* ***(d),*** *from crown P2 to A1* ***(e),*** *from crown A1 to A5* ***(f),*** *from crown A5 to A7* ***(g),*** *from crown A8 to A12* ***(h),*** *from crown A11 to A15* ***(i),*** *and the combined segments from crown A15 to A29* ***(j).***

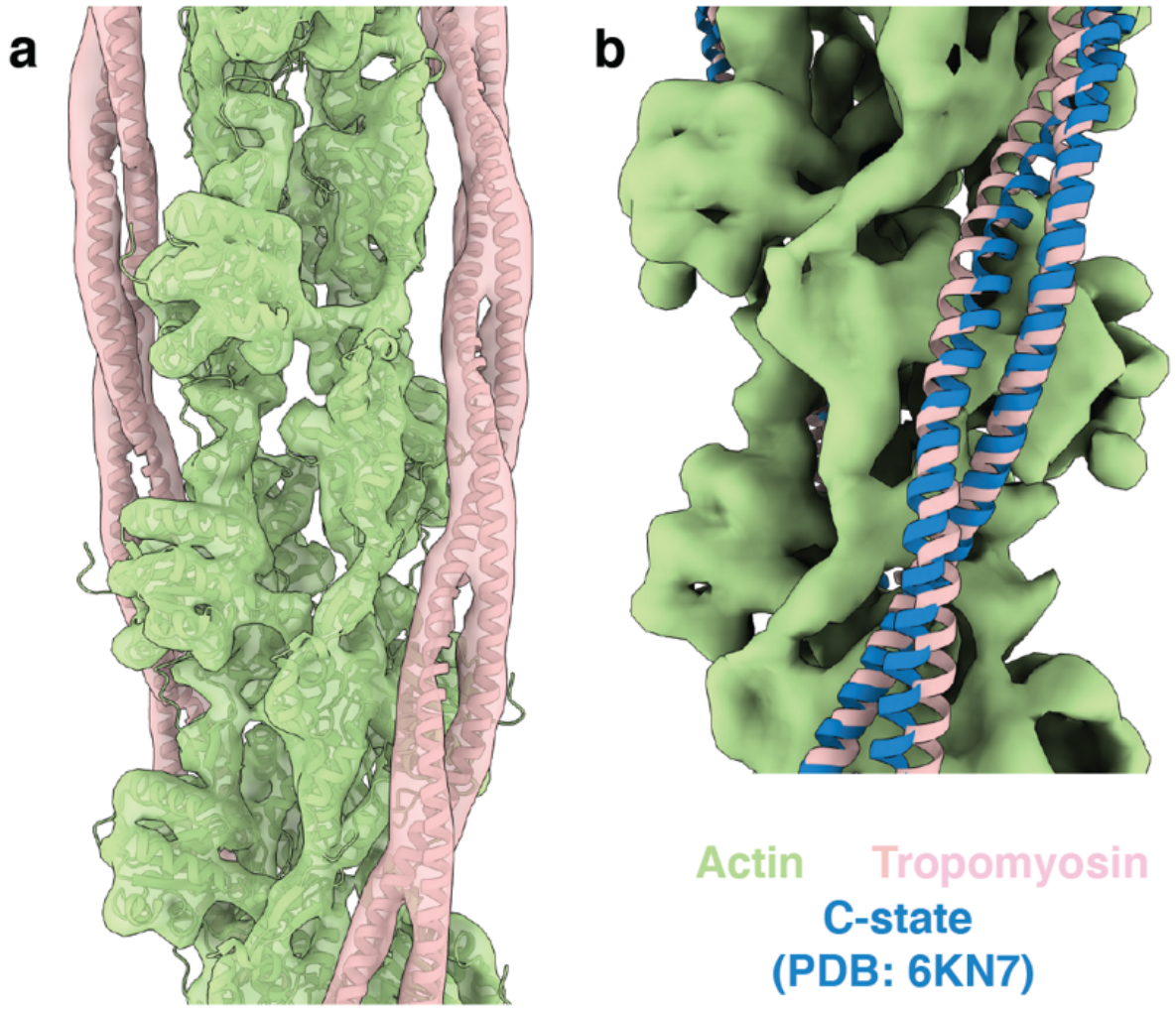

Extended Data Figure 3 In situ structure of the thin filament in the Ca^{2+} free state.

***a**, Subtomogram-averaged structure of the thin filament in the relaxed sarcomere. **b**, Model of the B-state of tropomyosin (PDB: 6KN7) is shown for comparison.*

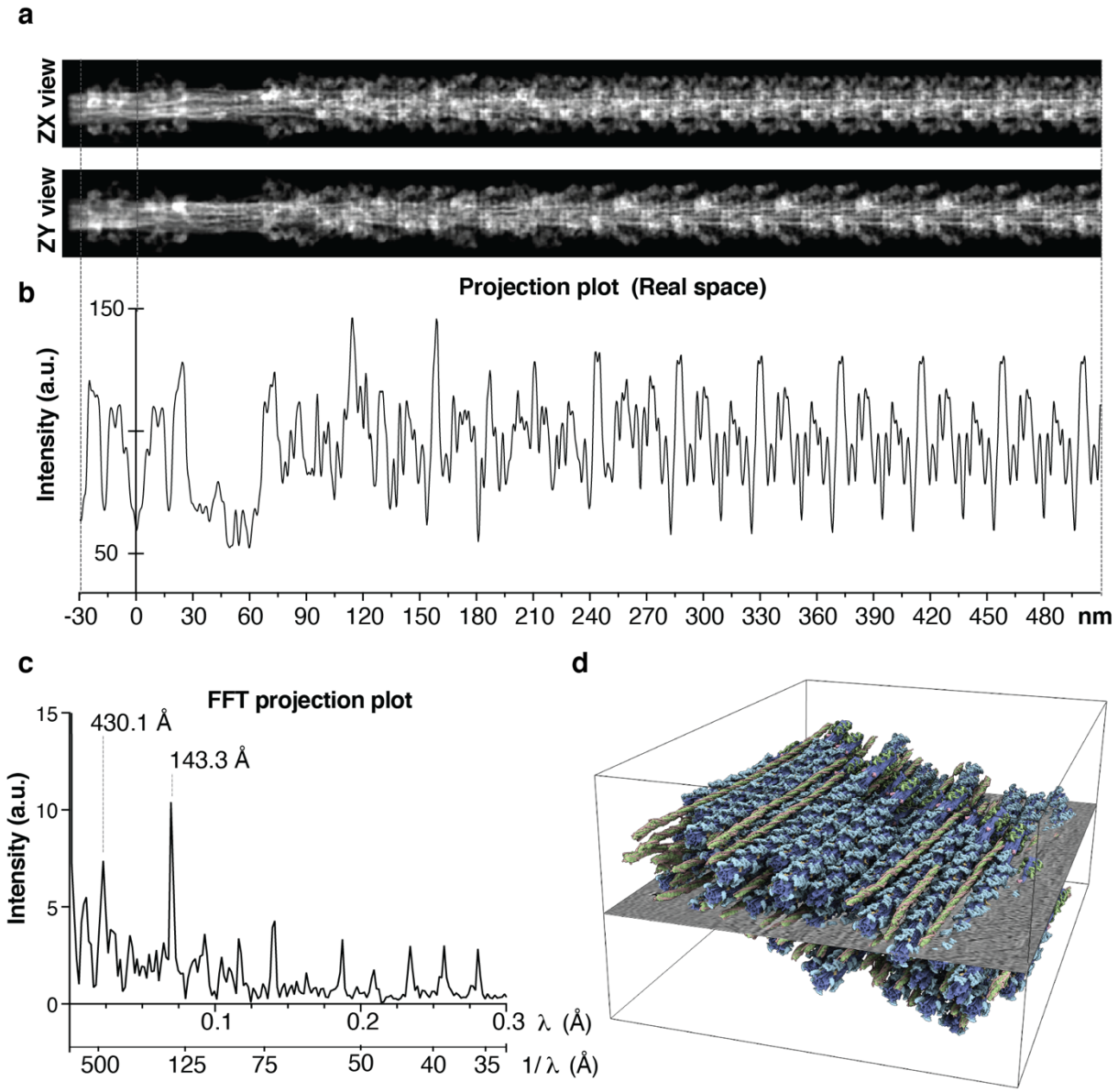

Extended Data Figure 4 Thick filament density projection and profile.

***a**, The three-dimensional map of the thick filament was projected by summing the intensities of the voxels along the x axis. **b**, Intensity profile along the x axis, revealing the periodicity and spacing of the repeating units in the thick filament. **c**, The Fast Fourier Transform (FFT) of the intensity profile shows the peaks resulting from the repetitive nature of its component. The 430 Å peak is associated to the C-type SRs while the 143.3 Å peak is associated to the crowns layers and was used to calibrate the pixel size of the reconstruction. **d**, Tomographic volume of a cardiac sarcomere A-band showing thick and thin filaments back-plotted into the reconstructed volume with a single tomographic slice at the center for orientation.*

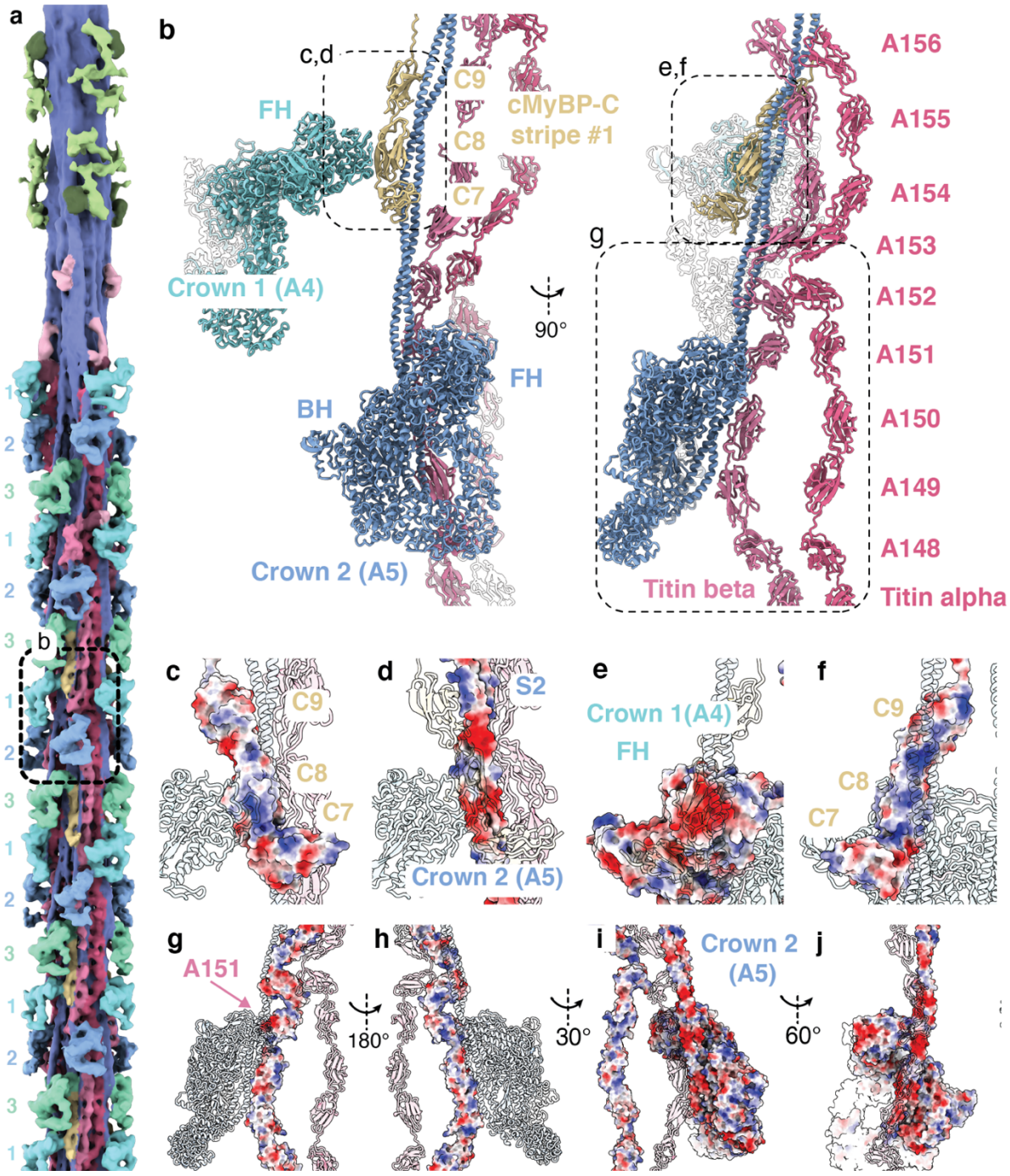

Extended Data Figure 5 The OFF state of crowns 1 and 2 is stabilized by interactions with titin and cMyBP-C.

***a**, An overview of the thick filament from the M-band to the fourth cMyBP-C stripe is provided for context. **b**, Simplified molecular model of the titin CSR10. **c-f**, Crown 1 FH binds stably to the C8 domain of cMyBP-C via an extensive network of complementary charges (**c,d**), while C8 and C9 bind to the first 80 amino acids of crown 2 tails (**e,f**). **g-j**, The same tail region interact with titin beta domains (**g,h**). The OFF state of crown 2 is further stabilized by interactions with A151 (**i,j**).*

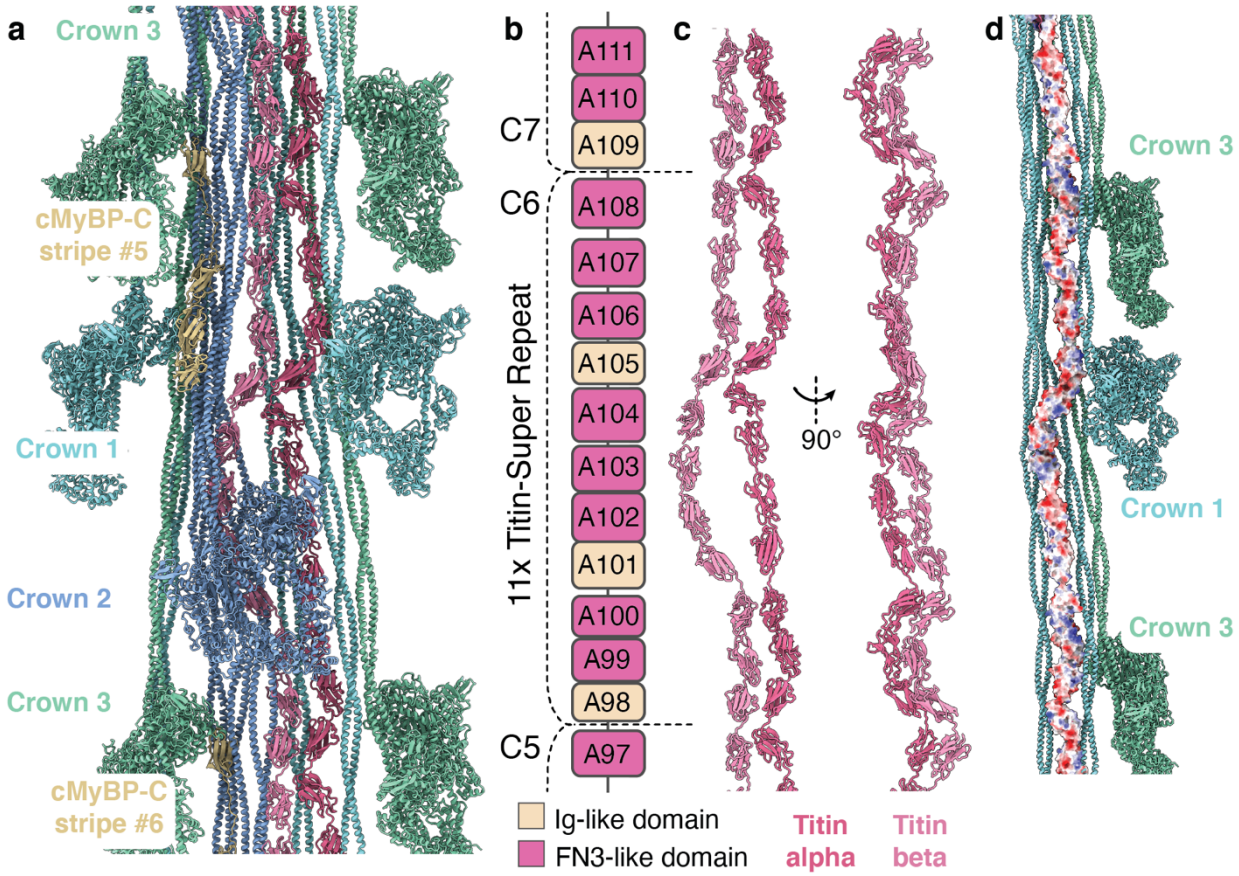

Extended Data Figure 6 Titin organization in the center of the C-zone.

***a**, Simplified overview of a single asymmetrical unit at CSR6, showing the molecular arrangement of the myosin crowns, titin and cMyBP-C. **b**, Domain map of titin C-type super-repeat. **c**, Titin alpha and titin beta chain run parallel to each other and interact at the 1st, 3rd, 8th, and 11th CSR domains. **d**, Binding of titin to S2 and LMM of crowns 1 and 3 is reliant on a network of electrostatic interactions.*

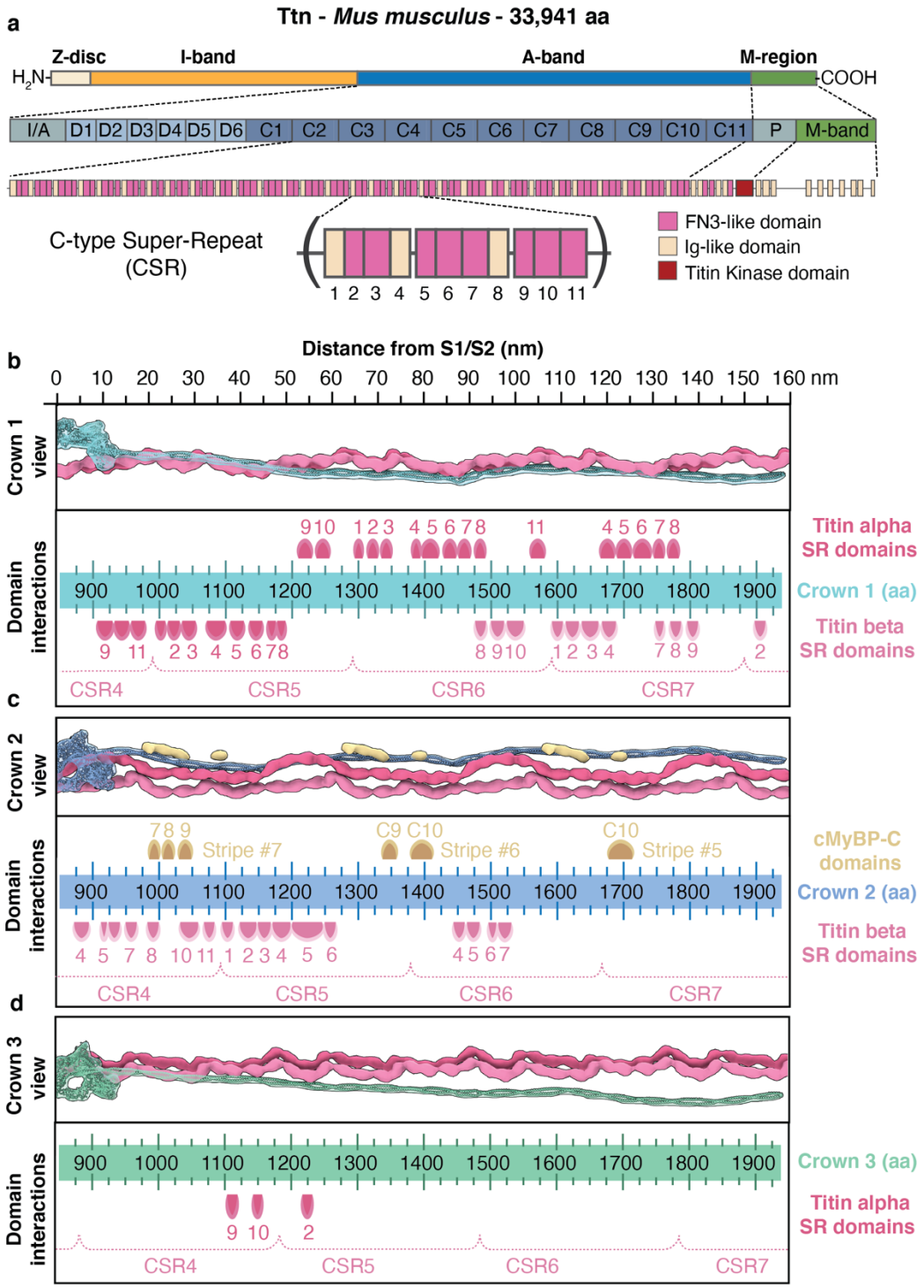

Extended Data Figure 7 Titin's domain interactions with myosin tails.

a, *Domain map of titin, showing its highly modular organization. The A-band comprises six D-type super-repeats in the distal zone (D-type SRs) and eleven 11x super-repeats in the central zone (C-type SRs). The proximal region (P-zone) contains the Titin Kinase domain (TK domain), while the M-band region presents ten Ig-like domains connected by seven disordered inter-spacing regions, m1-9 and is1-7, respectively.* ***b****, The model of crown 1 is shown alongside the densities of titin. To allow a clearer interpretation, a binding site map was generated to depict the amino acid residues of the myosin tail and their distance from the S1/S2 site.* ***c****, The arrangement and interactions of crown 2 are visualized alongside the densities of cMyBP-C and using the same approach as in (****b****).* ***d****, Similarly, the interaction of crown 3 with titin is shown.*

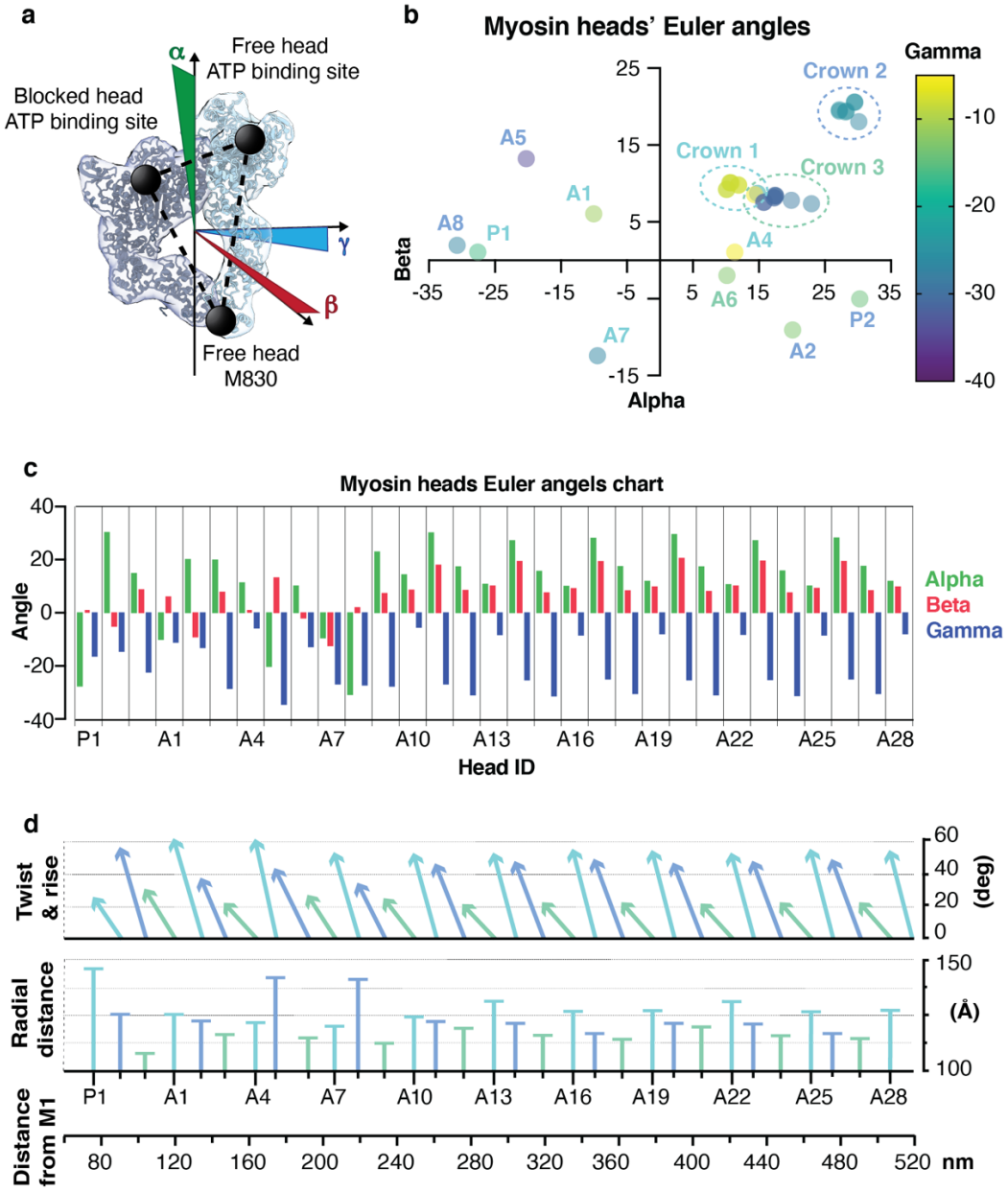

Extended Data Figure 8 Position and orientation of myosin heads at each crown.

a*, The arrangement of myosin heads deviates from a canonical helical symmetry. To quantitatively describe this arrangement, the thick filament was modeled as a cylinder, and the myosin IHMs were represented as triangles on its surface. The vertices of the triangle were determined by the coordinates of three points: the ATP-binding site in the FH, the same site in the BH, and the S1/S2 junction site. The Euler angles for the IHM are calculated relative to an equilateral triangle that has its topmost side perpendicular to the cylinder axis and parallel to its base.* ***b****, Colored scatter plot of the myosin crowns from P1 to A28. Alpha and beta angles are plotted along the x and y axes, respectively, while the gamma angle is encoded by the color gradient. Plotting of the IHMs generates three orientation clusters for the crowns from A10 to A28, while crowns associated to the P-zone or the first three C-type titin SR show more inconsistent orientation.* ***c****, A more detailed representation of* ***(b)*** *is shown in a colored histogram.* ***d****, Using the cylindrical coordinates for the triangles, we obtain the cylindrical coordinates for each myosin crown and plotted their twist, rise, and radial distance. Similar to the Euler angle distribution, a more consistent pseudo-helical pattern appears from A10 onwards. P1, A5, and A8, show outstanding orientation and radial distances, indicative of a more outward projected configuration.*

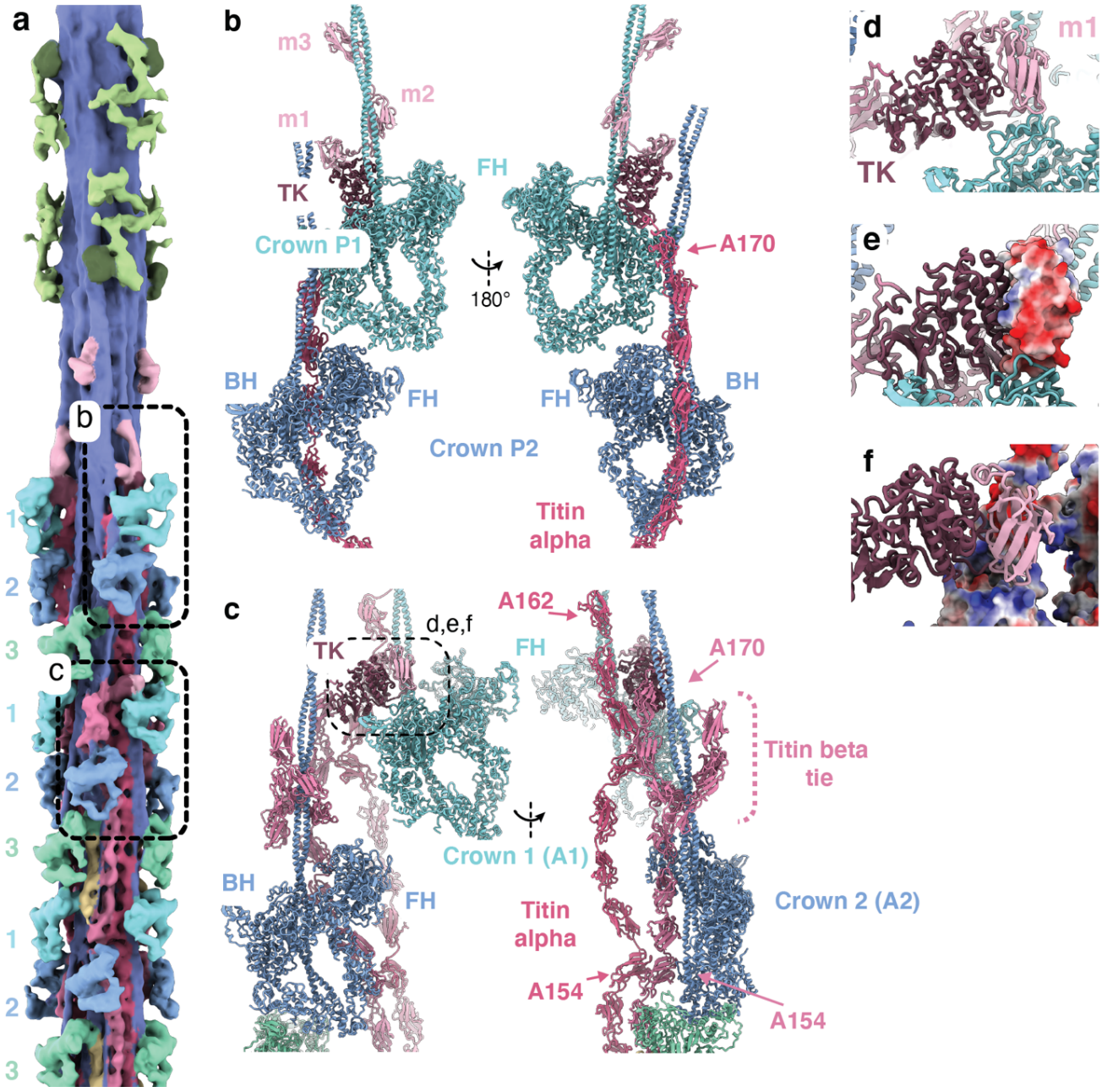

Extended Data Figure 9 The P-zone of the thick filament.

***a**, An overview of the thick filament from the M-band to the fourth cMyBP-C stripe is provided for context. **b**, The P-zone of titin alpha is located behind the first two crowns, P1 and P2 while TK, m1, m2, and m3 are binding to P1's S1 and S2 domains. However, no density could be assigned to titin beta in this region. **c**, Titin beta chains clearly run alongside titin alpha chains until domain A154, and just behind the crown A2 motor domains. In this region, we observe additional globular densities, forming a flexible bow tie-shaped structure, which wraps around the tail of crown A2 and projects outward. These densities were assigned to titin beta P-zone domains. **d-f**, On top of crown A1, we observe an additional density that we attributed to the TK-m1 complex. In this configuration, m1 is positioned on top of the crown A2 BH and interacts with it mainly via electrostatic interactions.*

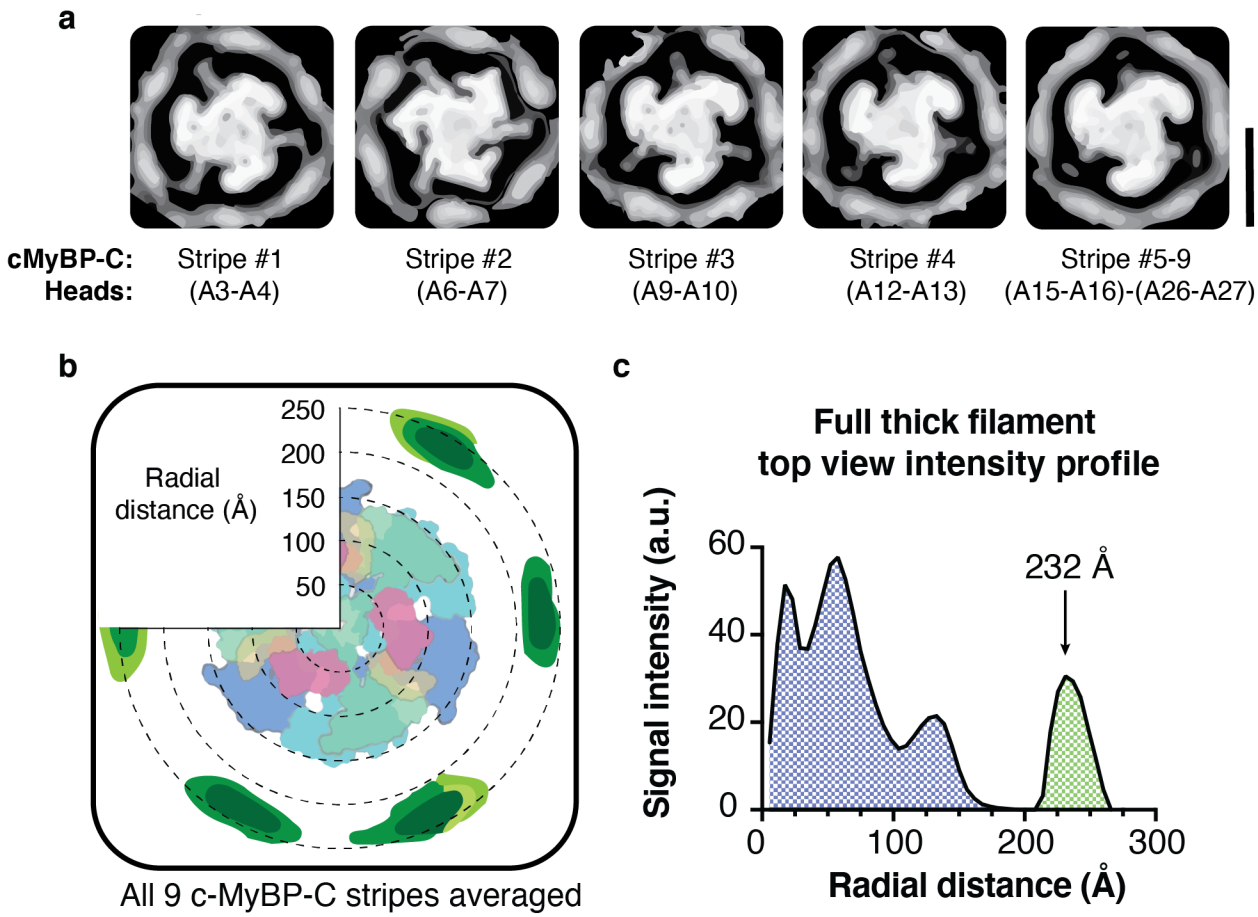

Extended Data Figure 10 C-zone lattice organization.

a*, The bridging domains of cMyBP-C exhibit a high degree of flexibility. To visualize the relative position of the thin filaments and the bridging cMyBP-C region with respect to the thick filament core, we centered each of the nine stripes individually on the cMyBP-C C7 plane and projected the resulting central 40 Å slab along the z-axis. Our analysis showed that stripes 4 to 9 projected into a region equidistant from both the negative azimuthal angle thin filament (NA-TF) and the positive azimuthal angle-thin filament (PA-TF), indicating that cMyBP-C may bind to either of them with equal likelihood. In contrast, stripes 2 showed a preferential orientation towards NA-TF, while stripe 1 exhibited a clear preferential bias towards PA-TF.* ***b****,****c****, We generated a single contour map by averaging all nine stripes together, which was then used to obtain a model for the determination of the average thin filament distance and azimuthal angles for the entire 430 Å repeat. Our analysis revealed that the center-to-center distance from thick to thin filament was 232 Å, as demonstrated by the radial profile of the signal intensity of a full 430 Å repeat. Scale bars: 25 nm.*

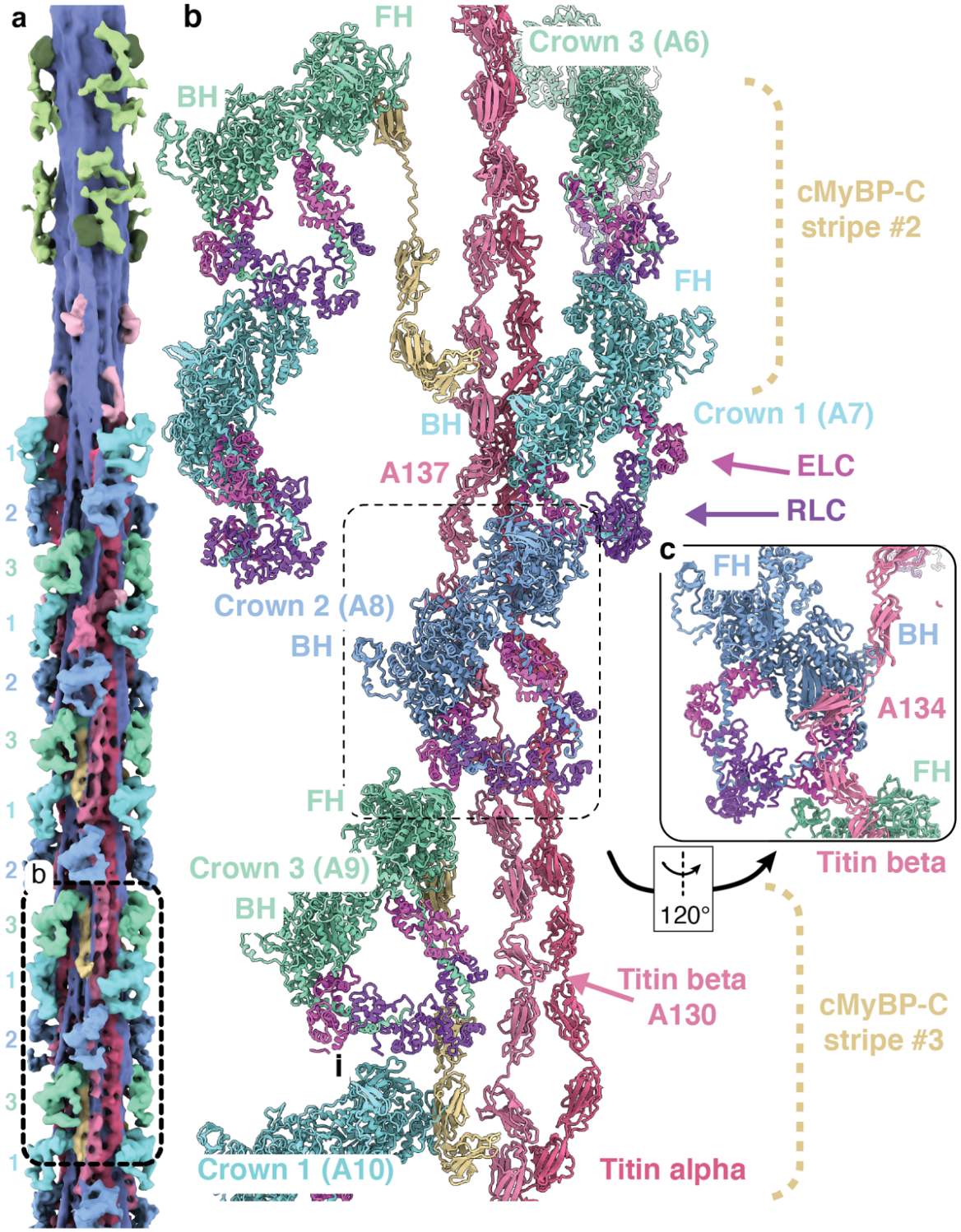

Extended Data 11 Figure Myosin OFF state is stabilized by myosin light chains at CSR9.

***a**, An overview of the thick filament from the M-band to the third cMyBP-C stripe is provided for context. **b**, Simplified overview of a single asymmetrical unit at CSR9, showing the molecular arrangement of the myosin crowns, titin and cMyBP-C. In contrast to all other cMyBP-C, at stripe #2 the crown 1 does not interact with cMyBP-C CTD, instead its FH binds to the RLC from crown 3 and its BH interacts with titin A137. Crown 2 orientation is also atypical as its FH interacts with the disordered region of Crown1's ELC and its BH binds to titin A134 (**c**). Similarly, crown 3 (A9)'s FH binds to the crown 2's ELC and it is also stabilized by an interaction of its RLC with titin beta A130.*

CHAPTER 4 References

Adewale, Adeleye O., and Young-Hoon Ahn. 2021. 'Titin N2A Domain and Its Interactions at the Sarcomere'. *International Journal of Molecular Sciences* 22 (14): 7563. https://doi.org/10.3390/ijms22147563.

Alamo, Lorenzo, Natalia Koubassova, Antonio Pinto, Richard Gillilan, Andrey Tsaturyan, and Raúl Padrón. 2017. 'Lessons from a Tarantula: New Insights into Muscle Thick Filament and Myosin Interacting-Heads Motif Structure and Function'. *Biophysical Reviews* 9 (5): 461–80. https://doi.org/10.1007/s12551-017-0295-1.

Alamo, Lorenzo, James S Ware, Antonio Pinto, Richard E Gillilan, Jonathan G Seidman, Christine E Seidman, and Raúl Padrón. 2017. 'Effects of Myosin Variants on Interacting-Heads Motif Explain Distinct Hypertrophic and Dilated Cardiomyopathy Phenotypes'. Edited by Jeffrey Robbins. *eLife* 6 (June): e24634. https://doi.org/10.7554/eLife.24634.

Alamo, Lorenzo, Willy Wriggers, Antonio Pinto, Fulvia Bártoli, Leiria Salazar, Fa-Qing Zhao, Roger Craig, and Raúl Padrón. 2008. 'Three-Dimensional Reconstruction of Tarantula Myosin Filaments Suggests How Phosphorylation May Regulate Myosin Activity'. *Journal of Molecular Biology* 384 (4): 780–97. https://doi.org/10.1016/j.jmb.2008.10.013.

Al-Khayat, Hind A., Robert W. Kensler, Edward P. Morris, and John M. Squire. 2010. 'Three-Dimensional Structure of the M-Region (Bare Zone) of Vertebrate Striated Muscle Myosin Filaments by Single-Particle Analysis'. *Journal of Molecular Biology* 403 (5): 763–76. https://doi.org/10.1016/j.jmb.2010.09.025.

Al-Khayat, Hind A., Robert W. Kensler, John M. Squire, Steven B. Marston, and Edward P. Morris. 2013. 'Atomic Model of the Human Cardiac Muscle Myosin Filament'. *Proceedings of the National Academy of Sciences* 110 (1): 318–23. https://doi.org/10.1073/pnas.1212708110.

Al-Khayat, Hind A., Edward P. Morris, Robert W. Kensler, and John M. Squire. 2008. 'Myosin Filament 3D Structure in Mammalian Cardiac Muscle'. *Journal of Structural Biology* 163 (2): 117–26. https://doi.org/10.1016/j.jsb.2008.03.011.

Allingham, John S., Robert Smith, and Ivan Rayment. 2005. 'The Structural Basis of Blebbistatin Inhibition and Specificity for Myosin II'. *Nature Structural & Molecular Biology* 12 (4): 378–79. https://doi.org/10.1038/nsmb908.

Alyonycheva, T., L. Cohen-Gould, C. Siewert, D. A. Fischman, and T. Mikawa. 1997. 'Skeletal Muscle-Specific Myosin Binding Protein-H Is Expressed in Purkinje Fibers of the Cardiac Conduction System'. *Circulation Research* 80 (5): 665–72. https://doi.org/10.1161/01.res.80.5.665.

Amat, Fernando, Daniel Castaño-Diez, Albert Lawrence, Farshid Moussavi, Hanspeter Winkler, and Mark Horowitz. 2010. 'Chapter Thirteen - Alignment of Cryo-Electron Tomography Datasets'. In *Methods in Enzymology*, edited by Grant J. Jensen, 482:343–67. Cryo-EM, Part B: 3-D Reconstruction. Academic Press. https://doi.org/10.1016/S0076-6879(10)82014-2.

Anderson, Robert L., Darshan V. Trivedi, Saswata S. Sarkar, Marcus Henze, Weikang Ma, Henry Gong, Christopher S. Rogers, et al. 2018. 'Deciphering the Super Relaxed State of Human β-Cardiac Myosin and the Mode of Action of Mavacamten from Myosin Molecules to Muscle Fibers'. *Proceedings of the National Academy of Sciences* 115 (35): E8143–52. https://doi.org/10.1073/pnas.1809540115.

Baker, Lindsay A, Michael Grange, and Kay Grünewald. 2017. 'Electron Cryo-Tomography Captures Macromolecular Complexes in Native Environments'. *Current Opinion in Structural Biology*, Cryo electron microscopy: exciting advances in CryoEM herald a new

era in structural biology • Biophysical methods: behind the scenes of the cryo-EM revolution, 46 (October): 149–56. https://doi.org/10.1016/j.sbi.2017.08.005.
Barefield, David, and Sakthivel Sadayappan. 2010. 'Phosphorylation and Function of Cardiac Myosin Binding Protein-C in Health and Disease'. *Journal of Molecular and Cellular Cardiology*, Special Issue: Cardiac Sarcomeres and the Integrated Biology of Excitation Contraction Coupling, 48 (5): 866–75. https://doi.org/10.1016/j.yjmcc.2009.11.014.
Barrick, Samantha K., and Michael J. Greenberg. 2021. 'Cardiac Myosin Contraction and Mechanotransduction in Health and Disease'. *Journal of Biological Chemistry* 297 (5). https://doi.org/10.1016/j.jbc.2021.101297.
Bennett, Pauline, Roger Craig, Roger Starr, and Gerald Offer. 1986. 'The Ultrastructural Location of C-Protein, X-Protein and H-Protein in Rabbit Muscle'. *Journal of Muscle Research & Cell Motility* 7 (6): 550–67. https://doi.org/10.1007/BF01753571.
Bennett, Pauline, Martin Rees, and Mathias Gautel. 2020. 'The Axial Alignment of Titin on the Muscle Thick Filament Supports Its Role as a Molecular Ruler'. *Journal of Molecular Biology* 432 (17): 4815–29. https://doi.org/10.1016/j.jmb.2020.06.025.
Berger, Casper, Navya Premaraj, Raimond B. G. Ravelli, Kèvin Knoops, Carmen López-Iglesias, and Peter J. Peters. 2023. 'Cryo-Electron Tomography on Focused Ion Beam Lamellae Transforms Structural Cell Biology'. *Nature Methods* 20 (4): 499–511. https://doi.org/10.1038/s41592-023-01783-5.
Betts, J. Gordon. 2013. *Anatomy and Physiology*. OpenStax College, Rice University.
Bharat, Tanmay A. M., and Sjors H. W. Scheres. 2016. 'Resolving Macromolecular Structures from Electron Cryo-Tomography Data Using Subtomogram Averaging in RELION'. *Nature Protocols* 11 (11): 2054–65. https://doi.org/10.1038/nprot.2016.124.
Bogomolovas, Julius, Jennifer R Fleming, Barbara Franke, Bruno Manso, Bernd Simon, Alexander Gasch, Marija Markovic, et al. 2021. 'Titin Kinase Ubiquitination Aligns Autophagy Receptors with Mechanical Signals in the Sarcomere'. *EMBO Reports* 22 (10): e48018. https://doi.org/10.15252/embr.201948018.
Bonne, Gisèle, Lucie Carrier, Josiane Bercovici, Corinne Cruaud, Pascale Richard, Bernard Hainque, Mathias Gautel, et al. 1995. 'Cardiac Myosin Binding Protein–C Gene Splice Acceptor Site Mutation Is Associated with Familial Hypertrophic Cardiomyopathy'. *Nature Genetics* 11 (4): 438–40. https://doi.org/10.1038/ng1295-438.
Brunello, Elisabetta, and Luca Fusi. 2024. 'Regulating Striated Muscle Contraction: Through Thick and Thin'. *Annual Review of Physiology* 86 (1): null. https://doi.org/10.1146/annurev-physiol-042222-022728.
Brunello, Elisabetta, Luca Fusi, Andrea Ghisleni, So-Jin Park-Holohan, Jesus G. Ovejero, Theyencheri Narayanan, and Malcolm Irving. 2020. 'Myosin Filament-Based Regulation of the Dynamics of Contraction in Heart Muscle'. *Proceedings of the National Academy of Sciences* 117 (14): 8177–86. https://doi.org/10.1073/pnas.1920632117.
Buchholz, Tim-Oliver, Alexander Krull, Réza Shahidi, Gaia Pigino, Gáspár Jékely, and Florian Jug. 2019. 'Content-Aware Image Restoration for Electron Microscopy'. *Methods in Cell Biology* 152: 277–89. https://doi.org/10.1016/bs.mcb.2019.05.001.
Caremani, Marco, Elisabetta Brunello, Marco Linari, Luca Fusi, Thomas C. Irving, David Gore, Gabriella Piazzesi, Malcolm Irving, Vincenzo Lombardi, and Massimo Reconditi. 2019. 'Low Temperature Traps Myosin Motors of Mammalian Muscle in a Refractory State That Prevents Activation'. *Journal of General Physiology* 151 (11): 1272–86. https://doi.org/10.1085/jgp.201912424.
Charton, Karine, Jaakko Sarparanta, Anna Vihola, Astrid Milic, Per Harald Jonson, Laurence Suel, Helena Luque, Imène Boumela, Isabelle Richard, and Bjarne Udd. 2015. 'CAPN3-Mediated Processing of C-Terminal Titin Replaced by Pathological Cleavage in Titinopathy'. *Human Molecular Genetics* 24 (13): 3718–31. https://doi.org/10.1093/hmg/ddv116.

Cleaver, J. R. A. 1975. ‘Field Emission Guns for Electron Probe Instruments’. *International Journal of Electronics* 38 (4): 513–29. https://doi.org/10.1080/00207217508920422.
Colpan, Mert, Jessika Iwanski, and Carol C. Gregorio. 2021. ‘CAP2 Is a Regulator of Actin Pointed End Dynamics and Myofibrillogenesis in Cardiac Muscle’. *Communications Biology* 4 (1): 1–15. https://doi.org/10.1038/s42003-021-01893-w.
Cooper, John A., and David Sept. 2008. ‘New Insights into Mechanism and Regulation of Actin Capping Protein’. In *International Review of Cell and Molecular Biology*, 267:183–206. Academic Press. https://doi.org/10.1016/S1937-6448(08)00604-7.
Craig, R., G. Offer, and Brian Blundell Boycott. 1976. ‘The Location of C-Protein in Rabbit Skeletal Muscle’. *Proceedings of the Royal Society of London. Series B. Biological Sciences* 192 (1109): 451–61. https://doi.org/10.1098/rspb.1976.0023.
Craig, Roger, and Raúl Padrón. 2022. ‘Structural Basis of the Super- and Hyper-Relaxed States of Myosin II’. *Journal of General Physiology* 154 (1). https://doi.org/10.1085/jgp.202113012.
Crocini, Claudia, and Michael Gotthardt. 2021. ‘Cardiac Sarcomere Mechanics in Health and Disease’. *Biophysical Reviews* 13 (5): 637–52. https://doi.org/10.1007/s12551-021-00840-7.
Daneshparvar, Nadia, Dianne W. Taylor, Thomas S. O’Leary, Hamidreza Rahmani, Fatemeh Abbasiyeganeh, Michael J. Previs, and Kenneth A. Taylor. 2020. ‘CryoEM Structure of Drosophila Flight Muscle Thick Filaments at 7 Å Resolution’. *Life Science Alliance* 3 (8). https://doi.org/10.26508/lsa.202000823.
Danev, Radostin, Haruaki Yanagisawa, and Masahide Kikkawa. 2019. ‘Cryo-Electron Microscopy Methodology: Current Aspects and Future Directions’. *Trends in Biochemical Sciences* 44 (10): 837–48. https://doi.org/10.1016/j.tibs.2019.04.008.
Dubochet, J., J. Lepault, R. Freeman, J. A. Berriman, and J.-C. Homo. 1982. ‘Electron Microscopy of Frozen Water and Aqueous Solutions’. *Journal of Microscopy* 128 (3): 219–37. https://doi.org/10.1111/j.1365-2818.1982.tb04625.x.
Dubochet, Jacques, Marc Adrian, Jiin-Ju Chang, Jean Lepault, and Alasdair W. McDowall. 1987. ‘Cryoelectron Microscopy of Vitrified Specimens’. In *Cryotechniques in Biological Electron Microscopy*, edited by Rudolf Alexander Steinbrecht and Karl Zierold, 114–31. Berlin, Heidelberg: Springer. https://doi.org/10.1007/978-3-642-72815-0_5.
Ecken, Julian von der, Mirco Müller, William Lehman, Dietmar J. Manstein, Pawel A. Penczek, and Stefan Raunser. 2015. ‘Structure of the F-Actin–Tropomyosin Complex’. *Nature* 519 (7541): 114–17. https://doi.org/10.1038/nature14033.
Eldemire, Ramone, Charles A. Tharp, Matthew R.G. Taylor, Orfeo Sbaizero, and Luisa Mestroni. 2021. ‘The Sarcomeric Spring Protein Titin: Biophysical Properties, Molecular Mechanisms, and Genetic Mutations Associated with Heart Failure and Cardiomyopathy’. *Current Cardiology Reports* 23 (9): 121. https://doi.org/10.1007/s11886-021-01550-y.
Ermel, Utz H., Serena M. Arghittu, and Achilleas S. Frangakis. 2022. ‘ArtiaX: An Electron Tomography Toolbox for the Interactive Handling of Sub-Tomograms in UCSF ChimeraX’. *Protein Science: A Publication of the Protein Society* 31 (12): e4472. https://doi.org/10.1002/pro.4472.
Faruqi, A. R, and R. Henderson. 2007. ‘Electronic Detectors for Electron Microscopy’. *Current Opinion in Structural Biology*, Carbohydrates and glycoconjugates / Biophysical methods, 17 (5): 549–55. https://doi.org/10.1016/j.sbi.2007.08.014.
Finley, Natosha L., and Tzvia I. Cuperman. 2014. ‘Cardiac Myosin Binding Protein-C: A Structurally Dynamic Regulator of Myocardial Contractility’. *Pflügers Archiv - European Journal of Physiology* 466 (3): 433–38. https://doi.org/10.1007/s00424-014-1451-0.
Foth, Bernardo J., Marc C. Goedecke, and Dominique Soldati. 2006. ‘New Insights into Myosin Evolution and Classification’. *Proceedings of the National Academy of Sciences* 103 (10): 3681–86. https://doi.org/10.1073/pnas.0506307103.

Franzini-Armstrong, Clara. 1970. 'Natural Variability in the Length of Thin and Thick Filaments in Single Fibres from a Crab, Portunus Depurator'. *Journal of Cell Science* 6 (2): 559–92. https://doi.org/10.1242/jcs.6.2.559.

Freiburg, Alexandra, and Mathias Gautel. 1996. 'A Molecular Map of the Interactions between Titin and Myosin-Binding Protein C'. *European Journal of Biochemistry* 235 (1–2): 317–23. https://doi.org/10.1111/j.1432-1033.1996.00317.x.

Fukuzawa, Atsushi, Stephan Lange, Mark Holt, Anna Vihola, Virginie Carmignac, Ana Ferreiro, Bjarne Udd, and Mathias Gautel. 2008. 'Interactions with Titin and Myomesin Target Obscurin and Obscurin-like 1 to the M-Band – Implications for Hereditary Myopathies'. *Journal of Cell Science* 121 (11): 1841–51. https://doi.org/10.1242/jcs.028019.

Fusi, L., E. Brunello, Z. Yan, and M. Irving. 2016. 'Thick Filament Mechano-Sensing Is a Calcium-Independent Regulatory Mechanism in Skeletal Muscle'. *Nature Communications* 7 (1): 13281. https://doi.org/10.1038/ncomms13281.

Gautel, Mathias. 2011. 'The Sarcomeric Cytoskeleton: Who Picks up the Strain?' *Current Opinion in Cell Biology*, Cell structure and dynamics, 23 (1): 39–46. https://doi.org/10.1016/j.ceb.2010.12.001.

Gautel, Mathias, and Kristina Djinović-Carugo. 2016. 'The Sarcomeric Cytoskeleton: From Molecules to Motion'. *Journal of Experimental Biology* 219 (2): 135–45. https://doi.org/10.1242/jeb.124941.

Gautel, Mathias, Dieter O. Fürst, Alessandra Cocco, and Stefano Schiaffino. 1998. 'Isoform Transitions of the Myosin Binding Protein C Family in Developing Human and Mouse Muscles'. *Circulation Research* 82 (1): 124–29. https://doi.org/10.1161/01.RES.82.1.124.

Geeves, M. A., and K. C. Holmes. 1999. 'Structural Mechanism of Muscle Contraction'. *Annual Review of Biochemistry* 68 (1): 687–728. https://doi.org/10.1146/annurev.biochem.68.1.687.

Gilbert, R., J.A. Cohen, S. Pardo, A. Basu, and D.A. Fischman. 1999. 'Identification of the A-Band Localization Domain of Myosin Binding Proteins C and H (MyBP-C, MyBP-H) in Skeletal Muscle'. *Journal of Cell Science* 112 (1): 69–79. https://doi.org/10.1242/jcs.112.1.69.

Glaeser, Robert M., Wim J. H. Hagen, Bong-Gyoon Han, Richard Henderson, Greg McMullan, and Christopher J. Russo. 2021. 'Defocus-Dependent Thon-Ring Fading'. *Ultramicroscopy* 222 (March): 113213. https://doi.org/10.1016/j.ultramic.2021.113213.

Gokhin, David S., Nancy E. Kim, Sarah A. Lewis, Heinz R. Hoenecke, Darryl D. D'Lima, and Velia M. Fowler. 2012. 'Thin-Filament Length Correlates with Fiber Type in Human Skeletal Muscle'. *American Journal of Physiology-Cell Physiology* 302 (3): C555–65. https://doi.org/10.1152/ajpcell.00299.2011.

Gollapudi, Sampath K., Weikang Ma, Srinivas Chakravarthy, Ariana C. Combs, Na Sa, Stephen Langer, Thomas C. Irving, and Suman Nag. 2021. 'Two Classes of Myosin Inhibitors, Para-Nitroblebbistatin and Mavacamten, Stabilize β-Cardiac Myosin in Different Structural and Functional States'. *Journal of Molecular Biology* 433 (23): 167295. https://doi.org/10.1016/j.jmb.2021.167295.

Grant, Timothy, and Nikolaus Grigorieff. 2015. 'Measuring the Optimal Exposure for Single Particle Cryo-EM Using a 2.6 Å Reconstruction of Rotavirus VP6'. Edited by Wesley I Sundquist. *eLife* 4 (May): e06980. https://doi.org/10.7554/eLife.06980.

Granzier, H. L., H. A. Akster, and H. E. Ter Keurs. 1991. 'Effect of Thin Filament Length on the Force-Sarcomere Length Relation of Skeletal Muscle'. *American Journal of Physiology-Cell Physiology* 260 (5): C1060–70. https://doi.org/10.1152/ajpcell.1991.260.5.C1060.

Granzier, Henk L., and Siegfried Labeit. 2004. 'The Giant Protein Titin'. *Circulation Research* 94 (3): 284–95. https://doi.org/10.1161/01.RES.0000117769.88862.F8.

Green, Eric M., Hiroko Wakimoto, Robert L. Anderson, Marc J. Evanchik, Joshua M. Gorham, Brooke C. Harrison, Marcus Henze, et al. 2016. 'A Small-Molecule Inhibitor of Sarcomere Contractility Suppresses Hypertrophic Cardiomyopathy in Mice'. *Science* 351 (6273): 617–21. https://doi.org/10.1126/science.aad3456.

Grinzato, Alessandro, Daniel Auguin, Carlos Kikuti, Neha Nandwani, Dihia Moussaoui, Divya Pathak, Eaazhisai Kandiah, et al. 2023. 'Cryo-EM Structure of the Folded-Back State of Human β-Cardiac Myosin'. *Nature Communications* 14 (1): 3166. https://doi.org/10.1038/s41467-023-38698-w.

Gubbens, Alexander, Melanie Barfels, Colin Trevor, Ray Twesten, Paul Mooney, Paul Thomas, Nanda Menon, Bernd Kraus, Chengye Mao, and Brian McGinn. 2010. 'The GIF Quantum, a next Generation Post-Column Imaging Energy Filter'. *Ultramicroscopy*, PROCEEDINGS OF THE INTERNATIONAL WORKSHOP ON ENHANCED DATA GENERATED BY ELECTRONS, 110 (8): 962–70. https://doi.org/10.1016/j.ultramic.2010.01.009.

Guckenberger, R. 1982. 'Determination of a Common Origin in the Micrographs of Tilt Series in Three-Dimensional Electron Microscopy'. *Ultramicroscopy* 9 (1): 167–73. https://doi.org/10.1016/0304-3991(82)90239-X.

Hagen, Wim J. H., William Wan, and John A. G. Briggs. 2017. 'Implementation of a Cryo-Electron Tomography Tilt-Scheme Optimized for High Resolution Subtomogram Averaging'. *Journal of Structural Biology*, Electron Tomography, 197 (2): 191–98. https://doi.org/10.1016/j.jsb.2016.06.007.

Hands-Portman, Ian, and Saskia E. Bakker. 2022. 'Customising the Plunge-Freezing Workflow for Challenging Conditions'. *Faraday Discussions* 240 (0): 44–54. https://doi.org/10.1039/D2FD00060A.

Hanft, Laurin M., Daniel P. Fitzsimons, Timothy A. Hacker, Richard L. Moss, and Kerry S. McDonald. 2021. 'Cardiac MyBP-C Phosphorylation Regulates the Frank–Starling Relationship in Murine Hearts'. *Journal of General Physiology* 153 (7). https://doi.org/10.1085/jgp.202012770.

Harris, Samantha P., Betty Belknap, Robert E. Van Sciver, Howard D. White, and Vitold E. Galkin. 2016. 'C0 and C1 N-Terminal Ig Domains of Myosin Binding Protein C Exert Different Effects on Thin Filament Activation'. *Proceedings of the National Academy of Sciences* 113 (6): 1558–63. https://doi.org/10.1073/pnas.1518891113.

He, Shaoda, and Sjors H. W. Scheres. 2017. 'Helical Reconstruction in RELION'. *Journal of Structural Biology* 198 (3): 163–76. https://doi.org/10.1016/j.jsb.2017.02.003.

Heissler, Sarah M., Amandeep S. Arora, Neil Billington, James R. Sellers, and Krishna Chinthalapudi. 2021. 'Cryo-EM Structure of the Autoinhibited State of Myosin-2'. *Science Advances* 7 (52): eabk3273. https://doi.org/10.1126/sciadv.abk3273.

Heissler, Sarah M., and James R. Sellers. 2016. 'Kinetic Adaptations of Myosins for Their Diverse Cellular Functions'. *Traffic (Copenhagen, Denmark)* 17 (8): 839–59. https://doi.org/10.1111/tra.12388.

Henderson, Christine A., Christopher G. Gomez, Stefanie M. Novak, Lei Mi-Mi, and Carol C. Gregorio. 2017. 'Overview of the Muscle Cytoskeleton'. In *Comprehensive Physiology*, 891–944. John Wiley & Sons, Ltd. https://doi.org/10.1002/cphy.c160033.

Henderson, Richard, Andrej Sali, Matthew L. Baker, Bridget Carragher, Batsal Devkota, Kenneth H. Downing, Edward H. Egelman, et al. 2012. 'Outcome of the First Electron Microscopy Validation Task Force Meeting'. *Structure* 20 (2): 205–14. https://doi.org/10.1016/j.str.2011.12.014.

Hooijman, Pleuni, Melanie A. Stewart, and Roger Cooke. 2011. 'A New State of Cardiac Myosin with Very Slow ATP Turnover: A Potential Cardioprotective Mechanism in the Heart'. *Biophysical Journal* 100 (8): 1969–76. https://doi.org/10.1016/j.bpj.2011.02.061.

Hornemann, Thorsten, Stefan Kempa, Mirko Himmel, Katrin Hayeß, Dieter O. Fürst, and Theo Wallimann. 2003. 'Muscle-Type Creatine Kinase Interacts with Central Domains of the M-Band Proteins Myomesin and M-Protein'. *Journal of Molecular Biology* 332 (4): 877–87. https://doi.org/10.1016/S0022-2836(03)00921-5.

Hu, Zhongjun, Dianne W. Taylor, Michael K. Reedy, Robert J. Edwards, and Kenneth A. Taylor. 2016. 'Structure of Myosin Filaments from Relaxed Lethocerus Flight Muscle by Cryo-EM

at 6 Å Resolution'. *Science Advances* 2 (9): e1600058. https://doi.org/10.1126/sciadv.1600058.
Huxley, A. F., and R. Niedergerke. 1954. 'Structural Changes in Muscle During Contraction: Interference Microscopy of Living Muscle Fibres'. *Nature* 173 (4412): 971–73. https://doi.org/10.1038/173971a0.
Huxley, H. E. 1957. 'THE DOUBLE ARRAY OF FILAMENTS IN CROSS-STRIATED MUSCLE'. *The Journal of Biophysical and Biochemical Cytology* 3 (5): 631–48. https://doi.org/10.1083/jcb.3.5.631.
Huxley, H. E., and W. Brown. 1967. 'The Low-Angle X-Ray Diagram of Vertebrate Striated Muscle and Its Behaviour during Contraction and Rigor'. *Journal of Molecular Biology* 30 (2): 383-IN16. https://doi.org/10.1016/S0022-2836(67)80046-9.
Huxley, Hugh, and Jean Hanson. 1954. 'Changes in the Cross-Striations of Muscle during Contraction and Stretch and Their Structural Interpretation'. *Nature* 173 (4412): 973–76. https://doi.org/10.1038/173973a0.
Irving, Malcolm. 2017. 'Regulation of Contraction by the Thick Filaments in Skeletal Muscle'. *Biophysical Journal* 113 (12): 2579–94. https://doi.org/10.1016/j.bpj.2017.09.037.
Jacob, R., B. Dierberger, and G. Kissling. 1992. 'Functional Significance of the Frank-Starling Mechanism under Physiological and Pathophysiological Conditions'. *European Heart Journal* 13 (suppl_E): 7–14. https://doi.org/10.1093/eurheartj/13.suppl_E.7.
Jeon, Young Keul, Jae Boum Youm, Kotdaji Ha, JooHan Woo, Hae Young Yoo, Chae Hun Leem, Seung Hee Lee, and Sung Joon Kim. 2020. 'Teaching Cardiac Excitation-Contraction Coupling Using a Mathematical Computer Simulation Model of Human Ventricular Myocytes'. *Advances in Physiology Education* 44 (3): 323–33. https://doi.org/10.1152/advan.00093.2019.
Jumper, John, Richard Evans, Alexander Pritzel, Tim Green, Michael Figurnov, Olaf Ronneberger, Kathryn Tunyasuvunakool, et al. 2021. 'Highly Accurate Protein Structure Prediction with AlphaFold'. *Nature* 596 (7873): 583–89. https://doi.org/10.1038/s41586-021-03819-2.
Kaech, Andres, and Urs Ziegler. 2014. 'High-Pressure Freezing: Current State and Future Prospects'. In *Electron Microscopy: Methods and Protocols*, edited by John Kuo, 151–71. Methods in Molecular Biology. Totowa, NJ: Humana Press. https://doi.org/10.1007/978-1-62703-776-1_8.
Kampourakis, Thomas, Ziqian Yan, Mathias Gautel, Yin-Biao Sun, and Malcolm Irving. 2014. 'Myosin Binding Protein-C Activates Thin Filaments and Inhibits Thick Filaments in Heart Muscle Cells'. *Proceedings of the National Academy of Sciences* 111 (52): 18763–68. https://doi.org/10.1073/pnas.1413922112.
Kaur, Satinder, Josue Gomez-Blanco, Ahmad A. Z. Khalifa, Swathi Adinarayanan, Ruben Sanchez-Garcia, Daniel Wrapp, Jason S. McLellan, Khanh Huy Bui, and Javier Vargas. 2021. 'Local Computational Methods to Improve the Interpretability and Analysis of Cryo-EM Maps'. *Nature Communications* 12 (1): 1240. https://doi.org/10.1038/s41467-021-21509-5.
Kidmose, R. T., J. Juhl, P. Nissen, T. Boesen, J. L. Karlsen, and B. P. Pedersen. 2019. 'Namdinator – Automatic Molecular Dynamics Flexible Fitting of Structural Models into Cryo-EM and Crystallography Experimental Maps'. *IUCrJ* 6 (4): 526–31. https://doi.org/10.1107/S2052252519007619.
Kiess, Tobias-Oliver, and Jens Kockskämper. 2019. 'SERCA Activity Controls the Systolic Calcium Increase in the Nucleus of Cardiac Myocytes'. *Frontiers in Physiology* 10. https://www.frontiersin.org/articles/10.3389/fphys.2019.00056.
Kominz, D. R., E. R. Mitchell, T. Nihei, and C. M. Kay. 1965. 'The Papain Digestion of Skeletal Myosin A*'. *Biochemistry* 4 (11): 2373–82. https://doi.org/10.1021/bi00887a017.
Kremer, James R., David N. Mastronarde, and J. Richard McIntosh. 1996. 'Computer Visualization of Three-Dimensional Image Data Using IMOD'. *Journal of Structural Biology* 116 (1): 71–76. https://doi.org/10.1006/jsbi.1996.0013.

Kremneva, Elena, Maarit H. Makkonen, Aneta Skwarek-Maruszewska, Gergana Gateva, Alphee Michelot, Roberto Dominguez, and Pekka Lappalainen. 2014. 'Cofilin-2 Controls Actin Filament Length in Muscle Sarcomeres'. *Developmental Cell* 31 (2): 215–26. https://doi.org/10.1016/j.devcel.2014.09.002.

Krishnan, Anita, Rajeev Samtani, Preeta Dhanantwari, Elaine Lee, Shigehito Yamada, Kohei Shiota, Mary T. Donofrio, Linda Leatherbury, and Cecilia W. Lo. 2014. 'A Detailed Comparison of Mouse and Human Cardiac Development'. *Pediatric Research* 76 (6): 500–507. https://doi.org/10.1038/pr.2014.128.

Kritikou, Ekat. 2010. 'To See Them Contract for the First Time'. *Nature Reviews Molecular Cell Biology* 9 (1): s5–s5. https://doi.org/10.1038/nrm2556.

Krivanek, Ondrej L., Alexander J. Gubbens, and Niklas Dellby. 1991. 'Developments in EELS Instrumentation for Spectroscopy and Imaging'. *Microscopy Microanalysis Microstructures* 2 (2–3): 315–32. https://doi.org/10.1051/mmm:0199100202-3031500.

Krüger, Martina, and Wolfgang A. Linke. 2011. 'The Giant Protein Titin: A Regulatory Node That Integrates Myocyte Signaling Pathways*'. *Journal of Biological Chemistry* 286 (12): 9905–12. https://doi.org/10.1074/jbc.R110.173260.

Kuba, Jakub, John Mitchels, Miloš Hovorka, Philipp Erdmann, Lukáš Berka, Robert Kirmse, Julia König, Jan De Bock, Bernhard Goetze, and Alexander Rigort. 2021. 'Advanced Cryo-Tomography Workflow Developments – Correlative Microscopy, Milling Automation and Cryo-Lift-Out'. *Journal of Microscopy* 281 (2): 112–24. https://doi.org/10.1111/jmi.12939.

Kühlbrandt, Werner. 2014. 'The Resolution Revolution'. *Science* 343 (6178): 1443–44. https://doi.org/10.1126/science.1251652.

Labeit, S., M. Gautel, A. Lakey, and J. Trinick. 1992. 'Towards a Molecular Understanding of Titin'. *The EMBO Journal* 11 (5): 1711–16. https://doi.org/10.1002/j.1460-2075.1992.tb05222.x.

Lange, Stephan, Mirko Himmel, Daniel Auerbach, Irina Agarkova, Katrin Hayess, Dieter O. Fürst, Jean-Claude Perriard, and Elisabeth Ehler. 2005. 'Dimerisation of Myomesin: Implications for the Structure of the Sarcomeric M-Band'. *Journal of Molecular Biology* 345 (2): 289–98. https://doi.org/10.1016/j.jmb.2004.10.040.

Lange, Stephan, Nikos Pinotsis, Irina Agarkova, and Elisabeth Ehler. 2020. 'The M-Band: The Underestimated Part of the Sarcomere'. *Biochimica et Biophysica Acta (BBA) - Molecular Cell Research*, Cardiomyocyte biology: new pathways of differentiation and regeneration, 1867 (3): 118440. https://doi.org/10.1016/j.bbamcr.2019.02.003.

Lappalainen, Pekka, Tommi Kotila, Antoine Jégou, and Guillaume Romet-Lemonne. 2022. 'Biochemical and Mechanical Regulation of Actin Dynamics'. *Nature Reviews Molecular Cell Biology* 23 (12): 836–52. https://doi.org/10.1038/s41580-022-00508-4.

Leapman, Richard D., and Songquan Sun. 1995. 'Cryo-Electron Energy Loss Spectroscopy: Observations on Vitrified Hydrated Specimens and Radiation Damage'. *Ultramicroscopy*, Proceedings of the 2nd international workshop on Electron Energy Loss Spectroscopy and Imaging, 59 (1): 71–79. https://doi.org/10.1016/0304-3991(95)00019-W.

Lemke, Sandra B., and Frank Schnorrer. 2017. 'Mechanical Forces during Muscle Development'. *Mechanisms of Development* 144 (Pt A): 92–101. https://doi.org/10.1016/j.mod.2016.11.003.

Li, Jiawei, Hamidreza Rahmani, Fatemeh Abbasi Yeganeh, Hosna Rastegarpouyani, Dianne W. Taylor, Neil B. Wood, Michael J. Previs, Hiroyuki Iwamoto, and Kenneth A. Taylor. 2022. 'Structure of the Flight Muscle Thick Filament from the Bumble Bee, Bombus Ignitus, at 6 Å Resolution'. *International Journal of Molecular Sciences* 24 (1): 377. https://doi.org/10.3390/ijms24010377.

Linari, Marco, Elisabetta Brunello, Massimo Reconditi, Luca Fusi, Marco Caremani, Theyencheri Narayanan, Gabriella Piazzesi, Vincenzo Lombardi, and Malcolm Irving. 2015. 'Force

Generation by Skeletal Muscle Is Controlled by Mechanosensing in Myosin Filaments'. *Nature* 528 (7581): 276–79. https://doi.org/10.1038/nature15727.
Linke, Wolfgang A., and Nazha Hamdani. 2014. 'Gigantic Business'. *Circulation Research* 114 (6): 1052–68. https://doi.org/10.1161/CIRCRESAHA.114.301286.
Littlefield, R., and V. M. Fowler. 1998. 'DEFINING ACTIN FILAMENT LENGTH IN STRIATED MUSCLE: Rulers and Caps or Dynamic Stability?' *Annual Review of Cell and Developmental Biology* 14 (1): 487–525. https://doi.org/10.1146/annurev.cellbio.14.1.487.
Littlefield, Ryan S., and Velia M. Fowler. 2008. 'Thin Filament Length Regulation in Striated Muscle Sarcomeres: Pointed-End Dynamics Go beyond a Nebulin Ruler'. *Seminars in Cell & Developmental Biology* 19 (6): 511–19. https://doi.org/10.1016/j.semcdb.2008.08.009.
Liu, Yingjuan, Sen Chen, Liesl Zühlke, Graeme C Black, Mun-kit Choy, Ningxiu Li, and Bernard D Keavney. 2019. 'Global Birth Prevalence of Congenital Heart Defects 1970–2017: Updated Systematic Review and Meta-Analysis of 260 Studies'. *International Journal of Epidemiology* 48 (2): 455–63. https://doi.org/10.1093/ije/dyz009.
Llinas, Paola, Tatiana Isabet, Lin Song, Virginie Ropars, Bin Zong, Hannah Benisty, Serena Sirigu, et al. 2015. 'How Actin Initiates the Motor Activity of Myosin'. *Developmental Cell* 33 (4): 401–12. https://doi.org/10.1016/j.devcel.2015.03.025.
Loescher, Christine M, Anastasia J Hobbach, and Wolfgang A Linke. 2022. 'Titin (TTN): From Molecule to Modifications, Mechanics, and Medical Significance'. *Cardiovascular Research* 118 (14): 2903–18. https://doi.org/10.1093/cvr/cvab328.
Luther, Pradeep K. 2009. 'The Vertebrate Muscle Z-Disc: Sarcomere Anchor for Structure and Signalling'. *Journal of Muscle Research and Cell Motility* 30 (5): 171–85. https://doi.org/10.1007/s10974-009-9189-6.
Luther, Pradeep K., Pauline M. Bennett, Carlo Knupp, Roger Craig, Raúl Padrón, Samantha P. Harris, Jitendrakumar Patel, and Richard L. Moss. 2008. 'Understanding the Organisation and Role of Myosin Binding Protein C in Normal Striated Muscle by Comparison with MyBP-C Knockout Cardiac Muscle'. *Journal of Molecular Biology* 384 (1): 60–72. https://doi.org/10.1016/j.jmb.2008.09.013.
Luther, Pradeep K., Peter M. G. Munro, and John M. Squire. 1981. 'Three-Dimensional Structure of the Vertebrate Muscle A-Band: III. M-Region Structure and Myosin Filament Symmetry'. *Journal of Molecular Biology* 151 (4): 703–30. https://doi.org/10.1016/0022-2836(81)90430-7.
Luther, Pradeep K., Hanspeter Winkler, Kenneth Taylor, Maria E. Zoghbi, Roger Craig, Raúl Padrón, John M. Squire, and Jun Liu. 2011. 'Direct Visualization of Myosin-Binding Protein C Bridging Myosin and Actin Filaments in Intact Muscle'. *Proceedings of the National Academy of Sciences* 108 (28): 11423–28. https://doi.org/10.1073/pnas.1103216108.
Ma, Weikang, Henry Gong, Lin Qi, Suman Nag, and Thomas C. Irving. 2022. 'Cardiac Myosin Filaments Are Directly Regulated by Calcium'. Preprint. Biophysics. https://doi.org/10.1101/2022.02.19.481172.
Mahamid, Julia, Stefan Pfeffer, Miroslava Schaffer, Elizabeth Villa, Radostin Danev, Luis Kuhn Cuellar, Friedrich Förster, Anthony A. Hyman, Jürgen M. Plitzko, and Wolfgang Baumeister. 2016. 'Visualizing the Molecular Sociology at the HeLa Cell Nuclear Periphery'. *Science* 351 (6276): 969–72. https://doi.org/10.1126/science.aad8857.
Main, Alice, William Fuller, and George S. Baillie. 2020. 'Post-Translational Regulation of Cardiac Myosin Binding Protein-C: A Graphical Review'. *Cellular Signalling* 76 (December): 109788. https://doi.org/10.1016/j.cellsig.2020.109788.
Makovetsky, Ruslana, Nicolas Piche, and Mike Marsh. 2018. 'Dragonfly as a Platform for Easy Image-Based Deep Learning Applications'. *Microscopy and Microanalysis* 24 (S1): 532–33. https://doi.org/10.1017/S143192761800315X.

Marcucci, Lorenzo. 2023. 'Muscle Mechanics and Thick Filament Activation: An Emerging Two-Way Interaction for the Vertebrate Striated Muscle Fine Regulation'. *International Journal of Molecular Sciences* 24 (7): 6265. https://doi.org/10.3390/ijms24076265.

Marko, M., C. Hsieh, W. Moberlychan, C. A. Mannella, and J. Frank. 2006. 'Focused Ion Beam Milling of Vitreous Water: Prospects for an Alternative to Cryo-Ultramicrotomy of Frozen-Hydrated Biological Samples'. *Journal of Microscopy* 222 (1): 42–47. https://doi.org/10.1111/j.1365-2818.2006.01567.x.

Marston, Steven, O'Neal Copeland, Adam Jacques, Karen Livesey, Victor Tsang, William J. McKenna, Shapour Jalilzadeh, Sebastian Carballo, Charles Redwood, and Hugh Watkins. 2009. 'Evidence From Human Myectomy Samples That MYBPC3 Mutations Cause Hypertrophic Cardiomyopathy Through Haploinsufficiency*'. *Circulation Research* 105 (3): 219–22. https://doi.org/10.1161/CIRCRESAHA.109.202440.

Martynowycz, Michael W., Max T. B. Clabbers, Johan Unge, Johan Hattne, and Tamir Gonen. 2021. 'Benchmarking the Ideal Sample Thickness in Cryo-EM'. *Proceedings of the National Academy of Sciences* 118 (49): e2108884118. https://doi.org/10.1073/pnas.2108884118.

Maruyama, K, T Yoshioka, H Higuchi, K Ohashi, S Kimura, and R Natori. 1985. 'Connectin Filaments Link Thick Filaments and Z Lines in Frog Skeletal Muscle as Revealed by Immunoelectron Microscopy.' *Journal of Cell Biology* 101 (6): 2167–72. https://doi.org/10.1083/jcb.101.6.2167.

Mastronarde, David N. 2003. 'SerialEM: A Program for Automated Tilt Series Acquisition on Tecnai Microscopes Using Prediction of Specimen Position'. *Microscopy and Microanalysis* 9 (S02): 1182–83. https://doi.org/10.1017/S1431927603445911.

Mayans, Olga, Peter F. M. van der Ven, Matthias Wilm, Alexander Mues, Paul Young, Dieter O. Fürst, Matthias Wilmanns, and Mathias Gautel. 1998. 'Structural Basis for Activation of the Titin Kinase Domain during Myofibrillogenesis'. *Nature* 395 (6705): 863–69. https://doi.org/10.1038/27603.

McLachlan, Andrew D., and Jonathan Karn. 1982. 'Periodic Charge Distributions in the Myosin Rod Amino Acid Sequence Match Cross-Bridge Spacings in Muscle'. *Nature* 299 (5880): 226–31. https://doi.org/10.1038/299226a0.

McNamara, James W., Amy Li, Nicola J. Smith, Sean Lal, Robert M. Graham, Kristina Bezold Kooiker, Sabine J. van Dijk, Cristobal G. dos Remedios, Samantha P. Harris, and Roger Cooke. 2016. 'Ablation of Cardiac Myosin Binding Protein-C Disrupts the Super-Relaxed State of Myosin in Murine Cardiomyocytes'. *Journal of Molecular and Cellular Cardiology* 94 (May): 65–71. https://doi.org/10.1016/j.yjmcc.2016.03.009.

Mehta, Amit D., Ronald S. Rock, Matthias Rief, James A. Spudich, Mark S. Mooseker, and Richard E. Cheney. 1999. 'Myosin-V Is a Processive Actin-Based Motor'. *Nature* 400 (6744): 590–93. https://doi.org/10.1038/23072.

Merino, Felipe, Sabrina Pospich, Johanna Funk, Thorsten Wagner, Florian Küllmer, Hans-Dieter Arndt, Peter Bieling, and Stefan Raunser. 2018. 'Structural Transitions of F-Actin upon ATP Hydrolysis at near-Atomic Resolution Revealed by Cryo-EM'. *Nature Structural & Molecular Biology* 25 (6): 528–37. https://doi.org/10.1038/s41594-018-0074-0.

Merino, Felipe, Sabrina Pospich, and Stefan Raunser. 2020. 'Towards a Structural Understanding of the Remodeling of the Actin Cytoskeleton'. *Seminars in Cell & Developmental Biology*, SI: Actin_15 June 2019, 102 (June): 51–64. https://doi.org/10.1016/j.semcdb.2019.11.018.

Moncman, Carole L., and Kuan Wang. 1995. 'Nebulette: A 107 kD Nebulin-like Protein in Cardiac Muscle'. *Cell Motility* 32 (3): 205–25. https://doi.org/10.1002/cm.970320305.

Moriya, Toshio, Michael Saur, Markus Stabrin, Felipe Merino, Horatiu Voicu, Zhong Huang, Pawel A. Penczek, Stefan Raunser, and Christos Gatsogiannis. 2017. 'High-resolution Single Particle Analysis from Electron Cryo-microscopy Images Using SPHIRE'. *JoVE (Journal of Visualized Experiments)*, no. 123 (May): e55448. https://doi.org/10.3791/55448.

Moss Richard L., Fitzsimons Daniel P., and Ralphe J. Carter. 2015. 'Cardiac MyBP-C Regulates the Rate and Force of Contraction in Mammalian Myocardium'. *Circulation Research* 116 (1): 183–92. https://doi.org/10.1161/CIRCRESAHA.116.300561.

Nag, Suman, and Darshan V Trivedi. 2021. 'To Lie or Not to Lie: Super-Relaxing with Myosins'. Edited by Suzanne R Pfeffer. *eLife* 10 (February): e63703. https://doi.org/10.7554/eLife.63703.

Nakao, K., W. Minobe, R. Roden, M. R. Bristow, and L. A. Leinwand. 1997. 'Myosin Heavy Chain Gene Expression in Human Heart Failure.' *The Journal of Clinical Investigation* 100 (9): 2362–70. https://doi.org/10.1172/JCI119776.

Obermann, W M, M Gautel, F Steiner, P F van der Ven, K Weber, and D O Fürst. 1996. 'The Structure of the Sarcomeric M Band: Localization of Defined Domains of Myomesin, M-Protein, and the 250-kD Carboxy-Terminal Region of Titin by Immunoelectron Microscopy.' *Journal of Cell Biology* 134 (6): 1441–53. https://doi.org/10.1083/jcb.134.6.1441.

Obermann, Wolfgang M.J., Mathias Gautel, Klaus Weber, and Dieter O. Fürst. 1997. 'Molecular Structure of the Sarcomeric M Band: Mapping of Titin and Myosin Binding Domains in Myomesin and the Identification of a Potential Regulatory Phosphorylation Site in Myomesin'. *The EMBO Journal* 16 (2): 211–20. https://doi.org/10.1093/emboj/16.2.211.

Offer, Gebald, Cabl Moos, and Roger Starr. 1973. 'A New Protein of the Thick Filaments of Vertebrate Skeletal Myofibrils: Extraction, Purification and Characterization'. *Journal of Molecular Biology* 74 (4): 653–76. https://doi.org/10.1016/0022-2836(73)90055-7.

Ohtsuki, Iwao. 1974. 'Localization of Troponin in Thin Filament and Tropomyosin Paracrystal*'. *The Journal of Biochemistry* 75 (4): 753–65. https://doi.org/10.1093/oxfordjournals.jbchem.a130448.

Oosterheert, Wout, Florian E. C. Blanc, Ankit Roy, Alexander Belyy, Micaela Boiero Sanders, Oliver Hofnagel, Gerhard Hummer, Peter Bieling, and Stefan Raunser. 2023. 'Molecular Mechanisms of Inorganic-Phosphate Release from the Core and Barbed End of Actin Filaments'. *Nature Structural & Molecular Biology* 30 (11): 1774–85. https://doi.org/10.1038/s41594-023-01101-9.

Oosterheert, Wout, Björn U. Klink, Alexander Belyy, Sabrina Pospich, and Stefan Raunser. 2022. 'Structural Basis of Actin Filament Assembly and Aging'. *Nature* 611 (7935): 374–79. https://doi.org/10.1038/s41586-022-05241-8.

Padrón, Raúl, Weikang Ma, Sebastian Duno-Miranda, Natalia Koubassova, Kyoung Hwan Lee, Antonio Pinto, Lorenzo Alamo, et al. 2020. 'The Myosin Interacting-Heads Motif Present in Live Tarantula Muscle Explains Tetanic and Posttetanic Phosphorylation Mechanisms'. *Proceedings of the National Academy of Sciences* 117 (22): 11865–74. https://doi.org/10.1073/pnas.1921312117.

Page, Sally G. 1974. 'Measurements of Structural Parameters in Cardiac Muscle'. In *Ciba Foundation Symposium 24 - Physiological Basis of Starling's Law of the Heart*, 13–30. John Wiley & Sons, Ltd. https://doi.org/10.1002/9780470720066.ch3.

Palmio, Johanna, Sarah Leonard-Louis, Sabrina Sacconi, Marco Savarese, Sini Penttilä, Anna-Lena Semmler, Wolfram Kress, et al. 2019. 'Expanding the Importance of HMERF Titinopathy: New Mutations and Clinical Aspects'. *Journal of Neurology* 266 (3): 680–90. https://doi.org/10.1007/s00415-019-09187-2.

Penczek, Pawel A. 2010. 'Resolution Measures in Molecular Electron Microscopy'. *Methods in Enzymology* 482: 73–100. https://doi.org/10.1016/S0076-6879(10)82003-8.

Pernigo, Stefano, Atsushi Fukuzawa, Amy E. M. Beedle, Mark Holt, Adam Round, Alessandro Pandini, Sergi Garcia-Manyes, Mathias Gautel, and Roberto A. Steiner. 2017. 'Binding of Myomesin to Obscurin-Like-1 at the Muscle M-Band Provides a Strategy for Isoform-Specific Mechanical Protection'. *Structure (London, England: 1993)* 25 (1): 107–20. https://doi.org/10.1016/j.str.2016.11.015.

Pernigo, Stefano, Atsushi Fukuzawa, Morten Bertz, Mark Holt, Matthias Rief, Roberto A. Steiner, and Mathias Gautel. 2010. 'Structural Insight into M-Band Assembly and Mechanics from the Titin-Obscurin-like-1 Complex'. *Proceedings of the National Academy of Sciences of the United States of America* 107 (7): 2908–13. https://doi.org/10.1073/pnas.0913736107.

Perrin, Benjamin J., and James M. Ervasti. 2010. 'The Actin Gene Family: Function Follows Isoform'. *Cytoskeleton* 67 (10): 630–34. https://doi.org/10.1002/cm.20475.

Pettersen, Eric F., Thomas D. Goddard, Conrad C. Huang, Elaine C. Meng, Gregory S. Couch, Tristan I. Croll, John H. Morris, and Thomas E. Ferrin. 2021. 'UCSF ChimeraX: Structure Visualization for Researchers, Educators, and Developers'. *Protein Science* 30 (1): 70–82. https://doi.org/10.1002/pro.3943.

Pilagov, Matvey, Laurens W.H.J. Heling, Jonathan Walklate, Michael A. Geeves, and Neil M. Kad. 2022. 'Single-Molecule Imaging Reveals How Mavacamten and PKA Modulate ATP Turnover in Skeletal Muscle Myofibrils'. *Journal of General Physiology* 155 (1): e202213087. https://doi.org/10.1085/jgp.202213087.

Pollard, Thomas D., and John A. Cooper. 2009. 'Actin, a Central Player in Cell Shape and Movement'. *Science* 326 (5957): 1208–12. https://doi.org/10.1126/science.1175862.

Ponnam, Saraswathi, and Thomas Kampourakis. 2021. 'Microscale Thermophoresis Suggests a New Model of Regulation of Cardiac Myosin Function via Interaction with Cardiac Myosin Binding Protein-C'. *Journal of Biological Chemistry*, December, 101485. https://doi.org/10.1016/j.jbc.2021.101485.

Ponnam, Saraswathi, Ivanka Sevrieva, Yin-Biao Sun, Malcolm Irving, and Thomas Kampourakis. 2019. 'Site-Specific Phosphorylation of Myosin Binding Protein-C Coordinates Thin and Thick Filament Activation in Cardiac Muscle'. *Proceedings of the National Academy of Sciences* 116 (31): 15485–94. https://doi.org/10.1073/pnas.1903033116.

Powell, Cameron J., Raghavendran Ramaswamy, Anne Kelsen, David J. Hamelin, David M. Warshaw, Jürgen Bosch, John E. Burke, Gary E. Ward, and Martin J. Boulanger. 2018. 'Structural and Mechanistic Insights into the Function of the Unconventional Class XIV Myosin MyoA from Toxoplasma Gondii'. *Proceedings of the National Academy of Sciences* 115 (45): E10548–55. https://doi.org/10.1073/pnas.1811167115.

Previs, M. J., S. Beck Previs, J. Gulick, J. Robbins, and D. M. Warshaw. 2012. 'Molecular Mechanics of Cardiac Myosin-Binding Protein C in Native Thick Filaments'. *Science* 337 (6099): 1215–18. https://doi.org/10.1126/science.1223602.

Previs, Michael J., Ji Young Mun, Arthur J. Michalek, Samantha Beck Previs, James Gulick, Jeffrey Robbins, David M. Warshaw, and Roger Craig. 2016. 'Phosphorylation and Calcium Antagonistically Tune Myosin-Binding Protein C's Structure and Function'. *Proceedings of the National Academy of Sciences* 113 (12): 3239–44. https://doi.org/10.1073/pnas.1522236113.

Puchner, Elias M., Alexander Alexandrovich, Ay Lin Kho, Ulf Hensen, Lars V. Schäfer, Birgit Brandmeier, Frauke Gräter, Helmut Grubmüller, Hermann E. Gaub, and Mathias Gautel. 2008. 'Mechanoenzymatics of Titin Kinase'. *Proceedings of the National Academy of Sciences of the United States of America* 105 (36): 13385–90. https://doi.org/10.1073/pnas.0805034105.

Pyle, Euan, and Giulia Zanetti. 2021. 'Current Data Processing Strategies for Cryo-Electron Tomography and Subtomogram Averaging'. *Biochemical Journal* 478 (10): 1827–45. https://doi.org/10.1042/BCJ20200715.

Rahmani, Hamidreza, Wen Ma, Zhongjun Hu, Nadia Daneshparvar, Dianne W. Taylor, J. Andrew McCammon, Thomas C. Irving, Robert J. Edwards, and Kenneth A. Taylor. 2021. 'The Myosin II Coiled-Coil Domain Atomic Structure in Its Native Environment'. *Proceedings of the National Academy of Sciences* 118 (14). https://doi.org/10.1073/pnas.2024151118.

Rahmanseresht, Sheema, Kyoung H. Lee, Thomas S. O'Leary, James W. McNamara, Sakthivel Sadayappan, Jeffrey Robbins, David M. Warshaw, Roger Craig, and Michael J. Previs.

2021. ‘The N Terminus of Myosin-Binding Protein C Extends toward Actin Filaments in Intact Cardiac Muscle’. *Journal of General Physiology* 153 (3): e202012726. https://doi.org/10.1085/jgp.202012726.

Ramaraj, Radhakrishnan. 2008. ‘Hypertrophic Cardiomyopathy: Etiology, Diagnosis, and Treatment’. *Cardiology in Review* 16 (4): 172–80. https://doi.org/10.1097/CRD.0b013e318178e525.

Ratti, Joyce, Elena Rostkova, Mathias Gautel, and Mark Pfuhl. 2011. ‘Structure and Interactions of Myosin-Binding Protein C Domain C0 CARDIAC-SPECIFIC REGULATION OF MYOSIN AT ITS NECK?’ *Journal of Biological Chemistry* 286 (14): 12650–58. https://doi.org/10.1074/jbc.M110.156646.

Reedy, M. C., and C. Beall. 1993. ‘Ultrastructure of Developing Flight Muscle in Drosophila. I. Assembly of Myofibrils’. *Developmental Biology* 160 (2): 443–65. https://doi.org/10.1006/dbio.1993.1320.

Rees, Martin, Roksana Nikoopour, Atsushi Fukuzawa, Ay Lin Kho, Miguel A. Fernandez-Garcia, Elizabeth Wraige, Istvan Bodi, et al. 2021. ‘Making Sense of Missense Variants in TTN-Related Congenital Myopathies’. *Acta Neuropathologica* 141 (3): 431–53. https://doi.org/10.1007/s00401-020-02257-0.

Risi, Cristina M., Edwin Villanueva, Betty Belknap, Rachel L. Sadler, Samantha P. Harris, Howard D. White, and Vitold E. Galkin. 2022. ‘Cryo-Electron Microscopy Reveals Cardiac Myosin Binding Protein-C M-Domain Interactions with the Thin Filament’. *Journal of Molecular Biology* 434 (24): 167879. https://doi.org/10.1016/j.jmb.2022.167879.

Robinson, T F, and S Winegrad. 1979. ‘The Measurement and Dynamic Implications of Thin Filament Lengths in Heart Muscle.’ *The Journal of Physiology* 286 (January): 607–19.

Robinson, Thomas F., and Saul Winegrad. 1977. ‘Variation of Thin Filament Length in Heart Muscle’. *Nature* 267 (5606): 74–75. https://doi.org/10.1038/267074a0.

Ruppel, Kathleen M., and James A. Spudich. 1996. ‘Structure-Function Analysis of the Motor Domain of Myosin’. *Annual Review of Cell and Developmental Biology* 12 (1): 543–73. https://doi.org/10.1146/annurev.cellbio.12.1.543.

Santini, Lorenzo, Chiara Palandri, Chiara Nediani, Elisabetta Cerbai, and Raffaele Coppini. 2020. ‘Modelling Genetic Diseases for Drug Development: Hypertrophic Cardiomyopathy’. *Pharmacological Research*, August, 105176. https://doi.org/10.1016/j.phrs.2020.105176.

Schaffer, Miroslava, Julia Mahamid, Benjamin D. Engel, Tim Laugks, Wolfgang Baumeister, and Jürgen M. Plitzko. 2017. ‘Optimized Cryo-Focused Ion Beam Sample Preparation Aimed at in Situ Structural Studies of Membrane Proteins’. *Journal of Structural Biology*, Electron Tomography, 197 (2): 73–82. https://doi.org/10.1016/j.jsb.2016.07.010.

Scheres, Sjors H. W. 2012a. ‘A Bayesian View on Cryo-EM Structure Determination’. *Journal of Molecular Biology* 415 (2): 406–18. https://doi.org/10.1016/j.jmb.2011.11.010.

———. 2012b. ‘RELION: Implementation of a Bayesian Approach to Cryo-EM Structure Determination’. *Journal of Structural Biology* 180 (3): 519–30. https://doi.org/10.1016/j.jsb.2012.09.006.

Schiaffino, Stefano, Alberto C. Rossi, Vika Smerdu, Leslie A. Leinwand, and Carlo Reggiani. 2015. ‘Developmental Myosins: Expression Patterns and Functional Significance’. *Skeletal Muscle* 5 (1): 22. https://doi.org/10.1186/s13395-015-0046-6.

Schöenfeld, Fabian, Markus Stabrin, Tanvir R. Shaikh, Thorsten Wagner, and Stefan Raunser. 2022. ‘Accelerated 2D Classification With ISAC Using GPUs’. *Frontiers in Molecular Biosciences* 9. https://www.frontiersin.org/articles/10.3389/fmolb.2022.919994.

Sjöström, Michael, and John M. Squire. 1977. ‘Cryo-Ultramicrotomy and Myofibrillar Fine Structure: A Review’. *Journal of Microscopy* 111 (2): 239–78. https://doi.org/10.1111/j.1365-2818.1977.tb00067.x.

Sohn, Regina L, Karen L Vikstrom, Michael Strauss, Carolyn Cohen, Andrew G Szent-Gyorgyi, and Leslie A Leinwand. 1997. ‘A 29 Residue Region of the Sarcomeric Myosin Rod Is

Necessary for Filament formation11Edited by J. Karn'. *Journal of Molecular Biology* 266 (2): 317–30. https://doi.org/10.1006/jmbi.1996.0790.
Squire, J. M. 1973. 'General Model of Myosin Filament Structure: III. Molecular Packing Arrangements in Myosin Filaments'. *Journal of Molecular Biology* 77 (2): 291–323. https://doi.org/10.1016/0022-2836(73)90337-9.
Squire, John M., Hind A. Al-khayat, Carlo Knupp, and Pradeep K. Luther. 2005. 'Molecular Architecture in Muscle Contractile Assemblies'. In *Advances in Protein Chemistry*, 71:17–87. Fibrous Proteins: Muscle and Molecular Motors. Academic Press. https://doi.org/10.1016/S0065-3233(04)71002-5.
Starr, R, and G Offer. 1978. 'The Interaction of C-Protein with Heavy Meromyosin and Subfragment-2'. *Biochemical Journal* 171 (3): 813–16. https://doi.org/10.1042/bj1710813.
Stewart, Melanie A., Kathleen Franks-Skiba, Susan Chen, and Roger Cooke. 2010. 'Myosin ATP Turnover Rate Is a Mechanism Involved in Thermogenesis in Resting Skeletal Muscle Fibers'. *Proceedings of the National Academy of Sciences* 107 (1): 430–35. https://doi.org/10.1073/pnas.0909468107.
Straight, Aaron F., Amy Cheung, John Limouze, Irene Chen, Nick J. Westwood, James R. Sellers, and Timothy J. Mitchison. 2003. 'Dissecting Temporal and Spatial Control of Cytokinesis with a Myosin II Inhibitor'. *Science* 299 (5613): 1743–47. https://doi.org/10.1126/science.1081412.
Sweeney, H. Lee, Anne Houdusse, and Julien Robert-Paganin. 2020. 'Myosin Structures'. In *Myosins: A Superfamily of Molecular Motors*, edited by Lynne M. Coluccio, 7–19. Advances in Experimental Medicine and Biology. Cham: Springer International Publishing. https://doi.org/10.1007/978-3-030-38062-5_2.
Szent-Györgyi, Andrew G. 2007. 'Regulation by Myosin: How Calcium Regulates Some Myosins, Past and Present'. In *Regulatory Mechanisms of Striated Muscle Contraction*, edited by Setsuro Ebashi and Iwao Ohtsuki, 253–64. Advances in Experimental Medicine and Biology. Tokyo: Springer Japan. https://doi.org/10.1007/978-4-431-38453-3_21.
Tacke, Sebastian, Philipp Erdmann, Zhexin Wang, Sven Klumpe, Michael Grange, Jürgen Plitzko, and Stefan Raunser. 2021. 'A Streamlined Workflow for Automated Cryo Focused Ion Beam Milling'. *Journal of Structural Biology* 213 (3): 107743. https://doi.org/10.1016/j.jsb.2021.107743.
Tamborrini, Davide, Zhexin Wang, Thorsten Wagner, Sebastian Tacke, Markus Stabrin, Michael Grange, Ay Lin Kho, et al. 2023. 'Structure of the Native Myosin Filament in the Relaxed Cardiac Sarcomere'. *Nature* 623 (7988): 863–71. https://doi.org/10.1038/s41586-023-06690-5.
Taylor, Keenan C., Massimo Buvoli, Elif Nihal Korkmaz, Ada Buvoli, Yuqing Zheng, Nathan T. Heinze, Qiang Cui, Leslie A. Leinwand, and Ivan Rayment. 2015. 'Skip Residues Modulate the Structural Properties of the Myosin Rod and Guide Thick Filament Assembly'. *Proceedings of the National Academy of Sciences* 112 (29): E3806–15. https://doi.org/10.1073/pnas.1505813112.
Tegunov, Dimitry, and Patrick Cramer. 2019. 'Real-Time Cryo-Electron Microscopy Data Preprocessing with Warp'. *Nature Methods* 16 (11): 1146–52. https://doi.org/10.1038/s41592-019-0580-y.
Tegunov, Dimitry, Liang Xue, Christian Dienemann, Patrick Cramer, and Julia Mahamid. 2021. 'Multi-Particle Cryo-EM Refinement with M Visualizes Ribosome-Antibiotic Complex at 3.5 Å in Cells'. *Nature Methods* 18 (2): 186–93. https://doi.org/10.1038/s41592-020-01054-7.
Thompson, Robert C., Massimo Buvoli, Ada Buvoli, and Leslie A. Leinwand. 2012. 'Myosin Filament Assembly Requires a Cluster of Four Positive Residues Located in the Rod Domain'. *FEBS Letters* 586 (19): 3008–12. https://doi.org/10.1016/j.febslet.2012.06.019.

Toepfer, Christopher N., Hiroko Wakimoto, Amanda C. Garfinkel, Barbara McDonough, Dan Liao, Jianming Jiang, Angela C. Tai, et al. 2019. 'Hypertrophic Cardiomyopathy Mutations in MYBPC3 Dysregulate Myosin'. *Science Translational Medicine* 11 (476). https://doi.org/10.1126/scitranslmed.aat1199.

Tonino, Paola, Balazs Kiss, Jochen Gohlke, John E. Smith, and Henk Granzier. 2019. 'Fine Mapping Titin's C-Zone: Matching Cardiac Myosin-Binding Protein C Stripes with Titin's Super-Repeats'. *Journal of Molecular and Cellular Cardiology* 133: 47–56. https://doi.org/10.1016/j.yjmcc.2019.05.026.

Trybus, Kathleen M. 1994. 'Role of Myosin Light Chains'. *Journal of Muscle Research & Cell Motility* 15 (6): 587–94. https://doi.org/10.1007/BF00121066.

Tskhovrebova, Larissa, and John Trinick. 2003. 'Titin: Properties and Family Relationships'. *Nature Reviews. Molecular Cell Biology* 4 (9): 679–89. https://doi.org/10.1038/nrm1198.

———. 2012. 'Molecular Rulers?' *Current Biology* 22 (9): R317–18. https://doi.org/10.1016/j.cub.2012.02.049.

Venturi, Federico. 2018. 'New Approaches for Phase Manipulation and Characterisation in the Transmission Electron Microscope'. https://doi.org/10.13140/RG.2.2.24104.32000.

Vibert, Peter, and Roger Craig. 1983. 'Electron Microscopy and Image Analysis of Myosin Filaments from Scallop Striated Muscle'. *Journal of Molecular Biology* 165 (2): 303–20. https://doi.org/10.1016/S0022-2836(83)80259-9.

Vibert, Peter, Roger Craig, and William Lehman. 1997. 'Steric-Model for Activation of Muscle Thin Filaments 1 1 Edited by P.E. Wright'. *Journal of Molecular Biology* 266 (1): 8–14. https://doi.org/10.1006/jmbi.1996.0800.

Wagner, Thorsten, Felipe Merino, Markus Stabrin, Toshio Moriya, Claudia Antoni, Amir Apelbaum, Philine Hagel, et al. 2019. 'SPHIRE-crYOLO Is a Fast and Accurate Fully Automated Particle Picker for Cryo-EM'. *Communications Biology* 2 (1): 1–13. https://doi.org/10.1038/s42003-019-0437-z.

Wan, W., and J. A. G. Briggs. 2016. 'Chapter Thirteen - Cryo-Electron Tomography and Subtomogram Averaging'. In *Methods in Enzymology*, edited by R. A. Crowther, 579:329–67. The Resolution Revolution: Recent Advances In cryoEM. Academic Press. https://doi.org/10.1016/bs.mie.2016.04.014.

Wang, Zhexin, Michael Grange, Sabrina Pospich, Thorsten Wagner, Ay Lin Kho, Mathias Gautel, and Stefan Raunser. 2022. 'Structures from Intact Myofibrils Reveal Mechanism of Thin Filament Regulation through Nebulin'. *Science* 375 (6582): eabn1934. https://doi.org/10.1126/science.abn1934.

Wang, Zhexin, Michael Grange, Thorsten Wagner, Ay Lin Kho, Mathias Gautel, and Stefan Raunser. 2021. 'The Molecular Basis for Sarcomere Organization in Vertebrate Skeletal Muscle'. *Cell* 184 (8): 2135-2150.e13. https://doi.org/10.1016/j.cell.2021.02.047.

Wang, Zhexin, and Stefan Raunser. 2023. 'Structural Biochemistry of Muscle Contraction'. *Annual Review of Biochemistry* 92 (1): 411–33. https://doi.org/10.1146/annurev-biochem-052521-042909.

Wells, Amber L., Abel W. Lin, Li-Qiong Chen, Daniel Safer, Shane M. Cain, Tama Hasson, Bridget O. Carragher, Ronald A. Milligan, and H. Lee Sweeney. 1999. 'Myosin VI Is an Actin-Based Motor That Moves Backwards'. *Nature* 401 (6752): 505–8. https://doi.org/10.1038/46835.

Wendt, Thomas, Dianne Taylor, Kathleen M. Trybus, and Kenneth Taylor. 2001. 'Three-Dimensional Image Reconstruction of Dephosphorylated Smooth Muscle Heavy Meromyosin Reveals Asymmetry in the Interaction between Myosin Heads and Placement of Subfragment 2'. *Proceedings of the National Academy of Sciences* 98 (8): 4361–66. https://doi.org/10.1073/pnas.071051098.

Williams, David B., and C. Barry Carter. 2009. 'The Transmission Electron Microscope'. In *Transmission Electron Microscopy: A Textbook for Materials Science*, edited by David B.

Williams and C. Barry Carter, 3–22. Boston, MA: Springer US. https://doi.org/10.1007/978-0-387-76501-3_1.

Woodhead, John L., Fa-Qing Zhao, Roger Craig, Edward H. Egelman, Lorenzo Alamo, and Raúl Padrón. 2005. 'Atomic Model of a Myosin Filament in the Relaxed State'. *Nature* 436 (7054): 1195–99. https://doi.org/10.1038/nature03920.

Xu, S., G. Offer, J. Gu, H. D. White, and L. C. Yu. 2003. 'Temperature and Ligand Dependence of Conformation and Helical Order in Myosin Filaments'. *Biochemistry* 42 (2): 390–401. https://doi.org/10.1021/bi026085t.

Xue, Han, Meng Zhang, Jianfang Liu, Jianjun Wang, and Gang Ren. 2022. 'Cryo-Electron Tomography Related Radiation-Damage Parameters for Individual-Molecule 3D Structure Determination'. *Frontiers in Chemistry* 10. https://www.frontiersin.org/articles/10.3389/fchem.2022.889203.

Yamada, Yurika, Keiichi Namba, and Takashi Fujii. 2020. 'Cardiac Muscle Thin Filament Structures Reveal Calcium Regulatory Mechanism'. *Nature Communications* 11 (1): 153. https://doi.org/10.1038/s41467-019-14008-1.

Yang, Shixin, Prince Tiwari, Kyoung Hwan Lee, Osamu Sato, Mitsuo Ikebe, Raúl Padrón, and Roger Craig. 2020. 'Cryo-EM Structure of the Inhibited (10S) Form of Myosin II'. *Nature* 588 (7838): 521–25. https://doi.org/10.1038/s41586-020-3007-0.

Yang, Zhengfan, Jia Fang, Johnathan Chittuluru, Francisco J. Asturias, and Pawel A. Penczek. 2012. 'Iterative Stable Alignment and Clustering of 2D Transmission Electron Microscope Images'. *Structure* 20 (2): 237–47. https://doi.org/10.1016/j.str.2011.12.007.

Yuen, Michaela, and Coen A. C. Ottenheijm. 2020. 'Nebulin: Big Protein with Big Responsibilities'. *Journal of Muscle Research and Cell Motility* 41 (1): 103–24. https://doi.org/10.1007/s10974-019-09565-3.

Zoghbi, Maria E., John L. Woodhead, Richard L. Moss, and Roger Craig. 2008. 'Three-Dimensional Structure of Vertebrate Cardiac Muscle Myosin Filaments'. *Proceedings of the National Academy of Sciences* 105 (7): 2386–90. https://doi.org/10.1073/pnas.0708912105.

CHAPTER 5 Publications and conference contributions

Publication

Tamborrini, Davide, Zhexin Wang, Thorsten Wagner, Sebastian Tacke, Markus Stabrin, Michael Grange, Ay Lin Kho, et al. **2023**. 'Structure of the Native Myosin Filament in the Relaxed Cardiac Sarcomere'. **Nature** 623 (7988): 863–71. https://doi.org/10.1038/s41586-023-06690-5.

Conference Contributions

Alpbach Molecular Motors: 25th - 31st of March 2023; Alpbach, Tirol - Austria.
Poster presentation, speaker in the general meeting, speaker in the focus session.

3rd MuscleX Workshop: 18th – 19th of May 2023; organized by bioCAT - Chicago, IL, United States.
Invited speaker.

Gordon Research Seminar - 3DEM: June 10th – 11th of June 2023; Newry, ME, United States.
Poster presentation and poster prize winner.

Gordon Research Conference - 3DEM: June 11th – 16th of June 2023; Newry, ME, United States.
Poster presentation and poster prize winner, selected speaker.

50th European Muscle Conference: 2nd – 6th September 2023; University of Florence, Italy.
Selected Speaker.

European Muscle Seminar: 6th September 2023; University of Florence, Italy.
Invited Speaker.

Human Technopole Colloquia Series: 15th September 2023; Human Technopole – Milan, Italy.
Invited Speaker.

Acknowledgements

"A smooth sea never made a skilled sailor." - Franklin D. Roosevelt

I am deeply indebted to Prof. Dr. Stefan Raunser, for giving me the chance to work on a Ph.D. project with high potential. For shaping me in a structural biochemist, for being a very supportive mentor and for teaching me a great deal about self-confidence.

I want to thank Prof. Dr. Heinz Neumann for giving me the chance to start my Ph.D. at the MPI and for his kind and patient guidance in the first two years, without him I could not have undertaken this journey. I am grateful to Petra, Martin, Neha, Damian, Anto, Sheila and Anson for the good time spent together in and out of the lab, and for providing me with great support at the very beginning of my time at the MPI.

I am thankful to Prof. Dr. Andrea Musacchio for his support and critical input along my entire journey and for offering shelter when I needed it the most, right after my first project fell apart. I am also thankful to Prof. Dr. Leif Dehlmet for accepting to be an examiner for my Ph.D. defense.

My sincere thanks also go to Zhexin (Eric) Wang, Thosten Wagner, Markus Stabrin, Astrid Sander, Sabrina Pospich and Asena Oelschläger, for teaching and/or supporting me so much and always being so cool about it. To Tobias Raich and Sebastian Tackle for listening and brainstorming with me all the times I was facing scientific, personal, or interpersonal challenges. To Christa and Lucia for their dedication and commitment to the IMPRS and for always providing help and support when needed. To my official and un-official office mates, for decorating the final part of my Ph.D. with funny and delightful memories: Oleg, Nina, Diana, Sree, Alicia, Elisa, Victoria, and Baptiste.

I am tremendously grateful to Martin Spinck and Peter Beiling for showing me how high the bar can be raised. For humbling me and fostering a stronger stoic attitude within me.

I want to thank Angela Hagemeier and Alex (Minghui) Xiu for being careful keepers of parts of me that exist only in their hands.

I thank my family for believing in me and always being the safe harbor I need during rough seas.

Finally, I would like to express my deepest gratitude to Chiara for her patience and for inspiring me to become the best version of myself. You have been my unwavering lighthouse, guiding me through the strongest winds when no other lights illuminated the sky. I love you.

"Two tasks to start life: narrow down your circle more and more and check over and over whether you are not hiding somewhere outside your circle." - Franz Kafka

I am grateful for the most challenging moments, both scientifically and personally. They washed away all the futile and inconsequential details that had been clouding my judgment and drive. These experiences refined the circle and enhanced my focus and my ability to handle scientific and personal questions, making me more effective. While the search for answers might never become easy, it is significantly simpler now.

I embarked on this journey with a resolute spirit, strong eagerness, and naïve optimism. Over the years, I have retained and strengthened all three of them. For this, I am extremely grateful.